

UNIVERSITÀ DEGLI STUDI DI MODENA E REGGIO EMILIA

Corso di dottorato di ricerca in
“Physics and Nanosciences”

**Investigation of charge transport in
graphene-related materials (GRMs)
thin films**

Candidato : ALEX BOSCHI

Relatore : Prof. VINCENZO PALERMO
(CNR-ISOF)

Coordinatore del
corso di dottorato :

Prof. STEFANO FRABBONI

Ciclo XXXIII
Marzo 2021

[...]

*Morre lentamente quem não vira a mesa
quando está infeliz no trabalho,
quem não arrisca o certo pelo incerto
atrás de um sonho,
quem não se permite, uma vez na vida,
fugir dos conselhos sensatos.*

[...]

Marta Medeiros, *A Morte Devagar* (2000)

[...] *Occorre una grande fantasia, una forte immaginazione, per essere un vero scienziato, per immaginare cose che non esistono ancora e scoprirle, per immaginare un mondo migliore di quello in cui viviamo e mettersi a lavorare per costruirlo.*

Gianni Rodari, H. C. *Andersen Award* acceptance speech,
XII IBBY Congress, Bologna (1970)

Abstract

The development of more economic techniques to produce large sheets of monoatomic layered materials, such as graphene, has opened new avenues to design nanostructured materials with pre-programmed chemical and physical properties. Most of the technologically relevant graphene-related material (GRM) systems are networks composed of randomly distributed and highly defective 2D nanosheets. While charge transport (CT) in single nanosheets has been extensively studied, its behaviour in well-stacked, reduced graphene oxide (RGO) thin films are being clarified only more recently. A multiscale geometrical model proposed to describe charge transport in these films is similar to that used for composite materials where quasi-1D building blocks behave as conductive fillers in an insulating matrix ("*spaghetti-like*" structures). The length of the quasi-1D wires is defined by the localization length ξ of the charge carriers. Despite this, a comprehensive study correlating the electrical properties of networks composed of purely 2D graphene-based materials with their structural complexity and morphology is still lacking.

This thesis aims to generalize this approach in order to describe charge transport in the various classes of GRM thin films, studying the role of building blocks and their arrangement when forming the thin film.

We compared two different GRMs produced at CNR-ISOF: reduced graphene oxide (RGO) and electrochemically exfoliated graphene oxide (EGO) and fabricated thin films with different arrangements using different deposition techniques, including i) spin-coating, ii) spray-coating and iii) vacuum assisted filtration. Multiscale structural analysis of the films was performed combining various experimental techniques: X-Ray Diffraction (XRD), optical (OM), Scanning Electron (SEM) and Atomic Force (AFM) microscopies; X-ray Photoelectron Spectroscopy (XPS) used for chemical analysis.

Described in terms of a polycrystalline system, we investigated the CT of the fabricated GRM thin films by measuring the temperature-dependence of the electrical resistivity (ρ) from room temperature down to only a few kelvin. Data analyses were performed using the reduced activation energy method: $W(T)$, allowing assignment of the various transport regimes in a self-consistent way. In the case of disordered RGO films we obtained excellent agreement with results reported in the literature. In particular, due to the low signal-to-noise ratio of the acquired data, we developed a generalization of the $W(T)$ approach. In this way, we showed that a correct analysis of ES-VRH

allows one to describe the resistance trend at low temperature, without invoking transitions between different VRH regimes, as is usually reported in the literature.

We found that the *spaghetti-like* structural model can be fruitfully used to describe CT in all the fabricated GRM thin films, both for RGO and EGO. We observed that the localization length ξ increases with the disordered stacking of the building blocks (i.e. the polycrystallinity) pointing out the effects of the multiscale mechanisms. The increase in disorder relates to an increase in the possible orientations of the building blocks and therefore to a greater number of structural configurations. This condition corresponds to the optimization of the interfaces on the nanometre scale and then, to a better chance that charges will jump between the different building blocks.

Based on a systematic and quantitative analysis of experimental data, the model developed combines concepts, approaches and results of a range of different fields, such as graphene and 2D related materials, polymers science, networks, percolation theory and critical phenomena. The role of interfaces and their nanostructure, as well as the universal behaviour observed from the nano- to the macro- scale and the analogies with charge transport in 1D and 3D systems give considerable importance to this result. In principle, the scheme developed could be used to describe CT in real-life GRM-based systems, such as inks and polymer composites.

Sommario

(abstract in Italian)

L'avvento di tecniche economiche per produrre fogli di materiali con spessore mono-atomico, come il grafene, ha aperto la possibilità di progettare materiali nanostrutturati con proprietà chimico/fisiche preprogrammabili. I sistemi tecnologicamente rilevanti a base di materiali correlati al grafene (GRM) sono principalmente networks di nanofogli bidimensionali distribuiti in modo casuale e altamente difettosi. Sebbene il trasporto di carica (CT) in fogli bidimensionali isolati sia stato ampiamente studiato, il comportamento delle cariche in film ben ordinati di grafene ossido ridotto è stato chiarito solo recentemente. Per descrivere il CT in questi sistemi è stato proposto un modello geometrico a multi-scala in analogia con il caso dei materiali compositi, in cui unità elementari quasi-1D si comportano da additivi conduttivi in una matrice isolante (struttura "*a spaghetti*"). La lunghezza di questi fili quasi-1D è definita dalla lunghezza di localizzazione ξ dei portatori di carica. Nonostante ciò, uno studio esaustivo che correli le proprietà elettriche di networks di GRM 2D con la complessità della struttura e della morfologia del materiale è ancora mancante in letteratura.

Lo scopo di questo lavoro è generalizzare il precedente approccio in modo da indagare il trasporto di carica in film sottili di GRM, studiando il ruolo dell'unità elementare e la sua disposizione nella struttura del film.

Abbiamo confrontato due distinti GRM prodotti al CNR-ISOF: il grafene ossido ridotto (RGO) e il grafene ossido esfoliato elettrochimicamente (EGO), e abbiamo fabbricato film con una differente disposizione dei foglietti utilizzando differenti tecniche di deposizione, quali i) lo *spin-coating*, ii) lo *spray-coating* e iii) la filtrazione assistita dal vuoto. La caratterizzazione multi-scala della struttura dei film è stata eseguita combinando le tecniche di diffrazione di raggi x (XRD) e delle seguenti microscopie: ottica (OM), a forza atomica (AFM) e a scansione di sonda elettronica (SEM). La spettroscopia fotoelettronica a raggi x (XPS) è stata invece impiegata per le analisi chimiche dei film.

Descritto in termini di sistemi policristallini, il CT in film di GRM è stato investigato misurando la resistività elettrica (ρ) in funzione della temperatura T , da valori ambientali fino a pochi K. L'analisi è stata eseguita con il metodo dell'energia di attivazione ridotta: $W(T)$, permettendo di assegnare in modo auto-consistente i differenti regimi di trasporto. Nel caso di film disordinati di RGO, abbiamo ottenuto un eccellente accordo con i risultati riportati in

letteratura. Nello specifico, abbiamo generalizzato il metodo $W(T)$ a causa di un basso rapporto segnale rumore nei dati acquisiti. In questo modo abbiamo mostrato che una corretta analisi del modello di trasporto di tipo ES-VRH permette di descrivere $\rho(T)$, senza il bisogno di invocare transizioni a differenti regimi VRH.

Abbiamo mostrato che la struttura a spaghetti può essere utilizzata per descrivere il CT in tutti i sistemi GRM studiati, sia nel caso di RGO sia in quello di EGO. Inoltre, abbiamo osservato che la lunghezza ξ aumenta con il disordine nella disposizione delle unità elementari (*i.e.* policristallinità) evidenziando gli effetti di meccanismi multi-scala. L'aumento del disordine è legato a un aumento delle possibili orientazioni delle unità elementari e, quindi, a un aumento del numero di configurazioni strutturali. Questa condizione corrisponde a un'ottimizzazione delle interfacce su scala nanometrica e a una più alata probabilità che le cariche "saltino" tra diverse unità elementari.

Basato su un'analisi sistematica e quantitativa dei dati sperimentali, il modello sviluppato combina concetti, approcci e risultati di campi diversi, quali il grafene e i materiali bi-dimensionali, la scienza dei polimeri, i networks, la teoria della percolazione e quella sui fenomeni critici. Il ruolo delle interfacce e della loro nano-struttura, unito al comportamento universale osservato dalla nano-scala alla macro-scala nonché le analogie con il CT in sistemi 1D e 3D forniscono a tali risultati una vasta importanza. In principio, infatti, lo schema sviluppato può essere applicato per descrivere il CT in sistemi realistici a base di GRM, come inchiostri e composti polimerici.

Table of Contents

Abstract.....	i
Introduction	1
Chapter 1 GRAPHENE-RELATED MATERIALS	4
Chapter 2 CHARGE TRANSPORT IN GRM THIN FILMS	15
2.1 CT Models of Disordered Systems.....	16
2.2 Reduced Activation Energy Method - $W(T)$	22
2.3 GO/RGO CT Studies Reported in Literature	25
2.4 First Systematic Approach to Study the CT in RGO Thin Films	28
Chapter 3 SAMPLES FABRICATION.....	42
3.1 GRM Synthesis.....	42
3.2 GRM Films Fabrications.....	44
Chapter 4 CHARACTERIZATION TECHNIQUES.....	56
4.1 Chemical Analysis: XPS	56
4.2 Morphology	64
4.3 Electrical Characterisation.....	75
Chapter 5 CHARACTERIZATION OF GRM THIN FILMS STRUCTURE	83
5.1 Reduced Graphene Oxide (RGO).....	83
5.2 Electrochemically exfoliated GO (EGO).....	90
Chapter 6 NEW PROTOCOL FOR VRH DATA ANALYSIS	96
6.1 General Description of VRH.....	96
6.2 Operative Approach for Fitting Analysis	100
6.3 Results and Discussion	102
Chapter 7 MEASUREMENT OF GRM THIN FILMS CHARGE TRANSPORT.....	106
7.1 The Role of Film Structure.....	107
7.2 The Role of Film Building Block: EGO vs. RGO.....	117
Concluding Remarks and Outlook	124
Appendix A.....	126

A.1 Complements of CT Theories	126
A.2 Review of Literature about CT Studies in RGO Systems	129
A.3 Additional Data about GRM	131
List of Figures	137
List of Acronyms.....	142
List of Activities during the PhD.....	144
Acknowledgments	147

Introduction

Graphene and 2-dimensional (2D) materials are nowadays found everywhere, from fundamental research to market products. Among intrinsic peculiarities of 2D materials there are the extremely high surface-to-volume ratio and the role of interfaces, that constitute almost all the object and give the material most of the observed unique properties. Both features can be exploited as advantages in devices design compared to their bulk equivalent. Furthermore, the nanometric confinement in one direction of 2D objects forces to think in terms of quantum physics. It is just through a quantum description that many of the extraordinary computational capabilities of common electronic devices can be explained.

2D materials are often not employed as single sheets, but they are combined together in films and similar structures [1]. These structures contain more than hundreds of thousands of 2D particles piled or stacked in different ways, with a certain degree of control. The final device behaviour is intimately connected with the interaction among single components, that are the 2D particles. Then, the properties of the structure can derive in a complex manner from its basic components, as well as from the way they combine. In this sense, they are referred as network structures. Common examples are found in printed traces of a multi-functional ink [2] or in conductive fillers in a polymer matrix, *i.e.* a composite [3]. In the last case, for instance, the structure transits from an insulating to a conducting state once a certain amount of fillers is inserted in the polymer and a certain degree of interconnections among filler particles is reached [4].

Most of literature studies about 2D materials-based devices emphasise the operational properties and figure of merits of the final system. However, supported by the occurrence of large particle-particle junction resistance, a single-sheet approach is often used to explain the basic mechanisms that lead to mentioned original and innovative device properties. In this approach, 2D nano- or micro-sheets that compose the structure are disentangled from each other and the role of the network structure plays a minor role. This is in strict contrast to the way CT is treated and described in polymers and common organic molecular materials [5].

We choose graphene-related materials (GRM) because their high potential for being used in commercial devices, as well as the related massive research that leads to different tools to assemble them in various network structures. Graphene oxide (GO) and its reduced form, in particular, can be thought of as toy models for a lot of 2D materials, comprising both structural disorder and chemical functionalities while retaining a main mono-atomic, graphene-like scaffold.

This work focuses on the way charge carriers move in GRM thin films, fabricated to be as close as possible to realistic systems. The motion of charged particles, commonly referred to as charge transport (CT), is of primary interest for materials and process design. CT is a fundamental mechanism of matter playing an important role in various phenomena occurring in a material, from current conduction to thermal management [6]. Several models and theories have been proposed in the years for describing CT in disordered organic systems. Despite that, no broad agreement has been found in the community for GRM network systems and questions are still open when dealing with their CT nature.

We employ a phenomenological approach to study charge transport in our graphene-related materials thin films. The approach has a microscopical character because the measured parameters - *e.g.* resistivity - are associated to the film as a whole entity. Starting from these parameters, we then try to explain the behaviour of the charge motion through the sub-micro components - *i.e.* GRM sheets - constituting the film. The physical and chemical properties of both GRM sheet and the final films are characterised to have the best possible comprehension of the system. The final aim is to correlate the network structure and the material characteristic to the charge transport mechanisms occurring in the thin film.

Chapter 1 briefly introduces graphene and graphene-related materials, underlying the nomenclature ambiguities often found in literature. Chapter 2 describes the state of the art of charge transport research in RGO systems. We also discuss here issues and recent advances about the topic.

The description of the used thin film fabrication methods and of the related characterization techniques is presented in the following two Chapters (Chapter 3 and Chapter 4, respectively).

Chapter 5 is dedicated to the measured properties of both GRM materials and GRM films. A new protocol used for the analysis of low temperature charge transport in GRM thin films is presented in Chapter 6.

The last Chapter 7) shows and discusses the results on charge transport in GRM thin films. The roles of the network structure and of the basic component (*i.e.* building block) forming the film are treated separately.

References

- [1] Lin, Z., *et al.*, *Van der Waals thin-film electronics*. *Nature Electronics* **2**, 9, p. 378-388 (2019). www.doi.org/10.1038/s41928-019-0301-7
- [2] Kelly, A.G., *et al.*, *All-printed thin-film transistors from networks of liquid-exfoliated nanosheets*. *Science* **356**, 6333, p. 69 (2017). www.doi.org/10.1126/science.aal4062
- [3] Bauhofer, W., *et al.*, *A review and analysis of electrical percolation in carbon nanotube polymer composites*. *Composites Science and Technology* **69**, 10, p. 1486-1498 (2009). www.doi.org/10.1016/j.compscitech.2008.06.018; Deng, H., *et al.*, *Progress on the morphological control of conductive network in conductive polymer composites and the use as electroactive multifunctional materials*. *Progress in Polymer Science* **39**, 4, p. 627-655 (2014). www.doi.org/10.1016/j.progpolymsci.2013.07.007
- [4] Zhan, Y., *et al.*, *Enhancing electrical conductivity of rubber composites by constructing interconnected network of self-assembled graphene with latex mixing*. *Journal of Materials Chemistry* **22**, 21, p. 10464-10468 (2012). www.doi.org/10.1039/C2JM31293J
- [5] Noriega, R., *et al.*, *A general relationship between disorder, aggregation and charge transport in conjugated polymers*. *Nature Materials* **12**, 11, p. 1038-1044 (2013). www.doi.org/10.1038/nmat3722
- [6] Kang, S.D., *et al.*, *Charge-transport model for conducting polymers*. *Nature Materials* **16**, 2, p. 252-257 (2017). www.doi.org/10.1038/nmat4784; Tritt, T.M., *et al.*, *Thermoelectric Materials, Phenomena, and Applications: A Bird's Eye View*. *MRS Bulletin* **31**, 3, p. 188-198 (2011). www.doi.org/10.1557/mrs2006.44

Chapter 1

GRAPHENE-RELATED MATERIALS

The purpose of this chapter is to give an overview of graphene-based materials, going in a direction of increasing structural and chemical complexity: from single 2D sheets to 3D networks.

Graphene is the “Nobel prize material” that boosted the huge interest in “flatland” (*i.e.* b-dimensional objects) of the 21st century [8]. Graphene is composed by a mesoscopic sheet of carbon atoms that are arranged in a poly-aromatic, hexagonal ring array, as visualised in Figure 1-1a. This array can be looked at as a mono-crystalline layer of graphite, from which the name comes from [9]. Carbon atoms in graphene are indeed in the sp^2 -hybridized state, where each carbon atom is attached to three other carbon atoms with a bond angle between atoms of 120° . These planar bonds involve σ orbital. The widely known (low energy) electronic structure of graphene is determined by the

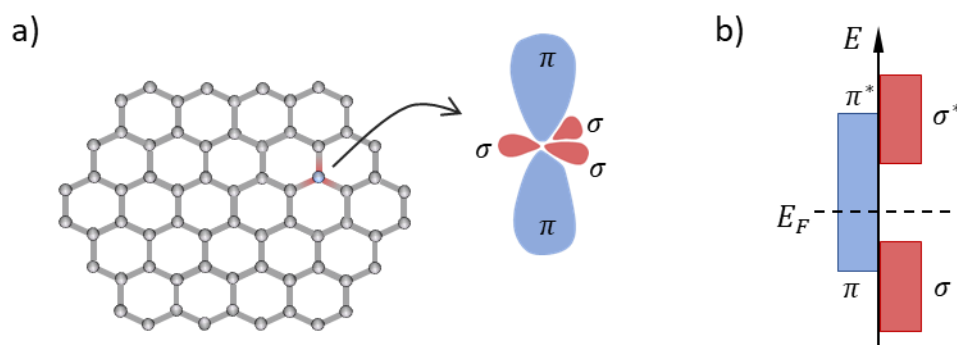


*Figure 1-1. (a) Chemical structure of graphene: carbon atoms are arranged in a honeycomb lattice. The scheme on the right depicts the three σ orbitals (*i.e.* sp^2) and the π orbital (*i.e.* p_z), that is perpendicular to the sheet. σ orbitals form in-plane σ bonds that strongly connect the carbon atoms and are responsible for the structural properties of the graphene sheet.*

(b) The bonding and antibonding electronic bands for σ orbitals and for π orbitals. Because σ bands are separated by a quite large gap, only π bands are usually considered for electronic properties of graphene. Images were inspired from ref. [7].

remaining two p_z , or π , orbitals in its unit cell. They mix to form two π bands that may be thought of as bonding, that is the lower energy valence band, and anti-bonding, the higher energy conduction band. Around the corners of the Brillouin zone, called K points, the bonding-antibonding bands joins with a linear dispersion function and there is no gap at E_F , as shown in Fig. 1-1b. The consequence of this electronic structure is that charges in graphene behave as massless, “slow” relativistic particles, obeying the Dirac-Weyl equation of quantum electrodynamics [10].

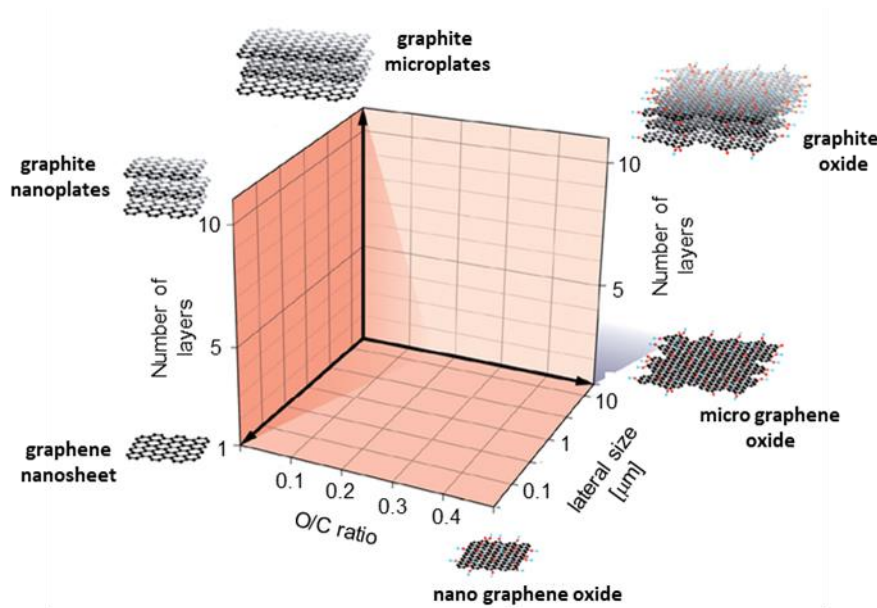


Figure 1-2. Classification of graphene-related materials (GRMs) according to their chemical state (i.e oxygen to carbon ratio), their average lateral size and their average number of layers. The image is from ref. [11].

A set of graphene layers (>10) vertically stacked through Wan der Waals forces forms crystalline graphite. Exploiting these weak interlayer forces, in 2004, graphene was isolated for the first time by graphite mechanical exfoliation [12]. Since that moment, graphene has attracted great attention in research community for its physical properties, including exceedingly high charge carrier mobility, current-carrying capacity, high mechanical strength at nanoscale, and elevated thermal conductivity [13]. In addition, its truly 2D and highly anisotropic shape makes graphene an interesting chemical platform [14]. However, as common, the progresses in graphene scientific knowledge have hardly match commercial challenges. While the best performances of (single-layer) graphene

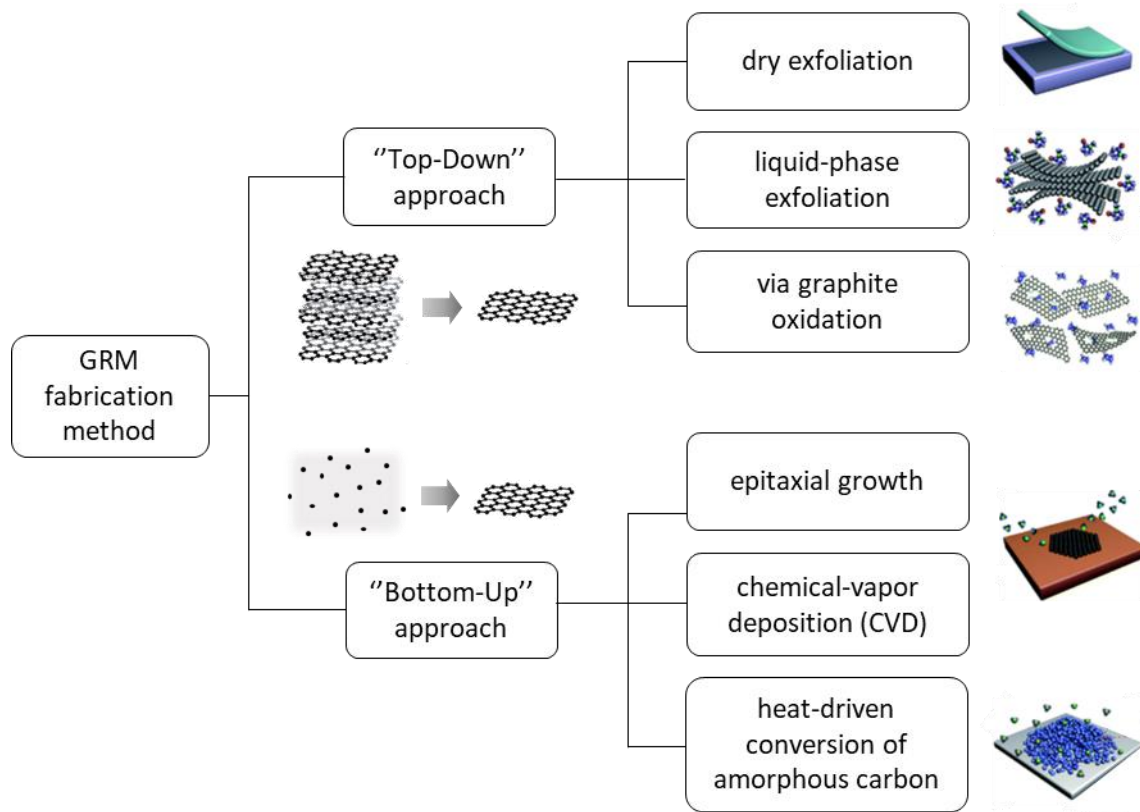


Figure 1-3. List of some graphene and GRM production methods classified by the two basic approaches in nanofabrication: "top-down" or "bottom-up".

have been observed in mechanically cleaved sheets, this route is not scalable and gives a low yield (a few monolayers per mm^2 of substrate area). Hence, various fabrication techniques and different bi-dimensional (2D) materials have been investigated.

In this regard, graphene-related materials (GRM) are a broad family of materials with the aromatic carbon sp^2 chemical structure as a main scaffold. They own a planar or sheet-like structure with thickness ranging from mono-atomic one to few nm and sizes from hundreds of nm to several tens of μm . Chemical functionalities and topological defects could be present, based on the GRM synthesis method and its processing history.

Relevant parameters to distinguish GRM are the exfoliation grade, quantified by the number of layers, the particle lateral size and the oxidation degree, quantified by the oxygen-to-carbon atomic ratio (O/C) [11] (see Figure 1-2). Adding to these three, the bulk density represents a fourth parameters, that is important for handling, processing and transporting GRM in powder form [15].

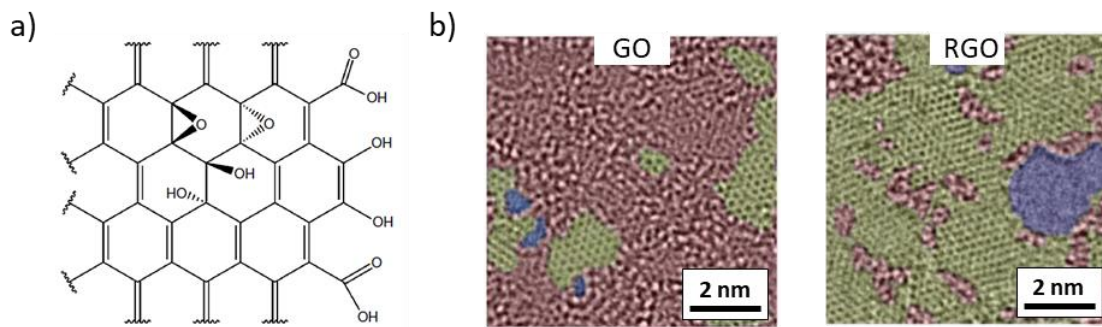


Figure 1-4. (a) Scheme of Lerf and Klinowski structural model for GO. Image from [16]. (b) Digital coloured, transmission electron microscopy (TEM) images of GO and RGO. sp^2 regions are depicted in yellow, while functionalised regions in red. Blue areas represent holes in the materials. The increase of $C sp^2$ is evident in RGO compared to GO. Images from [17].

While bottom-up approaches are common of high-quality, single-layer graphene production, GRM are commonly synthesized via top-down approaches. Lower-cost and, in some cases, suitability for kg-scale production are the main reasons for preferring the latter routes [18]. Different GRM fabrication techniques are cited in Figure 1-3.

The most famous among GRM is – chemical synthesized – graphene oxide (GO). Graphene oxide is made of mono-atomic carbon sheets containing oxygen functional groups. Thanks to these oxygen molecules, GO water suspensions with long-term stability can be easily produced, making possible the use of wet-based chemistry and the integration of the material with current industry processing methods for functional composites, printed electronics, antennas and energy storage applications [19]. This has promoted the high spread of graphene and GRM both in research field and in industry one.

Different solution-based preparations are used for GO synthesis [20]. All of them have in common the use of concentrate acids to oxidise bulk graphite while applying mechanical stresses (*e.g.*, by stirring or by ultrasonication of the suspension) to exfoliate graphite planes. The chemistry of GO sheet is still a debated topic and many structural models have been proposed in the years [16]. The most cited model is represented in Figure 1-4a and attributed to Lerf and Klinowski [21]. In their model, GO sheets are made of pure sp^2 hybridised carbon atoms regions with honeycomb (graphene) lattice structure and of oxidised region with sp^3 hybridised carbon atoms. These two kinds of areas are randomly

distributed in the sheet [17,22], as proved by high resolution, aberration corrected transmission electron microscopy (TEM) images shown in 1-4b. In this picture, oxidised GO domains contain epoxy and hydroxyl (tertiary alcohol) functional groups, while carboxyl and hydroxyl groups decorate the edge of the sheet. This was theorised by interpreting solid-state NMR spectra of specifically functionalised GO sheets, in which each functional group is substituted by another using a suitable reaction. However, presence of functional groups at defects/holes edges inside the sheet have not been fully clarified. Other “static” structural models differentiate for the spatial/numeric distribution and sometimes the kind of chemical functionalities present, such as the one proposed by Szabó *et al* [23]. By considering GO slightly acid character, Dimiev *et al* [24] formulated the dynamic structural model (DSM) that extends the comprehension about GO formation and structural evolution in suspension. In their findings, GO does not contain any pre-existing acid chemical groups. It is through interaction with water that C-C bonds are cleaved and vinylogous carboxylic acids are formed on the edges, both on the external perimeter and on the internal holes. Hence, the DSM propose a scheme where, based on the surrounding environment, GO modifies the distribution of oxygen functional groups proposed by Lerf-Klinowski.

Oxygen functionalities lead to the higher (suspension) stability of GO sheets in water [25] and simplify the chemical modifications of the material (for novel properties) [26], but also disrupt aromatic sp^2 regions and contribute to its insulating character. In fact, a full sp^3 C structure owns a large energy gap (around 5 eV), such as occurs in diamond crystal. Isolated sp^2 region contribute with localised energy levels inside the gap. By increasing the C sp^2/sp^3 ratio, the localised levels densify and join to the existing bands, causing a decrease of the energy gap [27].

A reduction process is thus needed to eliminate the functional groups and to partially restore the electrical and thermal properties of graphene. Reduction could be carried out by chemical or by physical means. In chemical reduction, GO is let to react with chemical agents, such as hydrazine [28], L-ascorbic acid [29] or amino acids [30]. While chemical reduction is technically simple and convenient for industry processing, the final material does not often match the required properties and further treatments are needed. On the other hand, physical reduction methods allow to eliminate as much as oxygen

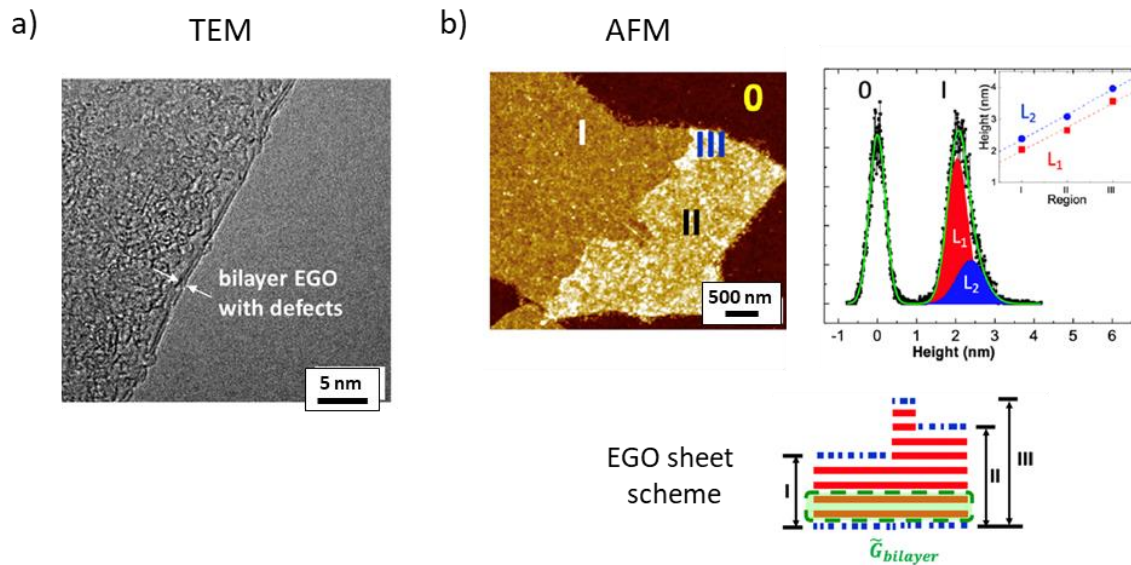


Figure 1-5. (a) High resolution TEM image of a EGO sheet. The sheet edge cross section is highlighted, showing a bilayer structure of the sheet. (b) On the left, a AFM image of a EGO sheet over a SiO₂ substrate; on the right, corresponding AFM histogram analysis with heights (see inset) measured at different regions, as marked in the image. The height peak for each layer is fitted with a main sharp component (L_1) plus a broader component (L_2) due to debris. The scheme at the bottom represents the suggested EGO morphology. Figures adapted from [33].

functionalities possible. They can be mostly applied to the final device or coating material only. Among them, there are thermal treatment [31] and light, *i.e.* laser, exposure [32]. It is known that the increase of sp^2 aromatic regions or, from the other side, the decrease of sp^3 ones, is correlated with an increase of the electrical conductivity of the RGO sheet. However, despite high reduced GO owns low oxygen content with a O/C ratio typically below 0.02, topological defects and holes remain in the sheet and hamper the possibility of achieving the theoretical conductivity of defect free, single-layer graphene [34]. This should be considered when using RGO.

A less known material that exhibit representative properties for quasi 2D (multi-layer), defective GRM is electrochemically exfoliated GO (EGO). EGO is fabricated by electrochemical mild oxidation and exfoliation of graphite. The synthesis process is fast, low cost and it gives high yield compared to other approaches [35,36], such as sonication-assisted liquid phase exfoliation. Moreover, it allows step-controlled oxidation of graphite during the synthesis. Hence, EGO flakes are usually less oxidated with respect to GO one

and have measurable conductivity without the need of further treatments. They also own a more complex morphology with respect to GO/RGO counterpart. TEM analysis have highlighted homogeneous micrometre-size flakes with a mixture of defective few layers structures at the edges. Combining TEM results (Figure 1-5a) with x-ray diffraction measurements, it has been suggested that EGO flakes are (partially) oxidised only on top and bottom sites, *i.e.* edge sites. The thickness of these flakes ranges from around 2 nm to tens of nm, as measured by atomic force microscopy. EGO is thus a few-layer “sandwich-like” structure consisting of vertically stacked, defective graphene bilayer sheets and having oxygen functionalised edge layers [33].

The disadvantage of EGO is that it only disperses well in high boiling point solvents (*e.g.*, Dimethylformamide (DMF); N-methyl-2-pyrrolidone (NMP)) and at low concentration (<1g/L). Depositions parameters should be adapted to the solvent characteristics and post-processing could be needed to fully remove solvent traces. As for other low oxidised GRMs, dispersion in water could still be viable by employing certain surfactants, such as sodium dodecyl benzene sulfonate [37] or sodium cholate [38]. On the other hand, surfactant molecules are nearly impossible to remove from GRM layers and they will be present in final devices. Because surfactants own uninteresting electronic properties, they can negatively affect charge transport and device performances [39]. A possible route to circumvent these issues is using a solvent exchange process. EGO is transferred from the high boiling point solvent, where it was synthesised, to a lower boiling point one, like 2-propanol (IPA) or acetonitrile.

Despite photonics and spintronics futuristic prototypes, RGO, EGO and GRM are hardly used as isolated particles in current realistic devices. Indeed, they are commonly processed and assembled to form films, membranes and macroscopic, nanostructured sheets or dispersed in polymeric matrixes. These are partially ordered structures where GRM 2D sheets are stacked together through both intralayer and interlayer crosslinks, forming networks. Few examples are presented in Figure 1-6.

One of the main industry relevant, semi-finished manufacture comes under the name of graphene paper [40]. The word is generically used to indicate a wide, micrometric-thick sheet made of assembled GRM 2D particles. The main peculiarity is a pre-programmed elevated electrical conductivity combined with good mechanical properties which makes

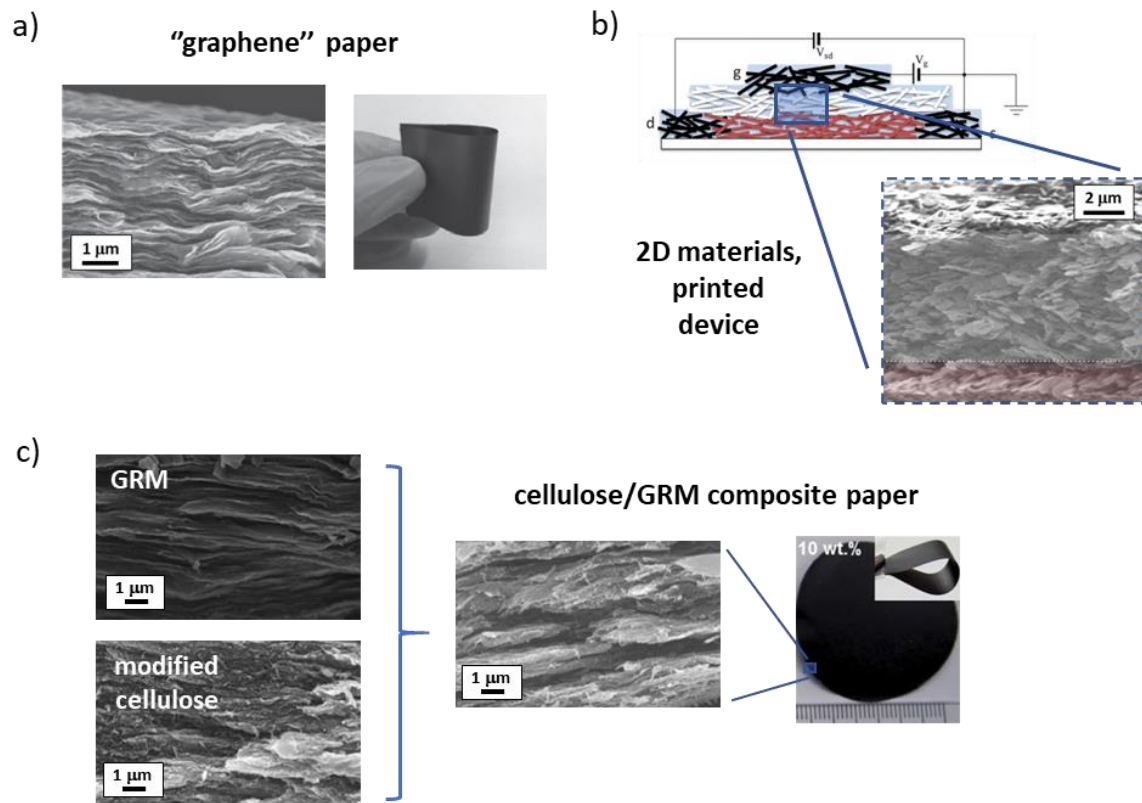


Figure 1-6. Different examples of the use of GRM in realistic devices. Together with a digital photograph or a scheme, a cross-section SEM micrograph is shown of: (a) “Graphene” paper (adapted from [47]); (b) a printed transistor (adapted from [2]); and (c) a cellulose/GRM composite (adapted from [48]).

graphene paper suitable both as electrodes [41], thermal management interface [42] and part of composite layered materials [43]. Graphene paper can be fabricated by different techniques, such as filtration [44], mechanical pressing [45], blade-coating [46] and electro spray deposition [47].

Thin films of GRM are also typically found in novel printed, electronic devices [2]. In fact, the use of 2D nano- and micro-sheets permits to create inks with on-demand properties. Compared to metal nanoparticle inks, GRM inks allows flexibility in the processing methods, low costs and are compatible with a wide range of substrates [39,49]. We underline that the conductivity of these interconnected architectures, and so their CT phenomenology, is closely connected with their microscopic network morphology [50]. GRM sheets are not only assembled alone, but they can be frequently found as conductive fillers and mechanical reinforcement in composite materials [51]. In this regard, a key

aspect is how GRM combines with the presence of the additional material. The fabrication of a GRM composite can occur (i) by functionalising the GRM sheets before assembling them; (ii) via a layer-by-layer hierarchy with other materials; or (iii) by solution mixing GRM sheets with a polymeric host [52]. In last case, the formation of GRM interconnected network structures inside the hosting polymer is highly desirable for achieving good electrical and mechanical properties [53]. We also underline that in (i) the GRM sheets act as a main scaffold of the structure, while in (iii) their content is a small percentage of the total volume. However, the discussion of these systems is out-of-the scope of the present work.

1.1 References

- [2] Kelly, A.G., *et al.*, *All-printed thin-film transistors from networks of liquid-exfoliated nanosheets*. *Science* **356**, 6333, p. 69 (2017). www.doi.org/10.1126/science.aal4062
- [7] Charlier, J., *et al.*, *Electronic properties of carbon-based nanostructures*, in *Introduction to Graphene-Based Nanomaterials: From Electronic Structure to Quantum Transport*, J.-C. Charlier, L.E.F. Foa Torres, *et al.*, Cambridge University Press, p. 11-90 (2014). www.doi.org/DOI:10.1017/CBO9781139344364.003
- [8] Novoselov, K.S., *Nobel Lecture: Graphene: Materials in the Flatland*. *Reviews of Modern Physics* **83**, 3, p. 837-849 (2011). www.doi.org/10.1103/RevModPhys.83.837
- [9] Boehm, H.P., *et al.*, *Nomenclature and terminology of graphite intercalation compounds*. *Carbon* **24**, 2, p. 241-245 (1986). [www.doi.org/10.1016/0008-6223\(86\)90126-0](http://www.doi.org/10.1016/0008-6223(86)90126-0)
- [10] Castro Neto, A.H., *et al.*, *The electronic properties of graphene*. *Reviews of Modern Physics* **81**, 1, p. 109-162 (2009). www.doi.org/10.1103/RevModPhys.81.109
- [11] Wick, P., *et al.*, *Classification Framework for Graphene-Based Materials*. *Angewandte Chemie International Edition* **53**, 30, p. 7714-7718 (2014). www.doi.org/10.1002/anie.201403335
- [12] Novoselov, K.S., *et al.*, *Electric Field Effect in Atomically Thin Carbon Films*. *Science* **306**, 5696, p. 666-669 (2004). www.doi.org/10.1126/science.1102896
- [13] Fuhrer, M.S., *et al.*, *Graphene: Materially Better Carbon*. *MRS Bulletin* **35**, 4, p. 289-295 (2011). www.doi.org/10.1557/mrs2010.551
- [14] Palermo, V., *Not a molecule, not a polymer, not a substrate... the many faces of graphene as a chemical platform*. *Chemical Communications* **49**, 28, p. 2848-2857 (2013). www.doi.org/10.1039/C3CC37474B
- [15] Kovtun, A., *et al.*, *Benchmarking of graphene-based materials: real commercial products versus ideal graphene*. *2D Materials* **6**, 2, p. 025006 (2019). www.doi.org/10.1088/2053-1583/aafc6e
- [16] Dimiev, A.M., *Mechanism of Formation and Chemical Structure of Graphene Oxide*, in *Graphene Oxide*, A.M. Dimiev and E. S., Wiley, p. 36-84 (2016). www.doi.org/10.1002/9781119069447.ch2
- [17] Erickson, K., *et al.*, *Determination of the Local Chemical Structure of Graphene Oxide and Reduced Graphene Oxide*. *Advanced Materials* **22**, 40, p. 4467-4472 (2010). www.doi.org/10.1002/adma.201000732
- [18] Dong, L., *et al.*, *Reactivity-Controlled Preparation of Ultralarge Graphene Oxide by Chemical Expansion of Graphite*. *Chemistry of Materials* **29**, 2, p. 564-572 (2017). www.doi.org/10.1021/acs.chemmater.6b03748; Ferrari, A.C., *et al.*, *Science and technology roadmap for graphene, related two-dimensional crystals, and hybrid systems*. *Nanoscale* **7**, 11, p. 4598-4810 (2015). www.doi.org/10.1039/C4NR01600A; Paton, K.R., *et al.*, *Scalable production of large quantities of defect-free few-layer graphene by shear exfoliation in liquids*. *Nature Materials* **13**, 6, p. 624-630 (2014). www.doi.org/10.1038/nmat3944

- [19] Graphene Flagship Annual Report. 2019.
- [20] Poh, H.L., *et al.*, *Graphenes prepared by Staudenmaier, Hofmann and Hummers methods with consequent thermal exfoliation exhibit very different electrochemical properties*. *Nanoscale* **4**, 11, p. 3515-22 (2012). www.doi.org/10.1039/c2nr30490b
- [21] Lerf, A., *et al.*, *Structure of Graphite Oxide Revisited*. *The Journal of Physical Chemistry B* **102**, 23, p. 4477-4482 (1998). www.doi.org/10.1021/jp9731821
- [22] Gómez-Navarro, C., *et al.*, *Atomic Structure of Reduced Graphene Oxide*. *Nano Letters* **10**, 4, p. 1144-1148 (2010). www.doi.org/10.1021/nl9031617
- [23] Szabó, T., *et al.*, *Evolution of Surface Functional Groups in a Series of Progressively Oxidized Graphite Oxides*. *Chemistry of Materials* **18**, 11, p. 2740-2749 (2006). www.doi.org/10.1021/cm060258+
- [24] Dimiev, A.M., *et al.*, *Graphene Oxide. Origin of Acidity, Its Instability in Water, and a New Dynamic Structural Model*. *ACS Nano* **7**, 1, p. 576-588 (2013). www.doi.org/10.1021/nn3047378
- [25] Neklyudov, V.V., *et al.*, *New insights into the solubility of graphene oxide in water and alcohols*. *Physical Chemistry Chemical Physics* **19**, 26, p. 17000-17008 (2017). www.doi.org/10.1039/C7CP02303K
- [26] Yu, W., *et al.*, *Progress in the functional modification of graphene/graphene oxide: a review*. *RSC Advances* **10**, 26, p. 15328-15345 (2020). www.doi.org/10.1039/D0RA01068E
- [27] Takai, K., *et al.*, *Structure and electronic properties of a nongraphitic disordered carbon system and its heat-treatment effects*. *Physical Review B* **67**, 21, p. 214202 (2003). www.doi.org/10.1103/PhysRevB.67.214202
- [28] Park, S., *et al.*, *Hydrazine-reduction of graphite- and graphene oxide*. *Carbon* **49**, 9, p. 3019-3023 (2011). www.doi.org/10.1016/j.carbon.2011.02.071; Stankovich, S., *et al.*, *Synthesis of graphene-based nanosheets via chemical reduction of exfoliated graphite oxide*. *Carbon* **45**, 7, p. 1558-1565 (2007). www.doi.org/10.1016/j.carbon.2007.02.034
- [29] Legge, E.J., *et al.*, *Physicochemical characterisation of reduced graphene oxide for conductive thin films*. *RSC Advances* **8**, 65, p. 37540-37549 (2018). www.doi.org/10.1039/C8RA08849G; Zhang, J., *et al.*, *Reduction of graphene oxide via ascorbic acid*. *Chemical Communications* **46**, 7, p. 1112-1114 (2010). www.doi.org/10.1039/B917705A
- [30] Fernández-Merino, M.J., *et al.*, *Identifying efficient natural bioreductants for the preparation of graphene and graphene-metal nanoparticle hybrids with enhanced catalytic activity from graphite oxide*. *Carbon* **63**, p. 30-44 (2013). www.doi.org/10.1016/j.carbon.2013.06.034
- [31] Acik, M., *et al.*, *The Role of Oxygen during Thermal Reduction of Graphene Oxide Studied by Infrared Absorption Spectroscopy*. *The Journal of Physical Chemistry C* **115**, 40, p. 19761-19781 (2011). www.doi.org/10.1021/jp2052618; Ganguly, A., *et al.*, *Probing the Thermal Deoxygenation of Graphene Oxide Using High-Resolution In Situ X-ray-Based Spectroscopies*. *The Journal of Physical Chemistry C* **115**, 34, p. 17009-17019 (2011). www.doi.org/10.1021/jp203741y
- [32] Evlashin, S., *et al.*, *Controllable Laser Reduction of Graphene Oxide Films for Photoelectronic Applications*. *ACS Applied Materials & Interfaces* **8**, 42, p. 28880-28887 (2016). www.doi.org/10.1021/acsami.6b10145; Yar, A., *et al.*, *Physical reduction of graphene oxide for supercapacitive charge storage*. *Journal of Alloys and Compounds* **822**, p. 153636 (2020). www.doi.org/10.1016/j.jallcom.2019.153636
- [33] Xia, Z., *et al.*, *Dispersion Stability and Surface Morphology Study of Electrochemically Exfoliated Bilayer Graphene Oxide*. *The Journal of Physical Chemistry C* **123**, 24, p. 15122-15130 (2019). www.doi.org/10.1021/acs.jpcc.9b03395
- [34] Mattevi, C., *et al.*, *Evolution of Electrical, Chemical, and Structural Properties of Transparent and Conducting Chemically Derived Graphene Thin Films*. *Advanced Functional Materials* **19**, 16, p. 2577-2583 (2009). www.doi.org/10.1002/adfm.200900166
- [35] Eredia, M., *et al.*, *Morphology and Electronic Properties of Electrochemically Exfoliated Graphene*. *The Journal of Physical Chemistry Letters* **8**, 14, p. 3347-3355 (2017). www.doi.org/10.1021/acs.jpcllett.7b01301
- [36] Xia, Z.Y., *et al.*, *Synergic Exfoliation of Graphene with Organic Molecules and Inorganic Ions for the Electrochemical Production of Flexible Electrodes*. *ChemPlusChem* **79**, 3, p. 439-446 (2014). www.doi.org/10.1002/cplu.201300375

- [37] Lotya, M., et al., *Liquid Phase Production of Graphene by Exfoliation of Graphite in Surfactant/Water Solutions*. *Journal of the American Chemical Society* **131**, 10, p. 3611-3620 (2009). www.doi.org/10.1021/ja807449u
- [38] Green, A.A., et al., *Solution Phase Production of Graphene with Controlled Thickness via Density Differentiation*. *Nano Letters* **9**, 12, p. 4031-4036 (2009). www.doi.org/10.1021/nl902200b
- [39] Tran, T.S., et al., *Graphene inks for printed flexible electronics: Graphene dispersions, ink formulations, printing techniques and applications*. *Advances in Colloid and Interface Science* **261**, p. 41-61 (2018). www.doi.org/10.1016/j.cis.2018.09.003
- [40] Chen, H., et al., *Mechanically Strong, Electrically Conductive, and Biocompatible Graphene Paper*. *Advanced Materials* **20**, 18, p. 3557-3561 (2008). www.doi.org/10.1002/adma.200800757
- [41] Wang, C., et al., *Electrochemical Properties of Graphene Paper Electrodes Used in Lithium Batteries*. *Chemistry of Materials* **21**, 13, p. 2604-2606 (2009). www.doi.org/10.1021/cm900764n
- [42] Liu, L., et al., *Exceptional electrical and thermal transport properties in tunable all-graphene papers*. *RSC Advances* **5**, 92, p. 75239-75247 (2015). www.doi.org/10.1039/C5RA15533A
- [43] Wang, D.-W., et al., *Fabrication of Graphene/Polyaniline Composite Paper via In Situ Anodic Electropolymerization for High-Performance Flexible Electrode*. *ACS Nano* **3**, 7, p. 1745-1752 (2009). www.doi.org/10.1021/nn900297m
- [44] Dikin, D.A., et al., *Preparation and characterization of graphene oxide paper*. *Nature* **448**, 7152, p. 457-460 (2007). www.doi.org/10.1038/nature06016
- [45] Liu, F., et al., *Folded Structured Graphene Paper for High Performance Electrode Materials*. *Advanced Materials* **24**, 8, p. 1089-1094 (2012). www.doi.org/10.1002/adma.201104691
- [46] Guo, Y., et al., *Ultrathin, Washable, and Large-Area Graphene Papers for Personal Thermal Management*. *Small* **13**, 44, p. 1702645 (2017). www.doi.org/10.1002/smll.201702645
- [47] Xin, G., et al., *Large-Area Freestanding Graphene Paper for Superior Thermal Management*. *Advanced Materials* **26**, 26, p. 4521-4526 (2014). www.doi.org/10.1002/adma.201400951
- [48] Luong, N.D., et al., *Graphene/cellulose nanocomposite paper with high electrical and mechanical performances*. *Journal of Materials Chemistry* **21**, 36, p. 13991-13998 (2011). www.doi.org/10.1039/C1JM12134K
- [49] He, P., et al., *Screen-Printing of a Highly Conductive Graphene Ink for Flexible Printed Electronics*. *ACS Applied Materials & Interfaces* **11**, 35, p. 32225-32234 (2019). www.doi.org/10.1021/acsami.9b04589
- [50] Barwich, S., et al., *On the relationship between morphology and conductivity in nanosheet networks*. *Carbon* **171**, p. 306-319 (2021). www.doi.org/10.1016/j.carbon.2020.09.015
- [51] Kuilla, T., et al., *Recent advances in graphene based polymer composites*. *Progress in Polymer Science* **35**, 11, p. 1350-1375 (2010). www.doi.org/10.1016/j.progpolymsci.2010.07.005
- [52] Huang, X., et al., *Graphene-based composites*. *Chemical Society Reviews* **41**, 2, p. 666-686 (2012). www.doi.org/10.1039/C1CS15078B
- [53] Alekseev, A., et al., *Local Organization of Graphene Network Inside Graphene/Polymer Composites*. *Advanced Functional Materials* **22**, 6, p. 1311-1318 (2012). www.doi.org/10.1002/adfm.201101796; Wang, P., et al., *Constructing 3D Graphene Networks in Polymer Composites for Significantly Improved Electrical and Mechanical Properties*. *ACS Applied Materials & Interfaces* **9**, 26, p. 22006-22017 (2017). www.doi.org/10.1021/acsami.7b07328

Chapter 2

CHARGE TRANSPORT IN GRM THIN FILMS

The purpose of this chapter is discussing the different models used to describe charge transport in disordered systems and presenting the current state-of-the-art of charge transport in RGO thin films.

Charge transport (CT) in single sheet GRM systems has been investigated in the past and it has nowadays an established theory [54-57]. On the other hand, the motion of charge in thin films of randomly stacked GRM sheets has a less clear consensus: different models have been proposed in literature, often in apparent contradiction to one another.

In the case of GRM thin films the charge transport differs intrinsically from that of the single sheet as the structural and the electrical continuity of the GRM network is given by contact regions between different sheets. For this reason, the transport mechanism at the sheet-to-sheet interface plays a crucial role in the electrical behaviour of the overall thin film.

As described in Chapter 1, graphene oxide (GO) is a purely 2D sheet showing a complex in-plane nano-texturing. Because of the high processability, GO allows to easily prepare thin films with tuned morphological, chemical and electrical properties resulting as the suitable test-bed material to study the role of sheet-to-sheet interface transport mechanisms.

However, even in the case of GO (and RGO) thin films there is still no general agreement between the results presented in the literature. Several CT models were reported explain the experimental electrical features, ranging from hopping transport [58-60], thermal activation [61,62], charges tunnelling motion [63], and even band-like transport [64].

One of the most widely used physical observables to study charge transport is the electrical resistivity as function of temperature: $\rho(T)$, or the electrical conductivity: $\sigma(T) = 1/\rho(T)$. Differences in the proposed models can be ascribed to a wide range of 2D/3D architectures and the disordered arrangement of GO/RGO sheets forming thin

films. A further critical issue is related to the $\rho(T)$ data analysis reported in the literature and of which we can identify three approaches: (i) a qualitative comparison of different models by data analysis in different plots [65], (ii) a linear combination of different superimposing models [63] or (iii) the use of a self-consistent way based on the logarithmic temperature derivative of resistivity [55]. The first two approaches present difficulties and inaccuracies, while the third approach it has only recently been used systematically [66].

This Chapter is divided in four Sections. The first one introduces the main models developed to study charge transport phenomena in disordered systems. The CT in GRM networks is briefly reviewed in the second Section, underlying the open issues. Then, the reduced activation energy method is presented. In last Section, we describe the first systematic study of RGO thin films recently published.

2.1 CT Models of Disordered Systems

In general, the electrical properties of a conducting organic materials depend on the spatial and energy distribution of their charge carriers, *i.e.* density of available energy states (DoS), and on the coupling between neighbouring elements constituting the organic structure [67]. If the coupling between elements is strong, the π -electrons can be delocalized over a wider zone of the material; the available states are then assumed to be delocalized states. The transport of charges via delocalized states is thus well described by a band-like transport theory, in analogy with inorganic crystalline semiconductors.

On the other hand, if the coupling between adjacent elements is weak, the delocalization of the π -electrons is limited to one or a few molecules; the available states are then assumed to be localized states. In a seminal work [68], Anderson associated the decrease of molecular coupling and, so, the rise of localization effect to disorder in the system. In this case, charge carriers must somehow “jump” from their localised state to a neighbouring unoccupied state to move into the material and give rise to a current flow. This electrical behaviour is broadly named hopping transport.

Thus, the way a molecule assembles with other molecules in the final structure has a deep influence on electrical properties of the final structure.

A remark should be made in addressing “disorder”: in literature, the term is used to indicate different phenomena [69]. We try to be as more specific as possible when talking of disorder by specifying the nature and the context. Disorder can be found in the distribution of available energy states, that are the energetic levels of molecules composing the systems, or in the relative positions and orientations of the different building blocks. In the first case, we refer to energetic disorder, while we talk of structural disorder in the second case. Chemical impurities and/or functionalities are often the cause of one/or both these two types of disorder. Another distinction for disorder is found in its time evolution. Disorder can be static or dynamic based on a faster or a slower motion of charge carriers with respect to the energy landscape. In the GRM systems with a fair amount of (fixed) chemical impurities, the static disorder often dominates and there is no need to solve time-dependent equations.

A metallic material is characterised by increasing resistivity with temperature, finite (dc) resistivity for T tending to 0 K and Drude-like reflectivity in the infrared spectrum; while in a semiconductor, resistivity decreases with temperature and it diverges at low T [70]. However, the difference between the electrical manifestations is strictly defined only at $T=0K$, where metals have a finite resistivity while insulators own a diverging resistivity. At finite temperature, the distinction is less clear because thermal excitation can always stimulate charge-carrying states and, in practise, it is a matter of comparing the resistivity values, which differ of many orders of magnitude. For instance, being pure 2D graphene a semimetal, its resistivity at finite T is extremely close to the one of highly doped inorganic semiconductors.

In a crystalline (ordered) medium, organic or not, the periodic potential generated by the crystal atoms influences the energy levels distribution and, so, the transport of charge carriers. The overall effect is the formation of energy bands, that are groups of many closely spaced energy levels, separated by forbidden energy regions, *i.e.* band gaps. The bands are a direct consequence of Pauli exclusion principle which forbids two states from having an identical quantum configuration.

The solution of Schrödinger equation with the inclusion of the periodic potential determines Bloch’s eigenstate for the charges, where the wavefunction is factorised in a free-electron term and in a Bloch function, which is a function with the same periodicity

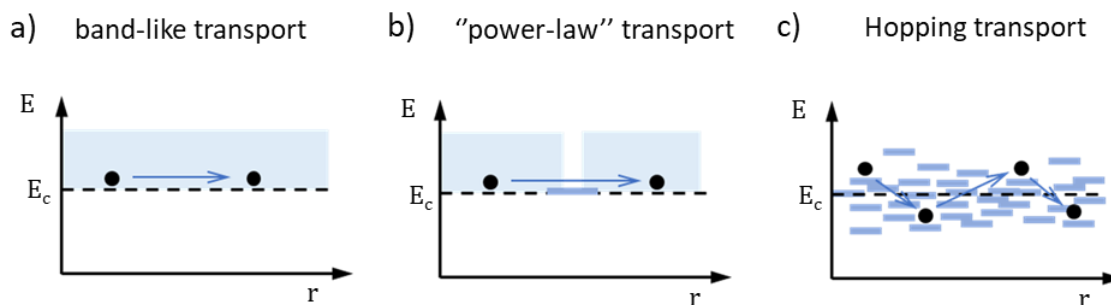


Figure 2-1. Diagrams of energy E versus spatial coordinate r for different transport mechanisms. From left to right, by increasing localisation: (a) band-like transport, (b) critical regime transport or nuclear tunnelling transport, and (c) hopping transport. The dashed line at E_c corresponds to energy edge at which transport occurs, e.g. the bottom of the conduction band. The light blue areas represent de-localised regions, while blue short lines are localised energy levels. Black dots are the charge carriers. The diagrams are shown for negative charge carriers. A similar picture (with reversed energy band) could be drawn for positive carriers, i.e. holes.

of the lattice. An approximated way of considering the periodic potential in the transport is to treat the carrier as free and to include its effect in the value of mass, that it is renamed effective mass.

In naïve term, two main bands are usually considered: a valence band and a higher energies conduction band, separated by a band gap of few eV. Two types of carriers are present in a semiconductor: electrons and holes, that are represented as the absence of electrons. The valence band is filled with electrons, while the conduction band is filled with holes; thermal or optical excitations, as well as presence of doping impurities can change the occupancy distribution between the two bands. The motion of carriers under an external electric field occurs from occupied to unoccupied energy states in the same band.

The discussed band-like transport is schematised in the energy vs. position (E - r) diagram of Figure 2-1a.

Hopping – Thermal Activated Transport

In systems with a certain degree of disorder – structural or energetic – the CT is modified from the common band-like motion occurring in organic crystals. The disorder induces a broadening of the DoS and charge carriers become localized over few atoms/molecules. The size of these regions is quantified in average by the double of localization length ξ ,

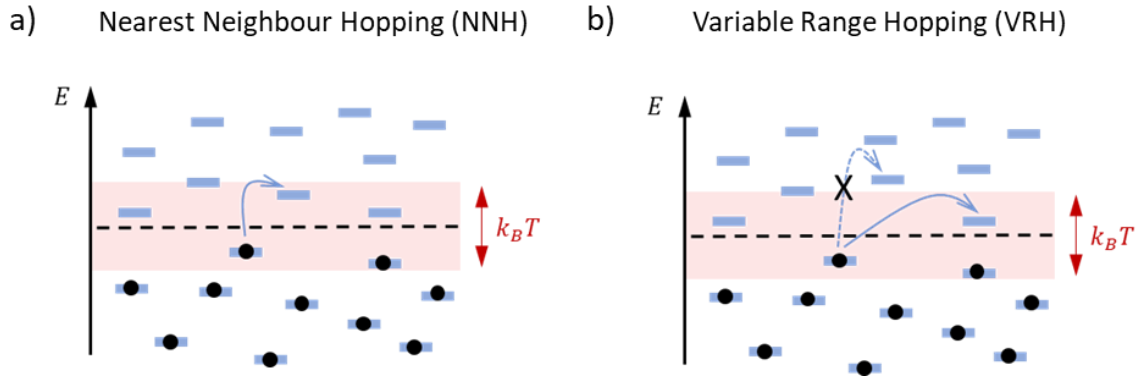


Figure 2-2. Schematic illustration of two hopping transport models: (a) the Nearest Neighbour Hopping (NNH) transport, or Arrhenius-like transport, and (b) the variable range hopping (VRH) transport. The energy E is along the y -axis. Energy levels are depicted as short light blue dashes. If they are occupied by a carrier, a dark dot is present; otherwise, the states are unoccupied. In the VRH, charges around the Fermi energy E_F can move to further unoccupied levels in the spatial landscape, without the need to overcome the thermal energy $k_B T$.

that is defined as the average spatial extension of the charge carrier wave function. Under a low electric field, the motion of a carrier from a localised region to another, located at a distance x_{ij} and unoccupied, is only possible by (stochastic) quantum tunnelling through a forbidden/insulating region. The process is mediated by the lattice vibrations, *i.e.* the phonons, and occurs in an energy range close to Fermi surface E_F . It is said that the carrier “hops” between the two regions and the associated transport mechanism is referred as hopping. The probability of these “hops” (upward in energy) at temperature T is given by [71]

$$\Gamma(x_{ij}) \sim \exp \left\{ -\frac{x_{ij}}{\xi} - \frac{E_{sc}(x_{ij}) + q\varphi(x_{ij})}{k_B T} \right\} \quad (2-1)$$

and the resistivity is inversely proportional to this probability. E_{sc} is the scattering energy with impurities/trap states, $\varphi(x)$ is the Coulomb potential generated by the charge carrier system, q is the charge of the carrier, and k_B is the Boltzmann constant. The sum of E_{sc} and $q\varphi$ resembles an activation energy. The main contribution to conduction is then given by maximising the exponent of eqn. 2-1.

The most common kind of hopping transport is nearest-neighbour hopping (NNH) or thermal activated transport, given the important role of the thermal energy contribution

in the process. In NNH, only the closest energy levels to the carrier must be considered as possible transport path. This imposes a limit for x_{ij} in eqn. 2-1 and NNH is pictured with the following exponential dependence of resistivity

$$\rho_{NNH}(T) = \rho_{0,NNH} \cdot \exp\left\{-\frac{E_a}{k_B T}\right\} \quad (2-2)$$

The activation energy E_a is the (barrier) energy carriers must overcome to contribute to the transport and it includes all the information about the system. The functional form of eqn. 2-2 is often referred as Arrhenius-like, in analogy with the relation for the rate constant of a chemical reaction.

Variable-Range Hopping (VRH)

At low temperatures, where lattice vibrations have a minor role, a different kind of hopping takes place. This model is referred as Variable-Range Hopping (VRH). Conversely to NNH, both the distance and the energy that the carrier must overcome are taken into account. A longer “hop” of the carrier/higher distance could be favoured if the activation energy is lower than the one needed to move in a closer region/site. An energy scheme of the VRH mechanism compared to NNH one is shown in Figure 2-1 to clarify the picture. The usual resistivity functional form for the VRH transport is expressed by a stretched exponential

$$\rho_{VRH}(T) = \rho_{0,VRH} \cdot \exp\left\{\left(\frac{T_0}{T}\right)^p\right\}. \quad (2-3)$$

The exponent p characterizes the type of the VRH model and it could depend on system dimensionality d . In Mott-VRH [72], p is equal to $1/(1 + d)$; while for Efros-Shklovskii (ES)-VRH [73], it assumes the value of $1/2$ independently on d . The latter case is discriminated by considering coulombic interactions between charge carriers. These interactions modify the energy states and cause the formation of a forbidden gap in the density of energy states around E_F .

T_0 is instead a characteristic temperature that is correlated with ξ : the lower the T_0 , the larger the latter. T_0 assumes a different form for each model and it could depend on the system dimensionality d , as well as the system dielectric constant ϵ and the density of states (DoS) around the Fermi energy g_0 . It is respectively

$$T_{0,M} = \frac{c(d)}{k_b \cdot g_0 \cdot \xi^d} \quad (2-4)$$

for Mott-VRH, and

$$T_{0,ES} = \frac{2.8q^2}{4\pi\epsilon_0\epsilon k_b \cdot \xi} \quad (2-5)$$

for ES-VRH. $c(d)$ is a constant reported in the appendix, while ϵ_0 is the vacuum dielectric permittivity. The derivation of eqn. 2-3 using eqn. 2-1 is also presented in appendix.

We notice that, for $p=1$, the Arrhenius functional form of eqn. 2 3 is resumed with $T_0 = -E_a/k_B$.

Critical regime

We have seen that “disorder” changes the electric potential felt by carriers, causing their localization and disrupting the transport. Ideally, we can consider a metallic system, with delocalised carriers, and progressively induce disorder. At a certain moment, the system will start to lose the metallic character and will transit to a regime where transport is dominated by hopping. The change is defined in literature as metal-to-insulator transition (MIT) [74]. Looking in terms of (decreasing) variation of energy, instead of system disorder, states change from being extended to being localised. The energy E_C at which such change occurs is named mobility edge. If Fermi energy is lower than the mobility edge, it will lie in a region of localised states and zero temperature resistivity will tend to infinite. In the opposite case, the system is metallic with a finite resistivity at $T=0K$. States deep in the band tails have a high probability to become localised because they relate to orbitals that feel huge potential fluctuations, while states in the centre of the band will probably remain de-localised.

The just discussed picture neglects carrier-carrier interactions. If this term is included in a perturbative way, the MIT transition could occur even in system with extremely weak disorder [75].

Thus, a system in proximity of the MIT transition is in a critical state and the “critical” resistivity happens to be described by the following temperature power-law [76]

$$\rho_{PL}(T) = \rho_{0,PL} \cdot \left(\frac{T_1}{T}\right)^m, \quad (2-6)$$

where T_1 and m are parameters which describe the transport mechanism and $\rho_{0,PL}$ is a pre-factor, independent on T .

Nuclear Tunnelling (NT)

In low-defects, organic semiconducting systems, the CT was connected to a universal scaling curve having the same temperature power-law behaviour of eqn. 2-6 [77,78]. For low applied voltages V , the measured current is expressed as

$$I(T) = I_0 \cdot T^m \cdot u(V, T, m, n_{hop}) \cdot V \quad , \quad (2-7)$$

where I_0 is a factor independent on temperature T ; and u is a complex function that contains a gamma function among the terms. n_{hop} is the number of carrier transport events, referred as “hops” in analogy with hopping models.

In present physical framework, CT along the polymeric backbone is driven by the coupling to the nuclear vibrations (*i.e.* a phonon bath). Carriers tunnel through the potential formed by the coupling of the electronic charge to its nuclear environment, as described by quantum nuclear tunnelling (NT) theory. This scaling behaviour was observed both in networks of 1D polymeric nanofibers [77,79] and in conjugated polymeric films, such as PBBT-C16 [80] and PEDOT:PSS [78]. The coupling is quantified by the Kondo parameter, defined as $\alpha_K = m/2 + 1$ [81]. A higher value of α_K indicates a stronger charge-environment coupling. Typical values reported in literature for π -conjugated polymers were bath phonon energies of ≈ 100 meV [82] and m within the range 1.25 – 6.75 [81], corresponding to α_K values between 1.6 – 4.4. Asadi *et al* [81] argued also that because the coupling strength is related to the tunnelling events, m should be proportional in some way to n_{hop} .

2.2 Reduced Activation Energy Method - $W(T)$

We have seen that there are two recurring functional dependences frequently used and combined to describe the measured $\rho(T)$ trends in disordered systems: (i) a stretched exponential and (ii) a power law.

From the experimental and data analysis point-of-view, a critical issue in interpreting such behaviours is inherent of the used fitting method. In many literatures works, data analyses

are based on simple fits of $\rho(T)$. Considering the VRH model, for instance, the logarithm of ρ is fitted as a function of T^{-p} , with p chosen a priori. This *ad hoc* linearising procedure of $\rho(T)$ could then lead to systematic errors and have proven ambiguous. Biased results may indeed occur in fitting Poisson-distributed data sets, such many electrical points averaged in a small range of temperature, by least-square minimisation methods [83].

As first introduced by Zabrodsky and co-workers [84], a robust and self-consistent mathematical method to avoid possible artefacts in $\rho(T)$ analysis is computing its logarithmic derivative, also called activation energy. This quantity normalised by thermal bath energy $k_B T$ (k_B is the Boltzmann constant) is named reduced activation energy and it is expressed as

$$W(T) = - \frac{\partial \ln \rho}{\partial \ln T}, \quad (2-8)$$

While widely applied in the study of the CT in inorganic semiconductors, the $W(T)$ method is seldom exploited for graphene-related materials

From the physical point of view, the activation energy represents the amount of energy a carrier should possess to transport in energy space between two states. However, this semi-classical definition of W is not suitable to describe all situations that can be encountered. Here, W will be mainly considered as an analysis tool. $W(T)$ method transforms stretched exponentials and PL curves into linear functions in log-log space, clearly simplifying the issues related to the fitting procedures. The method is convenient provided that only one transport mechanism is involved per time in a specific temperature range. Although the assumption above is quite rigid, it usually occurs that a mechanism among the others has the main role in the transport outcome. The analysis procedure could then be carried out and its results contain the essence of the transport behaviour. Conversely to a simple $\rho(T)$ fit, different transport regimes are clearly revealed in $W(T)$ plots, as shown in the scheme of Figure 2-3.

For the stretched exponential of eqn. 2-3, the activation energy becomes

$$W_{VRH}(T) = p \cdot \left(\frac{T_0}{T}\right)^p \quad (2-9)$$

and its logarithm is a straight line as a function of $\ln T$.

$$\ln W_{VRH} = -p \cdot \ln T + \delta \quad (2-10)$$

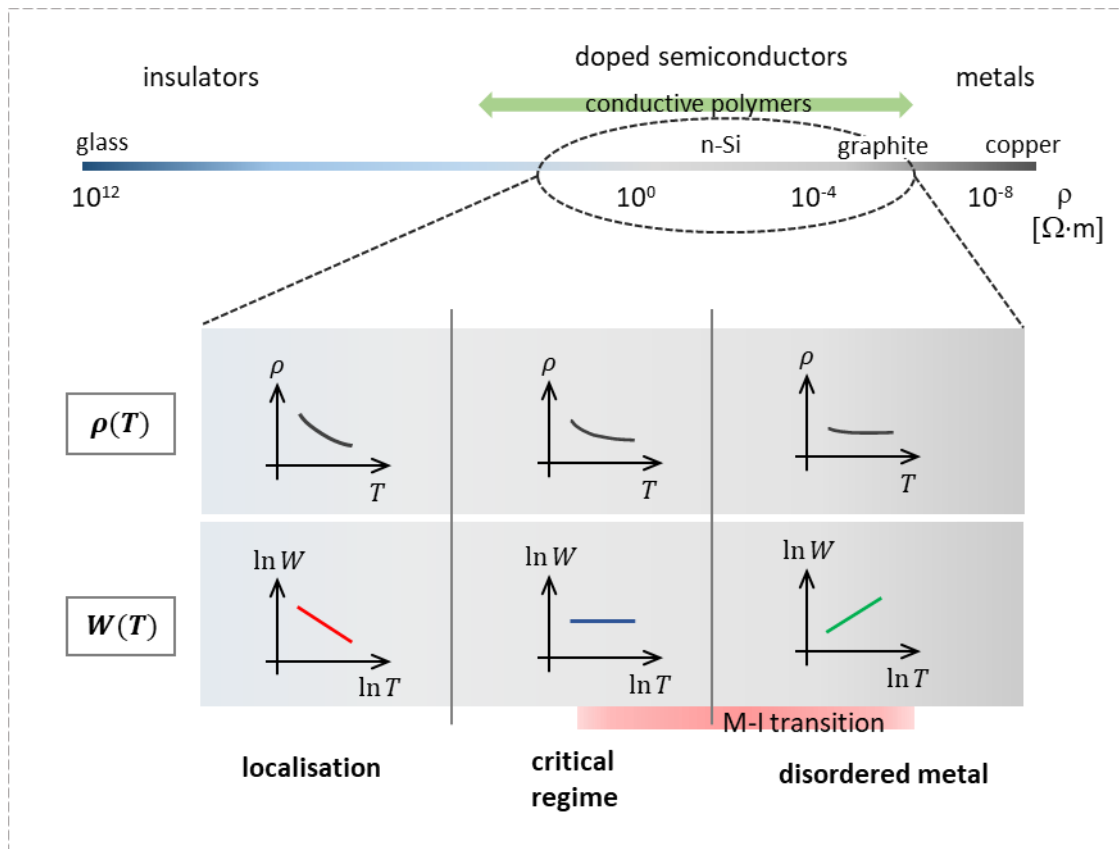


Figure 2-3. Scheme representing different materials ordered by their electrical resistivity. Simplified $\rho(T)$ and $W(T)$ plots are also presented for different charge transport regimes. While $\rho(T)$ does not always allow an unambiguous distinction of CT regimes, the fit of $\ln W - \ln T$ does. A system with localised charges has a negative $\ln W - \ln T$ slope, while metallic transport is identified by a positive $\ln W - \ln T$ slope. In a critical regime, W is independent on T .

where $\delta = \ln(p \cdot T_0^p)$.

Because $p > 0$ for the VRH models, we underline the slope is negative in $\ln W(\ln T)$. By linearly fitting eqn. 2-10, p and T_0 are immediately obtained.

In the case of power law of eqn. 2-6, instead, the activation energy is constant and equal to the positive exponent m .

$$W_{PL} = m \quad (2-11)$$

Hence, the logarithm of eqn. 2-11 is also constant:

$$\ln W_{PL} = \ln m \quad (2-12)$$

Differently from the VRH, the $W(T)$ method permits the evaluation of only m , and not of T_1 characteristic temperature. Therefore, T_1 could not be directly decoupled from the pre-factor $\rho_{0,PL}$.

We must cite that a metallic behaviour in the system manifests as an increase of activation energy with W . However, multiple transport mechanisms often superimpose in disorder metallic systems and a simple positive line in $\ln W(\ln T)$ is hardly observed [85].

In Fig. 2-3, we summarise the three $\rho(T)$ situations discussed and corresponding $W(T)$ plots.

2.3 GO/RGO CT Studies Reported in Literature

In past 15 years, the study of charge transport in modified graphene and in reduce graphene oxide has been a quite active field of research. However, few works carried out a detailed analysis of different transport mechanisms and most of them were performed on ad-hoc devices in the micrometre scale, that are often quite different from reality [86]. Charge transport in mechanically cleaved, crystalline graphene is expressed by an increasing resistivity with temperature and by a temperature-independent carrier density [87], following its semi-metallic nature as determined from electronic band structure.

First studies of CT in defective graphene systems were made using ion and plasma irradiated graphene [88], polycrystalline CVD [89] graphene and on hydrogenated graphene [90].

In these partially defective, 2D aromatic carbon structures, the situation is not anymore metal-like: charges move at low temperatures following a VRH model. Defects suppress the delocalization of charges, typical of semimetal graphene, and resistivity goes toward insulating values.

Looking to the problem from another perspective, researchers tried to investigate a material comprising already defects, instead of inducing them. In this regard, graphene oxide is the perfect toy model material: easily processable from one side and with tunable defectivity by reduction from the other side.

Reduced GO (RGO) is pictured as a random subnetwork of sp^2 hybridised carbon regions surrounded by large insulating areas, such as sp^3 carbon bonded with oxygen and holes [34]

Gomez-Navarro *et al* [91] studied the transport in a chemically reduced GO monolayer. They claimed 2D Mott-VRH as a plausible CT mechanism at low T . Their results were interesting for the time, when the structure of RGO was still poorly explained. On the other hand, the data analysis was oversimplified and they did not address sheets with different chemical structures, *i.e.* different C sp^2 content.

Two years later, Kaiser *et al* [56] confirmed the transport results studying similar RGO single sheet transistors. Their focus was on the effect of electrical field to aid the transport by electrical field driven tunnelling, mechanism that claimed it acts in parallel with hopping. They correlated the observed transport phenomenology of the device to the hypothesised, inhomogeneous chemical structure of the RGO sheet, and made a comparison with what occurs in conducting polymers.

In the same year, Eda *et al* [54] discussed RGO CT as a function of reduction degree. In their framework, GO undergoes a transition from insulator to semiconductor as the oxygen functionalities are removed from the sheet. The transport is of 2D-VRH type at low temperature and becomes thermal activated going toward room temperatures. Nevertheless, the analysis of $\rho(T)$ was still incomplete and not self-consistent.

A more comprehensive study about single layer RGO was published few years later Joung *et al* [55], who self-determined the CT regime in the material. In this paper, they took advantage of the activation energy method, which has been described in previous Section. Their conclusion is that transport in single RGO sheets is purely 2D and charges hop from one aromatic domain to the next one following ES-VRH scheme. The localization length ξ corresponds approximately to half of the size of aromatic domains in the RGO sheet.

We notice that while both negative (n-type) and positive (p-type) charges motion have been shown in *ad hoc* doped RGO transistors, in vacuum or with a suitable capping [92], the transport has a main p-type character in RGO films at ambient conditions. The suppression of n-type transport is generally explained by the presence of moisture, oxygen, and/or defects introduced during device fabrication [93].

By combining tens of thousands of RGO sheets in a film, the complexity of the structure increases. Investigation of CT mechanisms in RGO films has been carried only in recent years [58,63,64,94] and most of the results are controversial and/or do not benefit of broad consensus. The main question, hard to address, is the kind of hopping occurring at low temperatures, from which it descends the insulating/semiconducting nature of the system. Both Mott VRH and ES-VRH were claimed (and mutually excluded) in crisscrossing temperature ranges.

A first work using RGO thin films is the one of Muchharla *et al* [61]. They obtained a 2D-VRH from the data analysis in a mid T range, in contrast to what was shown for single sheets. Unfortunately, they did not perform measurements at lower T .

Two main approaches are followed to analyse experimental quantities relevant for charge transport, such as resistivity or mobility: a “qualitative” approach based on pre-determined transport models; or the combination of different transport functional forms, which superimpose in the motion of charges.

The work of Vianelli *et al* [65] claims a thermally activated transport at room temperature and a 2D Mott-VRH transport decreasing the temperature, even for ultra-reduced samples.

Kim *et al* [63], instead, proposes a model where two pathways superimpose for the motion of charges: a 3D VRH of charge occurs in highly chemically disordered regions, while quantum tunnelling and thermal activation occur in low disordered and sp^2 crystalline regions. In their opinion, the VRH is entirely frozen-out for highly reduced GO. Recent results of Faucett *et al* [58], Silverstein *et al* [95] and Kurnosov *et al* [96] show a clearer picture of transport in RGO films. A ES-VRH is obtained a low T by exploiting the same analysis scheme of reference [55]. However, these works still do not address the correlation between structural and chemical properties with CT phenomenology. Furthermore, they miss to explain the transport behaviour at larger T (closer to room ones).

The work of Shaina *et al* [97] is the only one that qualitatively discussed higher T transport in a thick RGO film: they observed a power law behaviour and suggested a transition to a “weakly conductive” metal system. Moreover, they highlighted the role of inter-sheet interactions in such behaviour.

In appendix, a summarising Table of relevant articles about CT in RGO systems is presented.

2.4 First Systematic Approach to Study the CT in RGO Thin Films

In this Section we present the extensive work made by Kovtun *et al* [66] to rationalise CT in RGO few-layers and thin film systems. By developing a scale-independent model, their results provide an unambiguous answer to the long-debated CT regimes taking place in such systems.

The work is based on a robust data analysis of the electrical resistivity vs. temperature $\rho(T)$, being a reliable physical observable to achieve in depth insight from single sheet to large-area aggregates. Indeed, carrier mobility is not a useful quantity to compare systems with different geometries and scale-lengths.

The use of RGO enabled them to tune independently *i*) the conductivity of each sheet, *ii*) the lateral size of the sheets, and *iii*) the thickness of the material, *i.e.* the number of sheets stacked over each other, fabricating a total of 28 different RGO devices.

For each device, ρ was measured from *ca.* 10 K to 300 K in order to detect the existence of different transport regimes. In all devices they found that ρ decreases with the increasing of temperature, clearly indicating that all the networks possess a semiconducting behaviour, with room temperature resistivity ρ_{RT} lying in the range between 2 and $2 \cdot 10^{-5} \Omega \cdot m$.

The results are summarised in Figure 2-4 with two representative curves for $\rho(T)$ and for corresponding $W(T)$. In the case of individual RGO sheets the log-log plot of $W(T)$ is linear with a negative slope corresponding to a VRH regime over the entire range of the measured temperatures. Differently, for RGO films, two regimes separated by a transition temperature (T^*) are clearly recognizable: a linear trend with negative slope, similar to that measured in single sheets, for $T < T^*$ and a constant trend corresponding to PL for $T > T^*$. The clear assignment of the CT mechanisms is possible because the presence in all devices of linear trends in $W(T)$ clearly excludes the occurrence of multiple mechanisms. In Figure 2-5a, it is shown that observed T^* increases with ρ_{RT} (the dashed curve is a guide for eyes). Hence, it was possible to infer a single scheme for the CT in RGO networks by comparing the quantitative analysis of the two regimes in all 28 devices. The single sheet

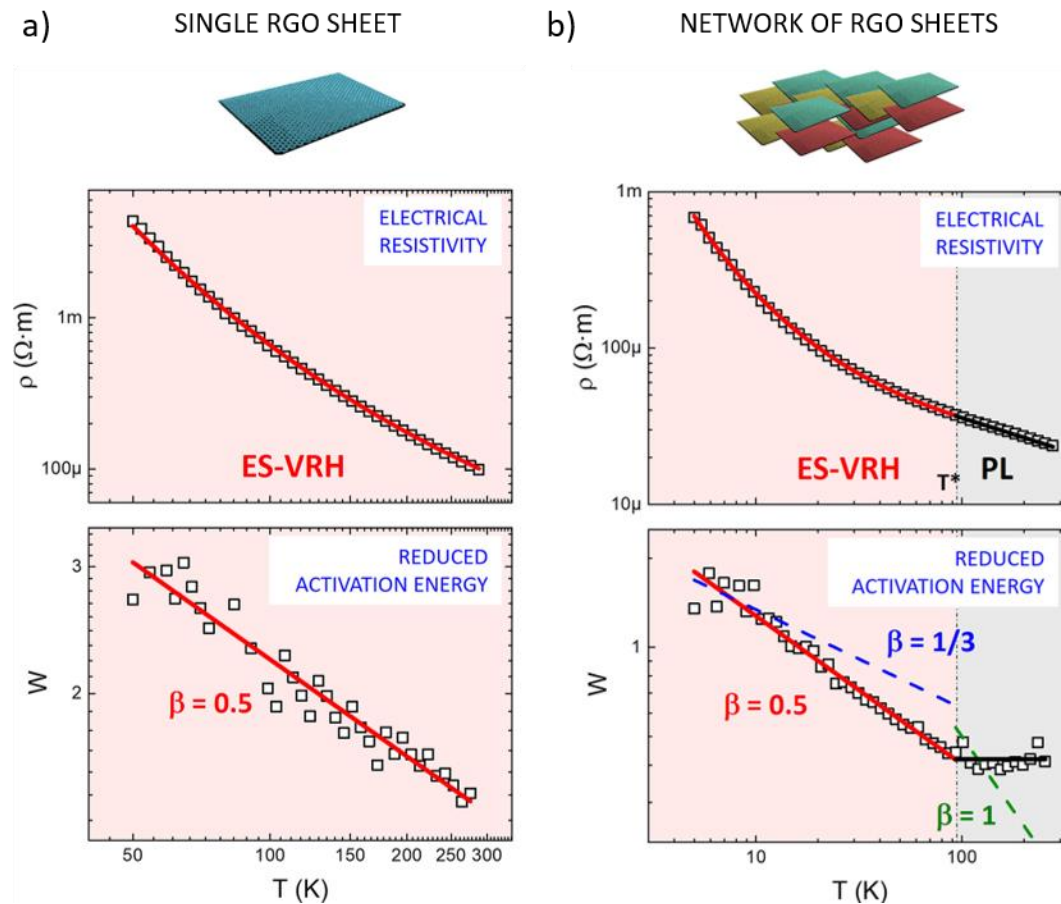


Figure 2-4. Log-log scale plot of resistivity $\rho(T)$ (top) and of corresponding reduced activation energy $W(T)$ (bottom) for (a) a single RGO sheet and (b) a representative RGO network. Conversely to ρ analysis, the use of $W(T)$ allows to unambiguously discriminate different transport regimes. Two transport regimes are obtained in RGO: VRH (red line) and PL (black line).

results a particular case of the RGO networks where the transition temperature T^* is out of the range of measured temperatures ($T^* > 300$ K).

The scheme is supported by the behaviour observed on micro-networks of few partially overlapped nanosheets where T^* is compatible with the room temperature within the experimental error bar (open circles in Fig. 2-5a). This suggests that T^* is related to the structural complexity of the network, for example, to the number of overlapping sheets. Both the VRH and the PL regimes are characterised by three similar parameters: a pre-factor ($\rho_{0,VRH}$ or $\rho_{0,PL}$), a characteristic temperature (T_0 or T_1), and a characteristic exponent (p or m). How this set of parameters (plus T^*) was obtained and their role in the CT in RGO networks is described in the following.

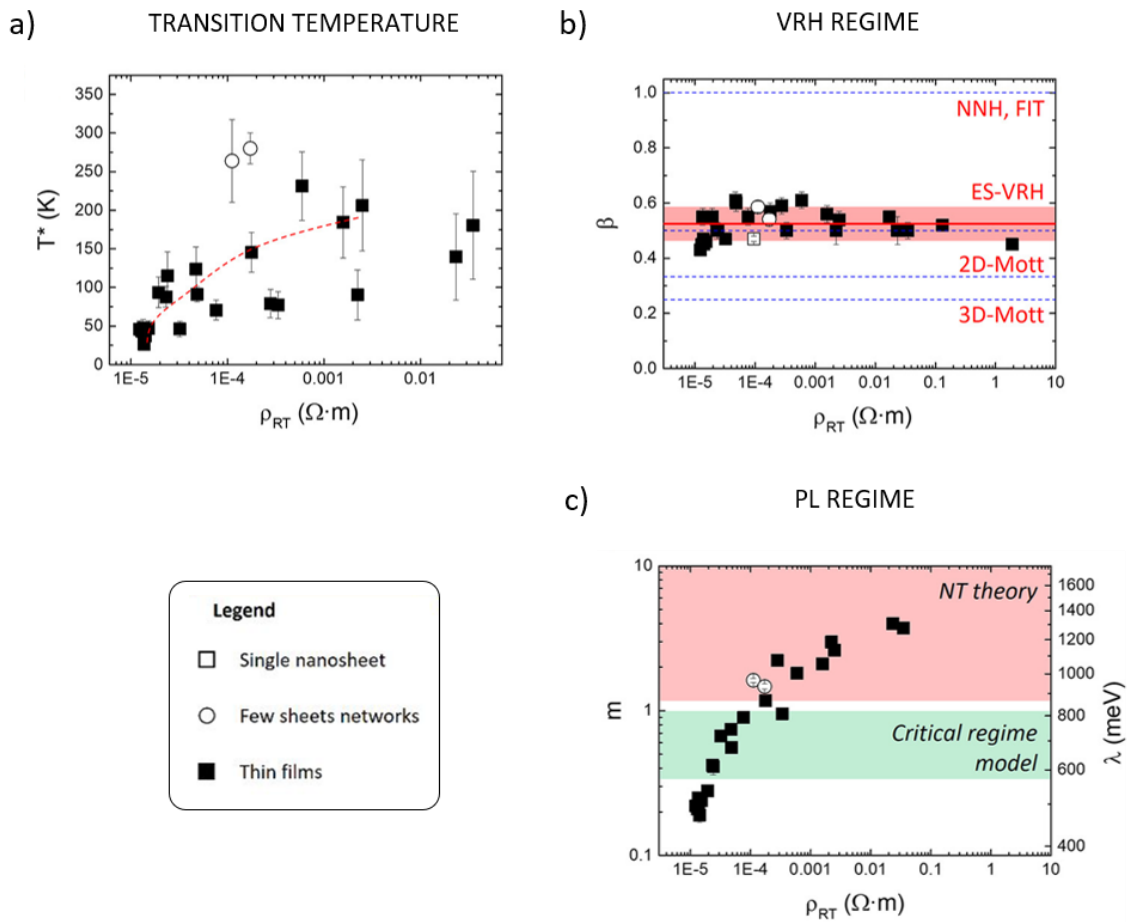


Figure 2-5. Plot of relevant transport parameters as a function of room temperature resistivity ρ_{RT} for all devices studied in ref. [66]. (a) Plot of transition temperature T^* vs ρ_{RT} , with a red dashed line as eye guide. (b) Plot of exponent p values in the VRH regime vs ρ_{RT} . All the obtained values are consistent with $p=1/2$, corresponding to the ES type of the VRH. (c) Plot of power exponent m values in PL regime vs ρ_{RT} . The corresponding reorganization energy λ is also reported on the secondary y-axis.

The data analysis was performed according to/ the same scheme:

- i) the $W(T)$ curves were linearly fitted in the corresponding ranges to calculate p , T_0 and m as free parameters;
- ii) just calculated parameters were hold fixed and the resistivity pre-factors were calculated by fitting the $\rho(T)$ curves;
- iii) both $W(T)$ and $\rho(T)$ were fitted using the parameters previously calculated as initial values, verifying their convergence on successive iterations.

In the VRH, all the obtained p values were always close to $1/2$, as shown in Figure 2-5b. For sake of comparison, the values expected for other regimes are also indicated (dashed blue lines): the VRH in 2D and 3D ($p = 1/3$ and $p = 1/4$, respectively), the NNH ($p = 1$). All such

regimes can be clearly excluded. In addition to ES-VRH, the value $p = 1/2$ can be explained by 1D-Mott VRH, but this last model is apparently insignificant in the case of carbon network structures [98]. From T_0 they computed the localization length ξ , using $\varepsilon_r = 2.5$ and $\varepsilon_r = 3.5$ for single or few-sheets RGO and for RGO thin films, respectively.

While the ES-VRH regime fully describes the measured $\rho(T)$ behavior of single RGO, PL regime is dominant at high temperature (close to RT) when two or more nanosheets are assembled partially in contact with each other. For thick RGO films, $\rho(T)$ is thus described by the PL regime in most of the measured temperature range. Therefore, the observation of the PL regime indicates a fundamental role of the inter-sheet CT in a RGO network. The observed m values ranges between 0.2 and 4.0 increasing with the measured ρ_{RT} of each network (Figure 2-5c). By comparison with values reported in literature for conjugated polymers, the measured m in RGO networks spans between the ranges defined by MIT transition and the one measured using NT models. Such experimental evidence highlights the analogy between PL transport in RGO networks and conjugated polymers thin films.

Correlation between ES-VRH and PL regimes

This Section is dedicated to elucidating the CT mechanism occurring in the PL regime. and to understanding if the ES-VRH and PL regimes were correlated.

To gather information about the PL regime it is convenient re-writing eqn. 2-6 by collecting $\rho_{0,PL}$ and T_1 in a scale factor $B = \rho_{0,PL} \cdot T_1^m$. Then, the logarithm of B corresponds to

$$\ln B = \ln \rho_{0,PL} + m \cdot \ln T_1 \quad (2-13)$$

Eqn. 2-13 represents a mathematical equivalence between the PL parameters of each individual i -th RGO network. m and $\ln B$ are directly calculated by $W(T)$ and $\rho(T)$ analysis, respectively, for each sample. All equivalences in the set are indeed independent from each other. Moreover, we can notice how the solution of eqn. 2-13 given by a linear combination of $\ln T_1$ and $\ln \rho_{0,PL}$.

The correlation plot $\ln B$ vs. m is shown in Figure 2-6a for all 28 devices. Because data are not randomly scattered but lay on a straight line (red line), the PL parameters are correlated. Such experimental evidence permitted i) to decouple the characteristic temperature T_1 and the prefactor $\rho_{0,PL}$ and ii) to prove that such parameters are the same

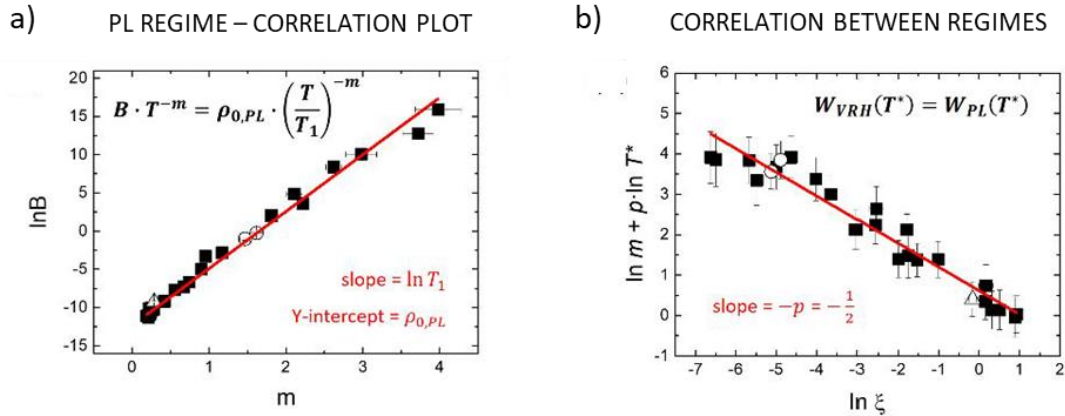


Figure 2-6. (a) Correlation plot of PL regime: $\ln B$ vs m , obtained from eqn. 2-13, for all 28 RGO devices. The good linear fit (red curve) suggests a single transport mechanism common of all RGO networks. (b) Correlation plot between the PL and VRH regimes obtained by requesting the continuity of $W(T)$ at T^* . In all graphs, symbols correspond to different type of devices: (■) thin films, (○) few sheets partially overlapped and (△) single high-reduced RGO sheet.

for all the devices, corresponding to the constant slope ($\ln T_1$) and the y-intercept ($\ln \rho_{0,PL}$), as calculated by a linear fit according to eqn. 2-13. The second observation indicates that the same CT mechanism occurs in all the RGO networks.

The obtained values for all devices are $k_B T_1 = 148 \pm 5$ meV and $\rho_{0,PL} = (4.4 \pm 0.1) \cdot 10^{-6} \Omega \cdot m$. It is possible to note that the power exponent m is the only parameter that independently identifies each RGO device. Recalling the analogy of RGO networks with conjugated polymers, similar approaches can be employed to study CT. Hence, as in polymeric materials, the parameter m is described in terms of reorganization energy (λ) of a phonon bath upon electron transfer [99], where the phonon bath energy is $k_B T_1$ in RGO networks. The reorganization energy term describes the strength of the electron-phonon bath and can be reliably estimated as twice the relaxation energy of a polaron localized over the region of two overlapped RGO sheets, *i.e.* the twice the polaron binding energy: $\lambda = \left(\frac{m}{2} + 1\right) \cdot k_B T_1$ [82,100].

The comparison of parameters calculated in the two CT regimes, at low and at high T (ES-VRH and PL), provides the following observation:

- i) the PL exponent m (or the correlated reorganization energy λ) decreases with the increase of the localization length calculated in ES-VRH; and

- ii) the measured $\rho(T)$ data and the corresponding $W(T)$ analysis do not show discontinuities at the transition temperature T^* between ES-VRH and PL regimes.

Again, a strong analogy with polymeric semiconductors, where the reorganization energy decreases as the size of the π -conjugated system is increased [101], is highlighted by i). The second experimental result, instead, implies that the resistivity calculated in the VRH regime corresponds to that in PL one at the transition temperature T^* : $\rho_{VRH}(T^*) = \rho_{PL}(T^*)$. From this, also $W_{VRH}(T^*) = W_{PL}(T^*)$ follows. Inserting the respective equations in the last equivalence, it is possible to derive a general formula comparing the parameters of the two CT regimes: T^* , p , m and ξ , obtained by fitting $W(T)$ (eqn. 2-10 and eqn. 2-12) for each i -th RGO network. Calculating all the terms as sum of logarithms they obtained:

$$p \cdot \ln T^* + \ln m = -p \cdot \ln \xi + K \quad (2-14)$$

where $K = p \cdot \ln \gamma + \ln p$ and $\gamma = \xi \cdot T_0$, which is a constant. In analogy with the correlation procedure employed for PL (eqn. 2-13 and Figure 2-6a), a set of independent equations should be considered, one for each measured i -th RGO network.

Figure 2-6b shows the correlation plot $\ln \xi$ vs. $(p \cdot \ln T^* + \ln m)$ where each point corresponds to the data of each RGO network. The red line corresponds to a linear fit following eqn. 2-13. The observed slope is equal to 0.55 ± 0.03 and it is in good agreement with the ES-VRH model. The achieved linearity supports a strong correlation between ES-VRH and PL, even if the two regimes are based on different mechanisms and act at different temperature ranges.

Dependence of ξ on the structural and geometrical properties of the RGO nanosheets network.

Differently to single RGO sheet, both in-plane and out-of-plane components can contribute to the transport when two or more sheets are overlapped (even partially). The case in which two adjacent sheets (*i.e.* belonging to the same plane) only touch the edges is statistically negligible. The sheet-to-sheet transport is thus mainly out-of-plane, while the in-plane component is related to the single sheet.

Experimentally, these two components were investigated by tuning independently different parameters which define the RGO networks: the oxidation degree (*i.e.* the corresponding intrinsic conductivity), the lateral size of the sheets composing the

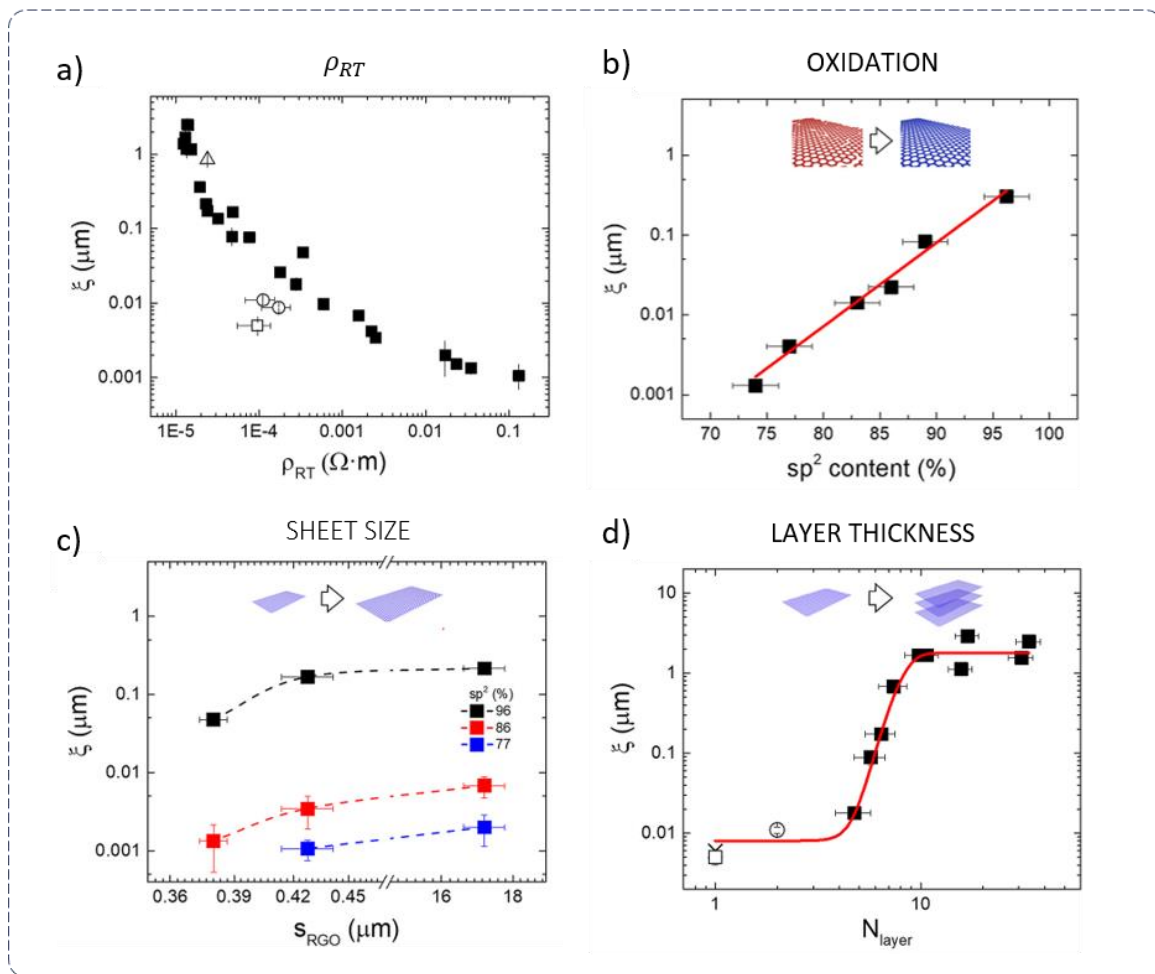
DEPENDENCE OF ξ ON

Figure 2-7. Dependence of localization length ξ on: (a) room temperature resistivity ρ_{RT} ; (b) C sp^2 content in the RGO sheets; (c) average sheets size s_{RGO} of RGO used to fabricate the films; and (d) film thickness, quantified by the number of stacked layers N_{layer} . In (a) and (b), symbols correspond to different type of devices: (■) thin films, (○) few sheets partially overlapped and (□) single high-reduced RGO sheet.

network, and the thickness of the thin film (*i.e.* the number of stacked sheets layers N_{layer}). A first general observation is that ξ increases with the decrease of the room temperature resistivity (Figure 2-7a).

The intrinsic conductivity of each sheet composing the network was varied by changing the content of the sp^2 carbons on RGO basal plane through thermal annealing. In this case, the average film thickness and the average lateral size of the single RGO sheets were both kept constants and equal to $N_{\text{layer}} = 8 \pm 1$ and $\langle s_{RGO} \rangle = (428 \pm 14)$ nm, respectively.

ξ vs. sp^2 is shown in Figure 2-7b and can be summarised as follows: for low sp^2 content ($\lesssim 80\%$), it results $1.3 < \xi < 5$ nm, in agreement with the values typically observed in a single RGO sheet [17,102]. For higher aromatic contents ($\gtrsim 80\%$) the parameter ξ reaches a size up to 300 ± 20 nm evidencing that charges can be delocalized over the single aromatic region on the RGO sheet. Such result is peculiar to the macroscopic network because in the case of an assembly of a few sheets partially in contact, the measured ξ amounts to a few nm, despite the sp^2 content is about 96%.

Then, the influence of the RGO sheets lateral size on CT was studied. Three different average lateral sizes were tested: $\langle s_1 \rangle = (17.2 \pm 0.6)$ μm , $\langle s_2 \rangle = (428 \pm 14)$ nm and $\langle s_3 \rangle = (380 \pm 7)$ nm. For each size, three thin films with different sp^2 contents: 77% (■), 86% (■) and 96% (■) were fabricated. The result for the 9 different size-conductivity combinations are provided in Figure 2-7c. The localization length was found to increase significantly with the aromatic content and to a lesser extent, with the nanosheet lateral size.

The experimental observations can be accounted by assuming that charges travelling along the sheet (in-plane) prefer to circumvent a defect, jumping on different planes (out-of-plane). Therefore, the electronic states can span through different overlapping sp^2 domains belonging to different sheets; charges are delocalized over different RGO sheets, which contribute to CT as a single conductive domain with characteristic size ξ . A cartoon of the two situations (single sheet and multi-layer films) is depicted in Figure 2-8a.

To probe out-of-plane mechanisms, RGO devices with an increasing number of stacked layers (*i.e.* thickness), from isolated single RGO sheets to macroscopic stacks, were prepared. The max number of stacked layers was of 34 ± 2 . As visible in Figure 2-7d, ξ increases sharply at $N_{\text{layer}} \approx 5$, then reaching an almost constant value ranging between 2-3 μm for $N_{\text{layer}} \approx 8$.

Concerning the dependence of room temperature resistivity (ρ_{RT}) on N_{layer} , as expected, it was measured an opposite trend with respect to that observed on ξ in the case of RGO thin films. An analogy can be made with what is observed in thin metal films (< 100 nm) where the electrical resistivity become larger as the film thickness decreases in size. In such systems the change occurs because the mean free path of charge carriers is reduced due to increased scattering effects. The inter-sheet CT (out-of-plane) is favoured respect to intra-sheet CT (in-plane), in agreement with the observation of coherent

“commensurate” electronic states at the interface between sp^2 regions [103]. In general, all the layered graphitic materials have similar electrical properties along the out-of-plane direction; for example “Kish” graphite, high oriented pyrolytic and natural graphites usually show metallic- or semi-metallic-like behaviour [104].

RGO networks as a “composite material”

To summarise, the CT of RGO networks is governed by π -conjugated regions of characteristic length ξ given by the overlapping sp^2 domains. Thus, the longer the π -conjugated domains due to increased amount of aromatic content or the number of RGO layers, the greater the localization length and, in turns, the lower are both the parameter m and the corresponding reorganization energy λ , as observed in semiconducting π -conjugated systems.

A purely geometrical analogy with “composite materials” can be made to describe the role of ξ and its behaviour with the number of layers in RGO networks. The model was envisioned for fibril-form (quasi-1D) conducting polymers [105] and we will refer to it as CT in a *spaghetti-like* network. Its main idea is schematised in Figure 2-8b: π -conjugated regions (*i.e.* both overlapping sp^2 domains in red and isolated ones in yellow) represent conductive fillers activated by an external electrical field \mathcal{E} , while structural holes, defects and sp^3 insulating regions behave like an insulating matrix (green area). In the same panel (Fig. 2-8b), an example is drawn for three-layer RGO film with randomly distributed sp^2 domains (disks) on each layer. Charges motion occurs through the stack (out-of-plane) and it is negligible in the layer plane. Fillers obtained by the overlapping stacked disks are visualized by collapsing all the layers on the projected plane (red regions in bottom surface).

The same concept is reinforced in Figure 2-8c where “disks become segments” (*i.e.* lateral view visualization): the filler (red line) in a RGO multilayer is given by a random path with blobs and dead ends spanning in three dimensions and an overall length equal to the localization length ξ . Using a classical physics approach, this random-paths network corresponds to the superimposition of all the possible trajectories of the charge carrier that travels between the planes “hopping” from one aromatic domain to another.

Since the localization length becomes orders of magnitude larger than the average size of a sp^2 region in a RGO single sheet, sp^2 domain size can be neglected in RGO networks and

SCHEMES

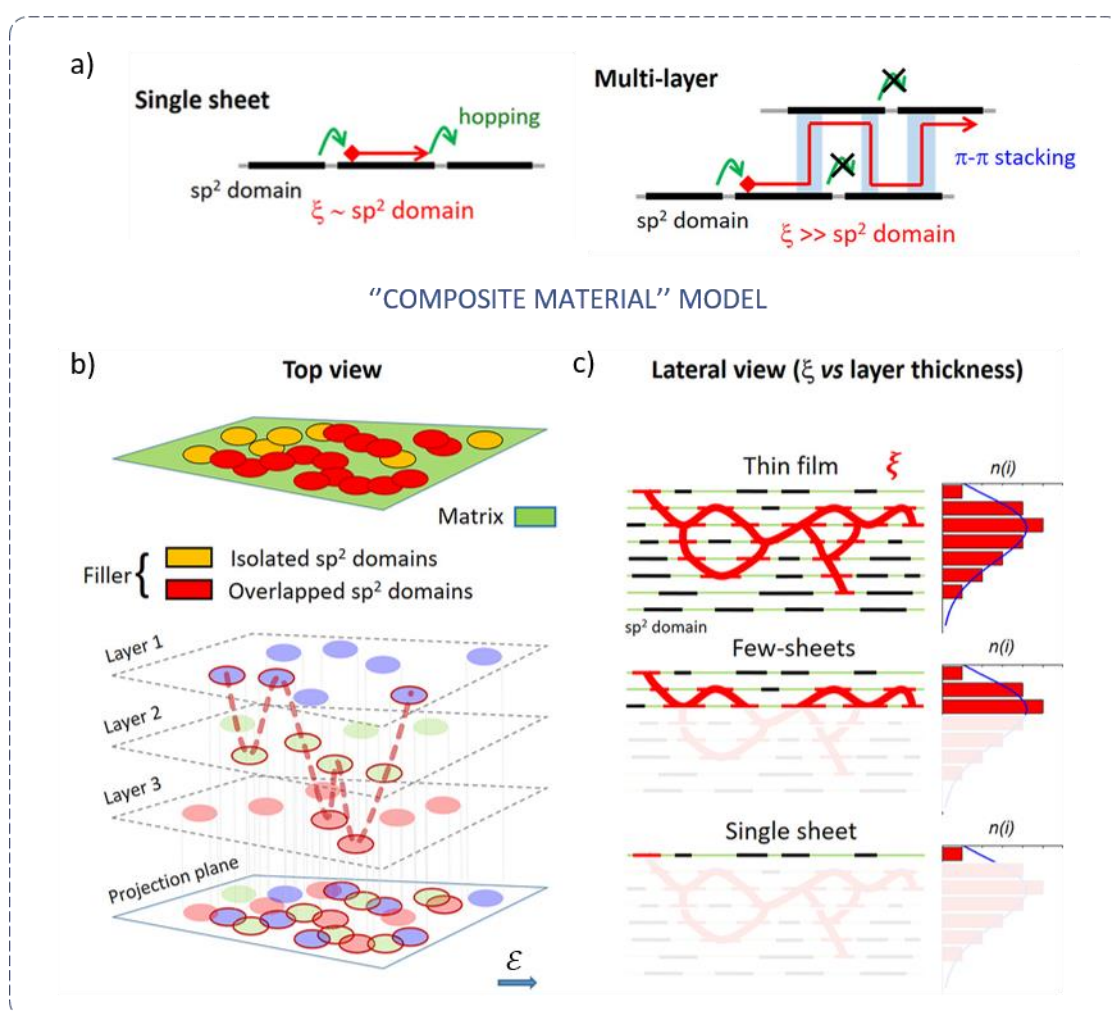


Figure 2-8. Schemes depicting the charge transport in single RGO sheet and in RGO networks. (a) Comparison between the two cases: purely 2D CT in single RGO sheet (left) and 3D transport in stacked RGO sheets (right). In this latter case, the out-of-plane motion due to π - π stacking allows charges to overcome defects. (b,c) Description of CT in RGO networks as they were composite materials with conductive fillers. Cartoons for this geometrical model from (b) top view and (c) lateral view. In (b), the aromatic sp^2 domains are represented by coloured disks. Conduction occurs via overlapped disks belonging to different planes. The same scheme is shown in (c) from lateral view, with disks that becomes short black lines. The red curved lines represent, instead, all the possible geometrical paths of average size ξ a charge can follow. By reducing the film thickness, also the number of paths is decreased.

only the distance between two overlapping aromatic regions – *i.e.* the layer-layer distance. d – plays a role in the transport. Up to a constant (*i.e.* the average sp^2 size), ξ is then proportional to the sum of the steps (*i.e.* the number of conductive sp^2 regions involved in the conduction path) in each layer.

Given a random path in a (3D) thick film, if layers decrease, also the number of steps is reduced. Below to a critical thickness of the film (in RGO case, $N_{layer} \approx 8$) the continuous percolated random path breaks in small, connected regions, causing an abrupt decrease of ξ . The extreme case corresponds to a single sheet ($N_{layer} = 1$), where no sp^2 regions are overlapped and ξ roughly equals to the typical sp^2 domain size in RGO (<10 nm).

2.5 References

- [17] Erickson, K., *et al.*, *Determination of the Local Chemical Structure of Graphene Oxide and Reduced Graphene Oxide*. *Advanced Materials* **22**, 40, p. 4467-4472 (2010). www.doi.org/10.1002/adma.201000732
- [34] Mattevi, C., *et al.*, *Evolution of Electrical, Chemical, and Structural Properties of Transparent and Conducting Chemically Derived Graphene Thin Films*. *Advanced Functional Materials* **19**, 16, p. 2577-2583 (2009). www.doi.org/10.1002/adfm.200900166
- [54] Eda, G., *et al.*, *Insulator to Semimetal Transition in Graphene Oxide*. *The Journal of Physical Chemistry C* **113**, 35, p. 15768-15771 (2009). www.doi.org/10.1021/jp9051402
- [55] Joung, D., *et al.*, *Efros-Shklovskii variable-range hopping in reduced graphene oxide sheets of varying carbon $\$s\{p\}^{\wedge}\{2\}\$$ fraction*. *Physical Review B* **86**, 23, p. 235423 (2012). www.doi.org/10.1103/PhysRevB.86.235423
- [56] Kaiser, A.B., *et al.*, *Electrical Conduction Mechanism in Chemically Derived Graphene Monolayers*. *Nano Letters* **9**, 5, p. 1787-1792 (2009). www.doi.org/10.1021/nl803698b
- [57] Park, M., *et al.*, *Electrical and thermoelectric transport by variable range hopping in reduced graphene oxide*. *Applied Physics Letters* **111**, 17, p. 173103 (2017). www.doi.org/10.1063/1.4987021
- [58] Faucett, A.C., *et al.*, *Evolution, structure, and electrical performance of voltage-reduced graphene oxide*. *FlatChem* **1**, p. 42-51 (2017). www.doi.org/10.1016/j.flatc.2016.10.003
- [59] Kumar, R., *et al.*, *Charge transport mechanism of hydrazine hydrate reduced graphene oxide*. *IET Circuits, Devices & Systems* **9**, 6, p. 392-396 (2015).
- [60] Rai, V., *et al.*, *Correlating Chemical Structure and Charge Transport in Reduced Graphene Oxide for Transparent Conductor and Interconnect Applications*. in *2015 IEEE International Symposium on Nanoelectronic and Information Systems*. 2015.
- [61] Muchharla, B., *et al.*, *Temperature dependent electrical transport of disordered reduced graphene oxide*. *2D Materials* **1**, 1, p. 011008 (2014). www.doi.org/10.1088/2053-1583/1/1/011008
- [62] Wang, S.-W., *et al.*, *Transport behavior and negative magnetoresistance in chemically reduced graphene oxide nanofilms*. *Nanotechnology* **22**, 33, p. 335701 (2011). www.doi.org/10.1088/0957-4484/22/33/335701
- [63] Kim, H.-J., *et al.*, *Charge Transport in Thick Reduced Graphene Oxide Film*. *The Journal of Physical Chemistry C* **119**, 51, p. 28685-28690 (2015). www.doi.org/10.1021/acs.jpcc.5b10734
- [64] Negishi, R., *et al.*, *Band-like transport in highly crystalline graphene films from defective graphene oxides*. *Scientific Reports* **6**, 1, p. 28936 (2016). www.doi.org/10.1038/srep28936
- [65] Vianelli, A., *Charge transport in Reduced Graphene Oxide Thin Films*, PhD Thesis; Università di Modena e Reggio Emilia (2016). <https://morethesis.unimore.it/theses/available/etd-02162016-220621/>
- [66] Kovtun, A., *2D graphene-based materials: interplay between composition and electrical properties.*, PhD Thesis; Università di Modena e Reggio Emilia (2017). <https://morethesis.unimore.it/theses/available/etd-02162016-220621/>; Kovtun, A., *et al.*, *Multiscale Charge Transport in van der Waals Thin Films: Reduced Graphene Oxide as a Case Study*. *ACS Nano* **15**, 2, (2021). www.doi.org/10.1021/acsnano.0c07771
- [67] Noriega, R., *et al.*, *Charge Transport Theories in Organic Semiconductors*, in *Organic Electronics II*, H. Klauk, Wiley, p. 67-104 (2012). www.doi.org/10.1002/9783527640218

- [68] Anderson, P.W., *Absence of Diffusion in Certain Random Lattices*. Physical Review **109**, 5, p. 1492-1505 (1958). www.doi.org/10.1103/PhysRev.109.1492
- [69] Pollak, M., *Electrons in Anderson–Mott insulators*. The European Physical Journal Special Topics **227**, 15, p. 2221-2240 (2019). www.doi.org/10.1140/epjst/e2018-800055-9
- [70] Ashcroft, N.W., et al., *Solid state physics* Thomson Press (1976).
- [71] Ambegaokar, V., et al., *Hopping Conductivity in Disordered Systems*. Physical Review B **4**, 8, p. 2612-2620 (1971). www.doi.org/10.1103/PhysRevB.4.2612
- [72] Hamilton, E.M., *Variable range hopping in a non-uniform density of states*. The Philosophical Magazine: A Journal of Theoretical Experimental and Applied Physics **26**, 4, p. 1043-1045 (1972). www.doi.org/10.1080/14786437208226975; Mott, N.F., *Conduction in non-crystalline materials*. The Philosophical Magazine: A Journal of Theoretical Experimental and Applied Physics **19**, 160, p. 835-852 (1969). www.doi.org/10.1080/14786436908216338
- [73] Shklovskii, B.I., et al., *Correlation Effects on the Density of States and Hopping Conduction, in Electronic properties of doped semiconductors*, Springer-Verlag, (1984).
- [74] Imry, J., *Introduction to Mesoscopic Physics*, Oxford University Press (1997). ; Mott, N.F., *Metal-Insulator Transition*. Reviews of Modern Physics **40**, 4, p. 677-683 (1968). www.doi.org/10.1103/RevModPhys.40.677
- [75] Castellani, C., et al., *Interaction-driven metal-insulator transitions in disordered fermion systems*. Physical Review B **30**, 2, p. 527-543 (1984). www.doi.org/10.1103/PhysRevB.30.527; Gebhard, F., *Metal–Insulator Transitions, in The Mott Metal-Insulator Transition: Models and Methods*, F. Gebhard, Springer Berlin Heidelberg, p. 1-48 (1997). www.doi.org/10.1007/3-540-14858-2_1
- [76] Larkin, A., et al., *Activation conductivity in disordered systems with large localization length*. Sov. Phys. JETP **56**, 3, p. 647 (1982).
- [77] Aleshin, A.N., et al., *One-Dimensional Transport in Polymer Nanofibers*. Physical Review Letters **93**, 19, p. 196601 (2004). www.doi.org/10.1103/PhysRevLett.93.196601
- [78] Kronemeijer, A.J., et al., *Universal Scaling in Highly Doped Conducting Polymer Films*. Physical Review Letters **105**, 15, p. 156604 (2010). www.doi.org/10.1103/PhysRevLett.105.156604
- [79] Choi, A., et al., *Probing spin-charge relation by magnetoconductance in one-dimensional polymer nanofibers*. Physical Review B **86**, 15, p. 155423 (2012). www.doi.org/10.1103/PhysRevB.86.155423; Kim, K.H., et al., *Apparent Power Law Scaling of Variable Range Hopping Conduction in Carbonized Polymer Nanofibers*. Scientific Reports **6**, 1, p. 37783 (2016). www.doi.org/10.1038/srep37783
- [80] Kang, E.S.H., et al., *Multi-barrier field-emission behavior in PBTTT thin films at low temperatures*. Scientific Reports **5**, 1, p. 8396 (2015). www.doi.org/10.1038/srep08396
- [81] Asadi, K., et al., *Polaron hopping mediated by nuclear tunnelling in semiconducting polymers at high carrier density*. Nature Communications **4**, 1, p. 1710 (2013). www.doi.org/10.1038/ncomms2708
- [82] van der Kaap, N.J., et al., *Charge transport in disordered semiconducting polymers driven by nuclear tunneling*. Physical Review B **93**, 14, p. 140206 (2016). www.doi.org/10.1103/PhysRevB.93.140206
- [83] Turton, D.A., et al., *Accurate Analysis of Fluorescence Decays from Single Molecules in Photon Counting Experiments*. Analytical Chemistry **75**, 16, p. 4182-4187 (2003). www.doi.org/10.1021/ac034325k
- [84] Zabrodsky, A., et al., *Effect of doping inhomogeneities on the conductivity of heavily doped and compensated semiconductors*. Fizika Tekhn. Poluprov. **9**, 3, p. 587-589 (1975).
- [85] Reghu, M., et al., *Metal-insulator transition in doped conducting polymers, in Handbook of conducting polymers*, p. 27-84 (1998).
- [86] Novoselov, K.S., et al., *2D materials and van der Waals heterostructures*. Science **353**, 6298, p. aac9439 (2016). www.doi.org/10.1126/science.aac9439
- [87] Chen, J.-H., et al., *Intrinsic and extrinsic performance limits of graphene devices on SiO₂*. Nature Nanotechnology **3**, 4, p. 206-209 (2008). www.doi.org/10.1038/nnano.2008.58; Tan, Y.W., et al., *Temperature dependent electron transport in graphene*. The European Physical Journal Special Topics **148**, 1, p. 15-18 (2007). www.doi.org/10.1140/epjst/e2007-00221-9
- [88] Buchowicz, G., et al., *Correlation between structure and electrical transport in ion-irradiated graphene grown on Cu foils*. Applied Physics Letters **98**, 3, p. 032102 (2011). www.doi.org/10.1063/1.3536529; Thiyagarajan, K., et al., *Defect-induced metallic-to-semiconducting transition in multilayer graphene*. RSC Advances **5**, 22, p. 16821-16827 (2015).

- www.doi.org/10.1039/C4RA13703E; Zion, E., et al., *Localization of Charge Carriers in Monolayer Graphene Gradually Disordered by Ion Irradiation*. *Graphene* **4**, p. 45-53 (2015). www.doi.org/10.4236/graphene.2015.43005
- [89] Kumari, A., et al., *Electrical transport properties of polycrystalline CVD graphene on SiO₂/Si substrate*. *Diamond and Related Materials* **45**, p. 28-33 (2014). www.doi.org/10.1016/j.diamond.2014.03.003
- [90] Chuang, C., et al., *Experimental evidence for Efros–Shklovskii variable range hopping in hydrogenated graphene*. *Solid State Communications* **152**, 10, p. 905-908 (2012). www.doi.org/10.1016/j.ssc.2012.02.002; Elias, D.C., et al., *Control of Graphene's Properties by Reversible Hydrogenation: Evidence for Graphane*. *Science* **323**, 5914, p. 610 (2009). www.doi.org/10.1126/science.1167130
- [91] Gómez-Navarro, C., et al., *Electronic Transport Properties of Individual Chemically Reduced Graphene Oxide Sheets*. *Nano Letters* **7**, 11, p. 3499-3503 (2007). www.doi.org/10.1021/nl072090c
- [92] Eda, G., et al., *Large-area ultrathin films of reduced graphene oxide as a transparent and flexible electronic material*. *Nature Nanotechnology* **3**, 5, p. 270-274 (2008). www.doi.org/10.1038/nnano.2008.83; Hwang, H., et al., *Highly Tunable Charge Transport in Layer-by-Layer Assembled Graphene Transistors*. *ACS Nano* **6**, 3, p. 2432-2440 (2012). www.doi.org/10.1021/nn2047197; Lee, J., et al., *Tuning of n- and p-Type Reduced Graphene Oxide Transistors with the Same Molecular Backbone*. *Chemistry – A European Journal* **18**, 17, p. 5155-5159 (2012). www.doi.org/10.1002/chem.201103554
- [93] Joung, D., et al., *High yield fabrication of chemically reduced graphene oxide field effect transistors by dielectrophoresis*. *Nanotechnology* **21**, 16, p. 165202 (2010). www.doi.org/10.1088/0957-4484/21/16/165202; Wang, L., et al., *Facile preparation of an n-type reduced graphene oxide field effect transistor at room temperature*. *Chemical Communications* **50**, 10, p. 1224-1226 (2014). www.doi.org/10.1039/C3CC47224H
- [94] Haque, A., et al., *Temperature Dependent Electrical Transport Properties of High Carrier Mobility Reduced Graphene Oxide Thin Film Devices*. *IEEE Transactions on Semiconductor Manufacturing* **31**, 4, p. 535-544 (2018). www.doi.org/10.1109/TSM.2018.2873202
- [95] Silverstein, K.W., et al., *Voltage-reduced low-defect graphene oxide: a high conductivity, near-zero temperature coefficient of resistance material*. *Nanoscale* **11**, 7, p. 3112-3116 (2019). www.doi.org/10.1039/C8NR08285E
- [96] Kurnosov, N.V., et al., *Comparison of temperature dependences of electrical conductivity of composite rGO-SWNT film with rGO and SWNT films*. *Low Temperature Physics* **46**, 3, p. 285-292 (2020). www.doi.org/10.1063/1.0000700
- [97] Shaina, P.R., et al., *Anomalous charge transport in reduced graphene oxide films on a uniaxially strained elastic substrate*. *Journal of Physics: Condensed Matter* **29**, 23, p. 235301 (2017). www.doi.org/10.1088/1361-648x/aa6eba
- [98] Govor, L.V., et al., *Coulomb gap and variable-range hopping in self-organized carbon networks*. *Journal of Applied Physics* **90**, 3, p. 1307-1313 (2001). www.doi.org/10.1063/1.1383021
- [99] Marcus, R.A., *Electron transfer reactions in chemistry. Theory and experiment*. *Reviews of Modern Physics* **65**, 3, p. 599-610 (1993). www.doi.org/10.1103/RevModPhys.65.599
- [100] Egger, R., et al., *Quantum rates for nonadiabatic electron transfer*. *The Journal of Chemical Physics* **100**, 4, p. 2651-2660 (1994). www.doi.org/10.1063/1.466460
- [101] Brédas, J.L., et al., *Organic semiconductors: A theoretical characterization of the basic parameters governing charge transport*. *Proceedings of the National Academy of Sciences* **99**, 9, p. 5804 (2002). www.doi.org/10.1073/pnas.092143399
- [102] Di Filippo, G., et al., *The evolution of hydrogen induced defects and the restoration of π -plasmon as a monitor of the thermal reduction of graphene oxide*. *Applied Surface Science* **512**, p. 145605 (2020). www.doi.org/10.1016/j.apsusc.2020.145605
- [103] Koren, E., et al., *Coherent commensurate electronic states at the interface between misoriented graphene layers*. *Nature Nanotechnology* **11**, 9, p. 752-757 (2016). www.doi.org/10.1038/nnano.2016.85
- [104] Marchand, D., et al., *Surface structure and electrical conductivity of natural and artificial graphites*. *Carbon* **22**, 6, p. 497-506 (1984). [www.doi.org/10.1016/0008-6223\(84\)90082-4](http://www.doi.org/10.1016/0008-6223(84)90082-4); Matsubara, K., et al., *Electrical resistance in the c direction of graphite*. *Physical Review B* **41**, 2, p. 969-974 (1990).

- [105] www.doi.org/10.1103/PhysRevB.41.969; Tsang, D.Z., *et al.*, *The c-axis electrical conductivity of kish graphite*. *Carbon* **14**, 1, p. 43-46 (1976). [www.doi.org/10.1016/0008-6223\(76\)90081-6](http://www.doi.org/10.1016/0008-6223(76)90081-6)
Prigodin, V.N., *et al.*, *Metal-insulator transition in an irregular structure of coupled metallic chains*. *Synthetic Metals* **65**, 2, p. 195-201 (1994). [www.doi.org/10.1016/0379-6779\(94\)90181-3](http://www.doi.org/10.1016/0379-6779(94)90181-3)

Chapter 3

SAMPLES FABRICATION

The purpose of this chapter is presenting the routes used for synthesising GRM sheets and the techniques employed for fabricating investigated GRM films.

3.1 GRM Synthesis

In this thesis work, we employed lab-made graphene oxide (GO) that was synthesised by C. Bettini at CNR-ISOF. The process is a modification of the classic Hummers' method [106] and it is schematised in Figure 3-1. Commercial graphite flakes, with diameter less than 500 μm , were water suspended and oxidized in the presence of sodium nitrate (NaNO_3), sulfuric acid (H_2SO_4) and potassium permanganate (KMnO_4). Graphite exfoliation occurs by continuous mechanical stirring of the suspension. The final GO was washed several times, centrifuged and dried. Further details are present in supporting information of reference [107].

The repeatability of the synthesis protocol from batch to batch and the stability in time of the material have been internally verified. Despite that, to fully avoid any tiny discrepancy,

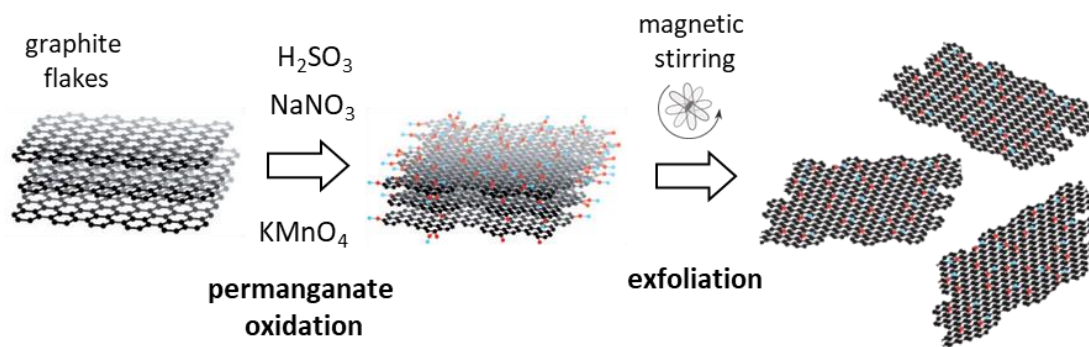


Figure 3-1. Scheme of GO synthesis following a modified Hummer's method.

we used the same batch and the same suspension of GO for fabricating all the RGO samples.

As synthesised GO powder was suspended at 2.5 g/L concentration in ultrapure water. The suspension was sonicated in a water bath (37kHz, 30W) for 6 hours. This treatment triggers bulk fragmentation of larger GO sheets and allows to obtain a narrower size distribution of sheets [108].

More than 99% of used GO sheets are mono-atomic in thickness – around 1 nm thick on ultra-flat silicon – as observed by atomic force and electronic microscopies.

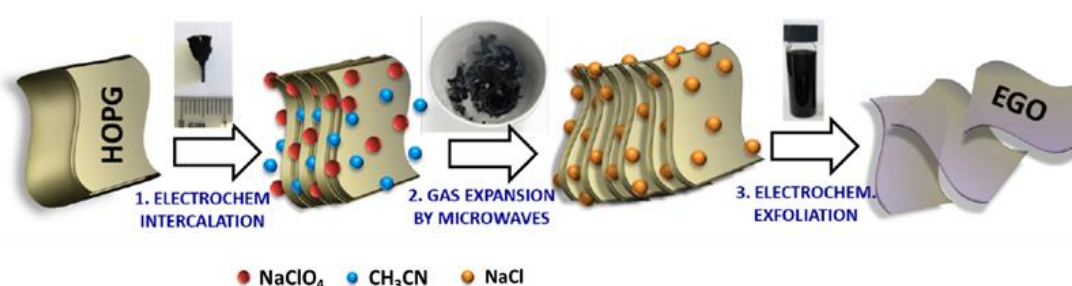


Figure 3-2. Scheme of EGO synthesis protocol. Image was taken from ref. [36].

The EGO used in this work was synthesised by F. Poletti at CNR-ISOF according to the method of reference [36], illustrated in Fig. 3-2. Commercial graphite flakes were pressed in a nylon bag with filter mesh and electrically connected to a platinum foil. This acted as a working electrode in an electrochemical cell with another platinum wire as counter electrode and an ionic solution made of sodium perchlorate dissolved in acetonitrile (1 mol L^{-1}). During the electrochemical treatment, uncharged acetonitrile molecules intercalated in the graphite aided by the synergistic action of perchlorate ions. Then, the graphite was placed in a microwaves oven and acetonitrile molecules were decomposed by microwaves, causing gas production and promoting a rapid (few seconds) expansion of graphite. The expanded graphite was again inserted in the electrochemical cell for the final exfoliation with sulfuric acid (H_2SO_4 , 0.1 mol L^{-1}). The resulting material was collected by filtration and it was cleaned by repeated washing with deionized water. Finally, the powder was re-dispersed in DMF through sonication and the suspension was centrifuged at 2k rpm to remove any re-aggregated particles.

3.2 GRM Films Fabrications

The possibility to suspend GRM in water or other suitable solvents, as well as the ability of some GRM to self-assemble, allow to exploit the wide portfolio of fabrication techniques of wet chemistry. We used three main techniques to fabricate our thin films. They are spin-coating deposition, spray-coating deposition and vacuum-assisted filtration. The aim is understanding if different network structures arise and if advantages/differences in the charge transport verifies in these systems.

Spin-coating deposition

Spin-coating is a solution-based deposition. For its simplicity, it has become one of the most known, and used, technique to fabricate thin films on a substrate, especially in organic electronics and polymer chemistry *R&D*. It relies on the competition of centrifugal forces and viscous ones generating in a polymer suspension or in a particle suspension, which is forced to spin at thousands of revolutions per minute. A typical spin-coating process is divided in four sequential steps depicted in Figure 3-3: suspension deposition, spin-up, spin-off and evaporation [109]. In the first step, an amount of suspension is drop-casted on the chosen substrate at rest. The liquid should be in excess compared to the one that the desired coating would require. The substrate is vacuum tightened to the rotor stage and centred to its axis of rotation. The vacuum pressure and the planarity of the substrate with respect to the rotation plane should be carefully adjusted. A deviation from planarity creates asymmetric forces during spinning which badly influence the uniformity of the film. In spin-off, the substrate is made to spin at constant radial acceleration. The generated centrifugal force causes the liquid to flow radially outward. The spin-off phase starts when the substrate has reached the target angular speed and (angular) acceleration is zero. The suspension constitutes a uniform film which thins as the liquid in excess at the substrate perimeter is swept away. During this phase, the non-volatile part of the suspension – *i.e.* particles, molecules, polymer chains etc - aggregates and deposits on the substrate. The thinning of the liquid film comes with an increased viscosity of the suspension and, indeed, a slow-down of the remaining liquid flow and of the spin-off process. If the uniformity of the film breaks, as it happens at the substrate edges, a larger amount of material is accumulated. This is evident in our squared dies,

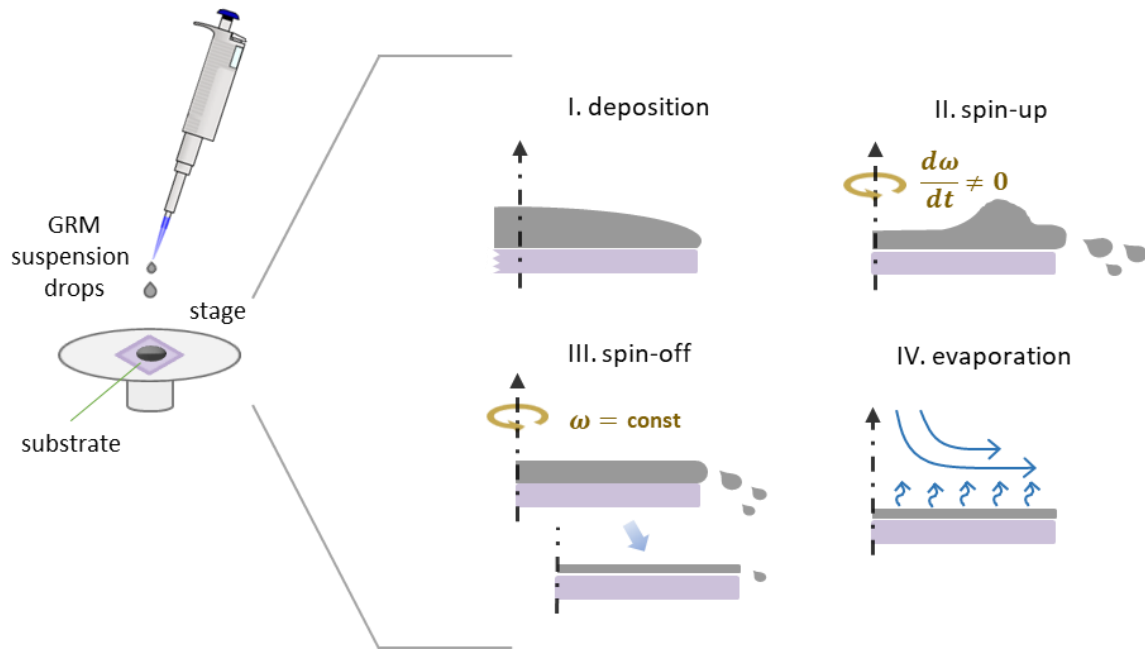


Figure 3-3. Scheme of a spin-coating deposition. Each phase of the method is illustrated separately. The deposited GRM suspension is depicted in dark grey on the top of a substrate (e.g. SiO_2), in lavender.

where thicker film regions are visible at the four corners. At a certain moment, spin-off stops and evaporation becomes the main mechanism of thinning. Once the thinning is terminated and the coating is deposited, the rotation of the substrate is halted.

The easiest way of modelling the process is assuming the solution as a Newtonian fluid, *i.e.* shear stress arising from the fluid flow is linear with shear velocity. Solution concentration C , solution viscosity η , angular velocity ω , as well as substrate characteristics, solvent physicochemical properties (boiling point, volatility) and solute diffusivity are all key parameters that influence thickness t and surface morphology of the deposited film [110]. For a flat substrate and sufficiently high velocity ($\omega \sim 10^3$ rpm), the film thickness t increases with increasing C and increasing η , while it decreases with increasing ω . However, rheology of GRM water-based suspensions can be greatly tuned by a little variation of the concentration [111]. For instance, the intrinsic 2D nature of GO, and so its high aspect ratio, gives GO suspensions particular viscoelastic properties: they behave like typical fluids at low concentration (<0.06 g/L) and like a gel at high concentration (>2.4 g/L). At medium concentrations, they have intermediate response between fluid-like and gel-like behaviour [112]. Thus, the thickness of spin-coated GRM

films cannot be easily predicted by empirical formulas for polymers found in literature [113].

Concerning the influence of solvent properties on film thickness, for a given initial viscosity, more volatile the solvent is thicker the film will result. In an effective solvent for good film uniformity, solvent-solute molecular interactions should be favoured with respect to solute-solute and solvent-solvent ones.

Pre- and post-treatment could also be performed. They do not constitute, strictly speaking, part of the spin-coating deposition, but they could be fundamental to achieve satisfying results. Thermal curing of a spin-coated polymer film is a common example of post-treatment. We performed an air plasma treatment of the substrates before the deposition. This treatment increases the hydrophilicity of the substrate and it improves the solution-substrate compatibility. In fact, enhanced solute-substrate interfacial interactions could affect positively the final deposition result.

In the present work, we used spin-coating method to deposit a GRM film on a desired flat substrate, for example monocrystalline doped silicon (Si), thermal-growth SiO₂ on Si or quartz.

We utilized a WS-650Mz spin-coater of Laurell Tech. Corp. for all depositions. It is equipped with different supports to firmly hold substrate of different sizes and thicknesses. Spin-coating is quite effective in producing uniform GO film starting from aqueous suspensions, while it was impossible to fabricate uniform EGO film. In fact, EGO sheets tend to aggregate in 3D islands and the suspension film breaks during the spin-off phase. The main reasons are the low concentration achievable in low boiling point solvent and the morphology distribution of the suspended sheets.

Except where stated differently, we used an angular acceleration of 0.5 rpm/min and an angular velocity of 2k rpm. These parameters were carefully optimized according to the characteristic of GRM materials and to the type of instrument present in the lab. Despite a spinning time of around 1 min is enough to get a good GO coating, the value of 3 min was chosen to permit a complete evaporation of the solvent. With previous parameters, GO suspension at 2.5g/L concentration produces almost three uniform layers on a cleaned and plasma treated silicon die. We performed sequential spin coating depositions (up to 50) to fabricate film tens of nm thick. We could have reached similar values of thickness by spin-coating a more concentrated suspension (>4g/L) at lower angular velocities (<1k

rpm). We intentionally did not follow this route because lead to greater inhomogeneities in the film surface [114].

At higher dilution ($<0.3\text{g/L}$) was instead possible to deposit isolated GO sheets - but also other GRM – in order to study their morphology by microscopic means.

Filtration

The method of filtration to fabricate membranes, and specifically GO ones, is as old as it is simple [115]. The basic principle consists in dropping the GRM suspension in a collecting cylinder (*i.e.* the funnel) with a porous filtering membrane (*i.e.* the filter) at the base. While the solvent passes through the filter to reach a reservoir, the GRM sheets self-assemble and coat the filter. The procedure could be realised “spontaneously” or by inducing a differential pressure between the funnel and the reservoir. In the first case, the filtration occurs by a combination of gravity force acting on the suspension and of the slow natural evaporation of the solvent. In the second case, we talk of pressure-assisted filtration, if a pressure greater than the ambient one is created on the cylinder part, or of vacuum-assisted filtration, if a pressure lower than the ambient one is created on the reservoir. These two last routes permit a high control of the coating formation and its reproducibility, which is extremely difficult to achieve with the spontaneous-evaporation method by the high number of parameters at stake.

We always employed the vacuum-assisted technique for the simplicity and low-cost of the needed equipment. Conversely to what reported elsewhere [116] and as it visible in the inset of Fig. 3-4a, we did not observe inhomogeneities in the coating on the filter. Hereafter, filtration and filtered film are used in place of vacuum-assisted filtration and vacuum-assisted filtered film, respectively.

The apparatus we used is represented in Fig. 3-4a and it is commercially available by different vendors as glass Büchner funnel. It is composed by a glass flask, a glass object containing the porous plate/septum and a glass funnel. The glass flask, that acts as a solvent reservoir, has a side connection for the vacuum pump. We used a membrane pump which allows a minimum rough vacuum of 7 mbar and a flow of 32 L/min. The flask and the support are joined by a rubber bung, which also seals the flask. The filter membrane is placed in between the porous plate/septum and the funnel cylinder. The

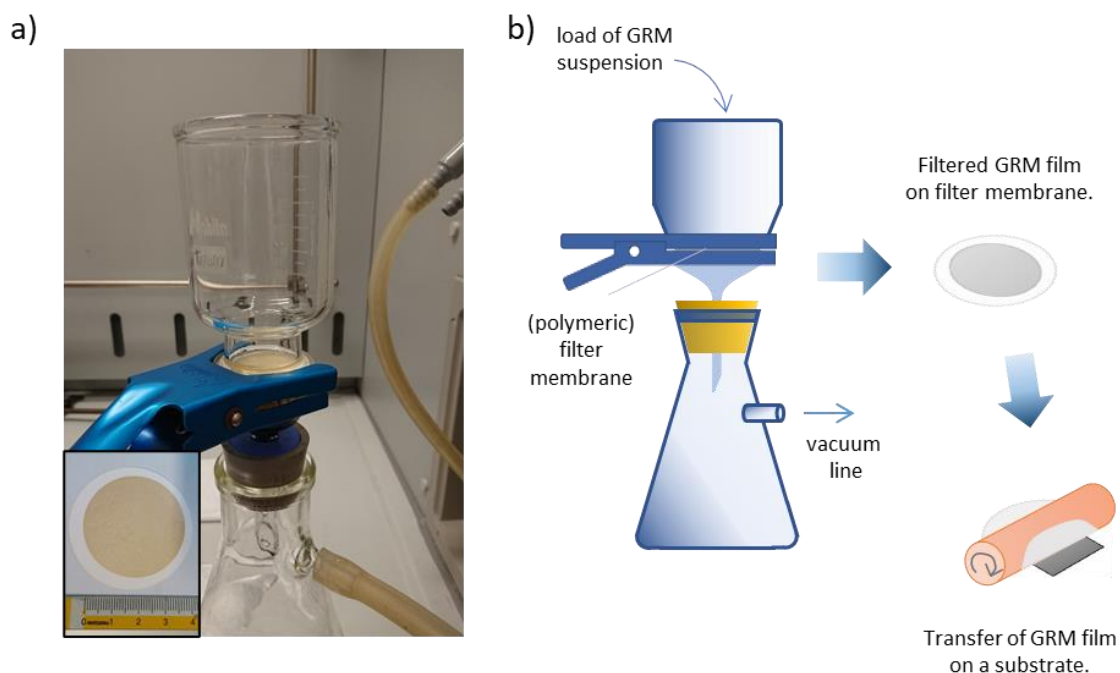


Figure 3-4. (a) Photograph of the vacuum-assisted filtration equipment. The inset shows a GO film on a nylon filter membrane. (b) Scheme of the GRM film fabrication by vacuum-assisted filtration.

three elements are kept in position by a large clamp. We had a funnel with a base internal diameter of 40mm.

The process is performed as follows. The equipment is mounted and the column is firmly fixed to a metal base in order to not inadvertently move it during the filtration. The membrane filter is washed with ultrapure water to remove possible impurities. A known amount of greatly diluted GRM suspension is dropped in the funnel with the pump turned off. The solvent in excess increases the filtration time and it aids the formation of a compact film without accumulated and sparsely distributed material [117]. We usually employed GRM suspensions with a concentration lower than 0.02g/L and a volume larger than 20mL. Then, the pump is turned on. The process lasts few minutes based on the quantity of liquid to filter and the size of suspended particles/sheets. Once the film is dried, we turn off the pump and we rapidly transfer the film on the desired substrates. The transfer is realized mechanically by pressing the back of the filter/GRM film on the substrate with a small rolling pin. The pin is manually rolled back and forth few times. We estimated an applied pressure of (60÷140) kPa by considering the size of the pin. A successful transfer needs a good mechanical stability of the GRM film and a higher

adhesion energy of the film/substrate interface with respect to the film/filter interface. Hence, a low content of residual solvent on the film exposed surface is a fundamental requirement. Before the transfer, substrates are cleaned and, when permitted by their characteristics, plasma treated. The importance of the plasma treatment should not be undervalued in case of a silicon substrate: the treatment favours the hydrophilicity of the silicon surface and avoid that residual water damage the depositing film. For the way the transfer occurs, a uniaxial tension is applied to the GRM film in the direction of rolling. It has been shown that this stretch of the film regulates spontaneous wrinkles formed in the filtration and improve its crystalline order on the μ metric scale [118].

The characteristics of filter membrane are extremely important in the film fabrication. We utilized membrane with an average porosity of 0.22 μ m or less to collect almost all the GRM sheets, but to also keep the influence of the filter surface morphology as little as possible in the assembly of them. Filters could be made of inorganic materials or of polymers. The best filter for fabricating self-standing GRM films is in alumina (Al_2O_3 ; Whatman® Anodisc). They have a tubular porous structure, with the main part of pores aligned perpendicular to the membrane plane. This permits an efficient and ordered assembling of the GRM sheets and easy peeling of the formed film/membrane. Al_2O_3 filters have two disadvantages: they are expensive compared to other organic filters, around 10 euro/piece against few euro/piece; and they are extremely fragile, making the transfer of the film impossible. Thus, we tested the filtration process with different polymer-based filters. The optimum results in terms of film uniformity and film detaching were obtained with a nylon_{6,6} filter (Axiva), which we used to fabricate all transferred GRM films. Transfers can also be achieved by dissolving the polymeric filter in a suitable solvent – *i.e.* cellulose acetate in acetone – and by fishing the floating film with the desired substrate. However, following this route, the number of solvent residues in the sample is larger than with the mechanical transfer.

We filtered from 0.2mg to 0.6mg of material for fabricating GO and EGO, SiO_2 supported thin films.

Spray-coating deposition

Spray-coating involves atomising – break up in μm droplets – a suspension and direct it towards the substrate to coat. It is a widespread technique in manufacturing because allows to fast coat surfaces with different morphologies.

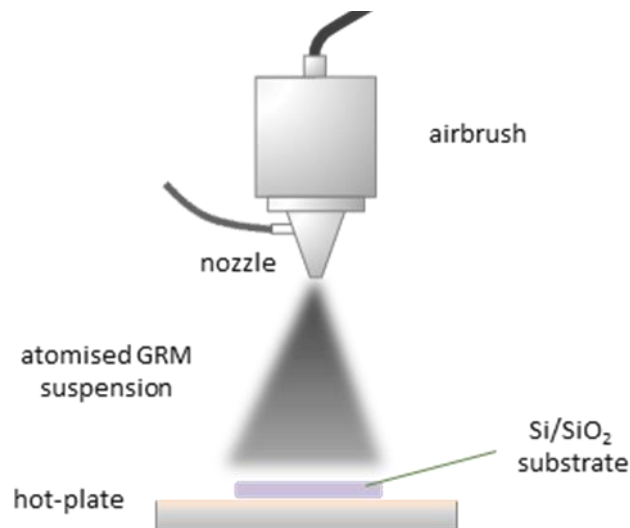


Figure 3-5. Scheme of GRM film fabrication by the spray-coating process.

Spray-coated GRM films investigated in this work were fabricated by C. Anichini at University of Strasbourg (France) with the set-up schematised in Figure 3-5. He employed a commercial airbrush gun for modelling and painting with a 0.3 needle-shaped nozzle. The gun was vertically mounted on a lab-designed three axis motor unit. In this case, the atomisation occurs via a compressed nitrogen-assisted process. The GRM suspension exits from the instrument nozzle at low speed and it is surrounded by a high-speed stream of nitrogen. Friction between the liquid and nitrogen molecules accelerates and disrupts the fluid (nitrogen + suspension) stream forming droplets. The nitrogen is supplied at the pressure of 1.5 bar. The substrate, thermal growth SiO_2 on crystalline Si, is pre-heated at 80°C to ease the evaporation of the solvent. The suspension GRM concentration is an important parameter to optimise in this technique, increasing the amount of GRM per unit of solvent volume causes an increase of suspension viscosity. Viscosity influences greatly the atomisation: higher the viscosity is, harder atomising the suspension will be and, indeed, larger the droplets will be. Hence, more solvent needs to be removed from the substrate making the formation of a uniform GMR film not viable. GO suspension was

supplied to the system (spray coater) at 1g/L optimized concentrations. Only the DMF-suspended EGO was tested with this technique. DMF posed two concurring problems that prevented a successful deposition: (i) it eroded plastic parts in the gun, that had to be removed before the deposition; and (ii) it did not evaporate rapidly enough for the film formation. We were not able to test IPA-suspended EGO, but we are confident that the issues can be overcome in this way.

Films post-processing

We performed thermal treatments of deposited GRM films in order to change their chemical composition and improve the “chemical order” – that is the extension of C sp² aromatic regions. The treatments were all carried out in a custom-made tube furnace at high vacuum. A schematic of the furnace is depicted in Figure 3-6. The furnace has the tubular treatment chamber separated by a sample insertion chamber, which can allocate up to 9 boat-shaped holders. The heating is accomplished by metal resistances which surround the tube chamber. The resistances and the tube are enclosed in a cage made of refractory material. This avoids heat dissipations and aid to obtain a homogeneous environment around the heated volume. Hence, temperature up to 900°C can be achieved. The temperature is measured by a thermocouple placed just outside the tube. A correction factor is used to consider the gradient of temperature between the inside of the tube, under vacuum, and the outside. The pumping system is composed of a turbomolecular pump in series with an oil rotary pump. It pumps the two chambers simultaneously. Chamber pressure lower than 10⁻⁶ mbar can be maintained during the treatment. Heating power and chamber temperature are accurately controlled by a 920P Eurotherm controller, equipped with a PID feedback loop. In the treatment of solution processed GRM is extremely important to tune the heating rate. In fact, it is desirable to keep it as low as possible in order to avoid abrupt solvent evaporation and ease structural changes (*i.e.* expansion), which can occur during the departure of oxygens from the GRM chemical functionalities. Usually, the heating rate was kept at 1K/min and 5K/min between room T and 250 °C and between 250 °C and 900 °C, respectively. This allowed to lower treatment-induced issues, as well as to make the treatment lasts not more than few hours.

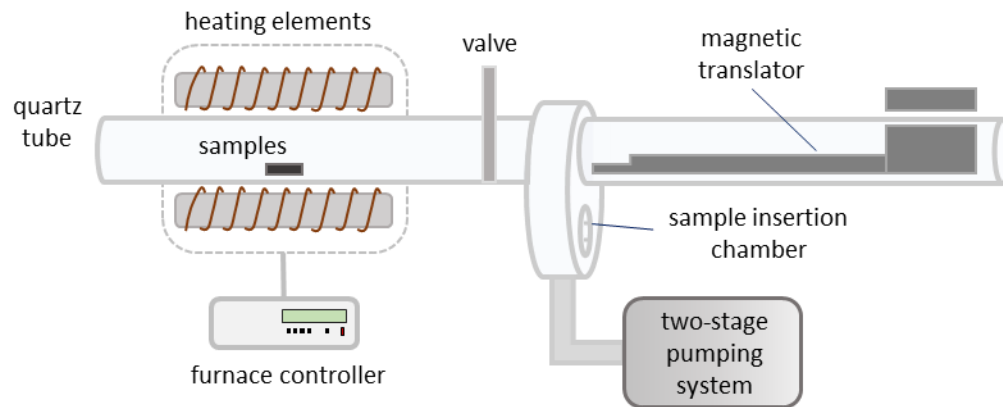


Figure 3-6. Scheme of the tube furnace used in this work for GRM thermal treatment at high vacuum.

Oxidised GRM films always undergo a thickness decrease upon thermal treatment. Indeed, the removal of oxygen functionalities causes a reduction in thickness of the sheets and, in turns, the film structure gently collapses. Concerning the chosen thickness values, we tried to reach films thicknesses that were high enough to model realistic networks on one hand, but that could still not be considered bulky (so, “thin”) on the other.

Few extra cares are needed in the case of free-standing, μm -thick membrane fabricated by filtration with respect to supported films. The reason lies on the mentioned thickness reduction on one hand, and on gases release during the reduction on the other. To obtain a successful reduction, we sandwiched the membrane between two clean silicon chips, that are kept in place by a tungsten clip.

For each supported GRM film, we performed an additional post-fabrication step: we removed with a toothpick less than 0.5 mm of material from the substrate border. In the case of Si/SiO₂ substrates, this has the dual goal of permitting direct thickness measurements and of avoiding to electrically connect the studied film with the silicon underneath. The removal is quite simple with GO on SiO₂, while it becomes more difficult with decreasing oxygen content in the GRM and multiple “scratching” passes are needed

Electrodes fabrication

To perform electrical characterizations, metallic electrodes were deposited on GRM films. The electrodes were fabricated by thermal evaporation of pure (99.99%) gold. The electrodes thickness was of the order of tens of nm and was varied based on the thickness

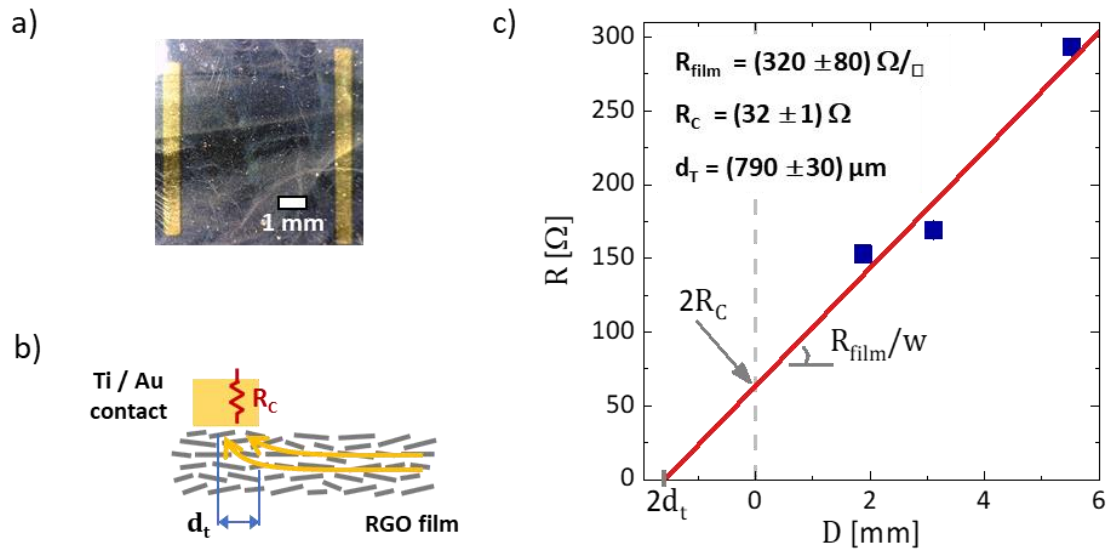


Figure 3-7. (a) Optical image of a RGO film (in dark grey) with evaporated Ti/Au electrodes (in yellow). Samples with this 2 parallel line electrode configuration were used to estimate the contact resistance R_C at the RGO/electrode interface. (b) Scheme of the film/contact geometry with R_C and the transfer length d_t highlighted. (c) Plot of 2-probe resistance R as a function of the electrodes distance D for three different devices (blue squares), following the transfer length method. The linear fit (red curves) permits to estimate R_C , as well as the film resistance R_{film} and d_t .

of the GRM film underneath. A thin layer of titanium (Ti), or less frequently chromium (Cr), was deposited before gold to facilitate the adhesion of the electrode to the film. Electrodes geometries and their size were varied by interposing different shadow masks during the deposition. The electrode geometry that was used for electrical charge transport measurements has four round electrodes in the corner of a square. In this case, the size of the electrode and their reciprocal distance was 0.5 mm or 1 mm and 9 mm or 4 mm, respectively, based on the size of the film.

We estimated the contact resistance R_C at the GRM/electrode interface by employing the transfer length method [119]. It consists in measuring the resistance between two electrodes as a function of their distance D . If all the electrode geometrical properties are equal, the R versus D plot supplies several information on the formed electrical interface. The intercept at zero distance indicates the double of R_C , while the slope gives the resistance R_{film} of the studied film only. The length wherein carriers are effectively

injected from the electrodes, called transfer length d_T , is also estimated by half of the (negative) intercept at zero resistance.

For this purpose, we fabricated identical RGO filtered films on Si/SiO₂ with couples of Ti/Au electrodes. A microscopic image is shown in Figure 3-7a. Each electrode had a width of 8 mm a length of 1 mm. We applied a potential difference ranging between 10mV and 500mV. The contact resistance resulted around one tenth of the film resistance, as presented in 3-8b. Indeed, we can safely state that the fabricated interface forms an ohmic contact and the influence of the metal electrodes is marginal in the film electrical measurement. Moreover, we estimated a film-electrode effective, injection distance - *i.e.* transfer length d_t - of several hundreds of μm that well compares with the electrode length. This indicates that current crowding effects at the electrode edge are present but limited.

3.3 References

- [36] Xia, Z.Y., *et al.*, *Synergic Exfoliation of Graphene with Organic Molecules and Inorganic Ions for the Electrochemical Production of Flexible Electrodes*. *ChemPlusChem* **79**, 3, p. 439-446 (2014). www.doi.org/10.1002/cplu.201300375
- [106] Hummers, W.S., *et al.*, *Preparation of Graphitic Oxide*. *Journal of the American Chemical Society* **80**, 6, p. 1339-1339 (1958). www.doi.org/10.1021/ja01539a017
- [107] Treossi, E., *et al.*, *High-Contrast Visualization of Graphene Oxide on Dye-Sensitized Glass, Quartz, and Silicon by Fluorescence Quenching*. *Journal of the American Chemical Society* **131**, 43, p. 15576-15577 (2009). www.doi.org/10.1021/ja9055382
- [108] Liscio, A., *et al.*, *Evolution of the size and shape of 2D nanosheets during ultrasonic fragmentation*. *2D Materials* **4**, 2, p. 025017 (2017). www.doi.org/10.1088/2053-1583/aa57ff
- [109] Scriven, L.E., *Physics and Applications of DIP Coating and Spin Coating*. *MRS Proceedings* **121**, p. 717 (2011). www.doi.org/10.1557/PROC-121-717
- [110] Das, R., *Fabrication and Properties of Spin-Coated Polymer Films*, in *Nano-size Polymers*, S. Fakirov, Springer, p. 283-386 (2016). www.doi.org/10.1007/978-3-319-39715-3
- [111] Naficy, S., *et al.*, *Graphene oxide dispersions: tuning rheology to enable fabrication*. *Materials Horizons* **1**, 3, p. 326-331 (2014). www.doi.org/10.1039/C3MH00144J
- [112] Vallés, C., *et al.*, *The rheological behaviour of concentrated dispersions of graphene oxide*. *Journal of Materials Science* **49**, 18, p. 6311-6320 (2014). www.doi.org/10.1007/s10853-014-8356-3
- [113] Daughton, W.J., *An Investigation of the Thickness Variation of Spun-on Thin Films Commonly Associated with the Semiconductor Industry*. *Journal of The Electrochemical Society* **129**, 1, p. 173 (1982). www.doi.org/10.1149/1.2123749; Spangler, L.L., *et al.*, *Influence of solvent and molecular weight on thickness and surface topography of spin-coated polymer films*. *Polymer Engineering & Science* **30**, 11, p. 644-653 (1990). www.doi.org/10.1002/pen.760301104; Lai, J.H., *An investigation of spin coating of electron resists*. *Polymer Engineering & Science* **19**, 15, p. 1117-1121 (1979). www.doi.org/10.1002/pen.760191509
- [114] Torrisi, L., *et al.*, *Self-supporting graphene oxide films preparation and characterization methods*. *Vacuum* **160**, p. 1-11 (2019). www.doi.org/10.1016/j.vacuum.2018.11.001
- [115] Clauss, A., *et al.*, *Graphitoxyd-Membranen zur Messung des Wasserdampf-Partialdruckes*. *Angewandte Chemie* **68**, 16, p. 522-522 (1956). www.doi.org/10.1002/ange.19560681614

-
- [116] Tsou, C.-H., *et al.*, *Effect of microstructure of graphene oxide fabricated through different self-assembly techniques on 1-butanol dehydration*. *Journal of Membrane Science* **477**, p. 93-100 (2015). www.doi.org/10.1016/j.memsci.2014.12.039
- [117] Salehi-Khojin, A., *et al.*, *Chemical sensors based on randomly stacked graphene flakes*. *Applied Physics Letters* **100**, 3, p. 033111 (2012). www.doi.org/10.1063/1.3676276
- [118] Li, P., *et al.*, *Continuous crystalline graphene papers with gigapascal strength by intercalation modulated plasticization*. *Nature Communications* **11**, 1, p. 2645 (2020). www.doi.org/10.1038/s41467-020-16494-0
- [119] Nagashio, K., *et al.*, *Graphene/Metal Contact*, in *Frontiers of Graphene and Carbon Nanotubes: Devices and Applications*, K. Matsumoto, Springer Japan, p. 53-78 (2015). www.doi.org/10.1007/978-4-431-55372-4_5

Chapter 4

CHARACTERIZATION TECHNIQUES

In the current chapter, the characterisation techniques employed to study prepared GRM thin-films and to investigate their charge transport are discussed.

We adopted a multi-tool and multi-scale approach to characterise chemical, morphological and electrical properties both of starting materials and of the final thin films. Charge transport carrier mechanisms occur on different length scale. In GRM networks, such mechanisms are intimately linked with the chemical and morphological landscape of the 2D sheets, as well as with the sheet-sheet interactions which arise when stacked together. A proper set of experimental methodologies is thus mandatory to acquire knowledge about the nano – the material – and the macro – the real device, where interactions among nano objects play a key role.

Here, the characterization techniques used and the related instrumentation are presented. I pay a lot of care on first two techniques (*i.e.* XPS and AFM) because I have extensively used them during these three years, even for activities not directly linked to this work.

4.1 Chemical Analysis: XPS

Photoelectron spectroscopy (PS) involves the energy analysis of electrons ejected from matter by incident radiation. The technique allows quantitative chemical characterization of surfaces and thin films. It is grounded on the photoelectric effect, which was firstly observed by Hertz [120] and later explained by Einstein, in 1905, through wave-particle duality of electromagnetic radiation [121]. A material exposed to electromagnetic radiation of sufficiently high energy $h\nu$ emits electrons of kinetic energy E_K . The energy balance of the process is expressed by

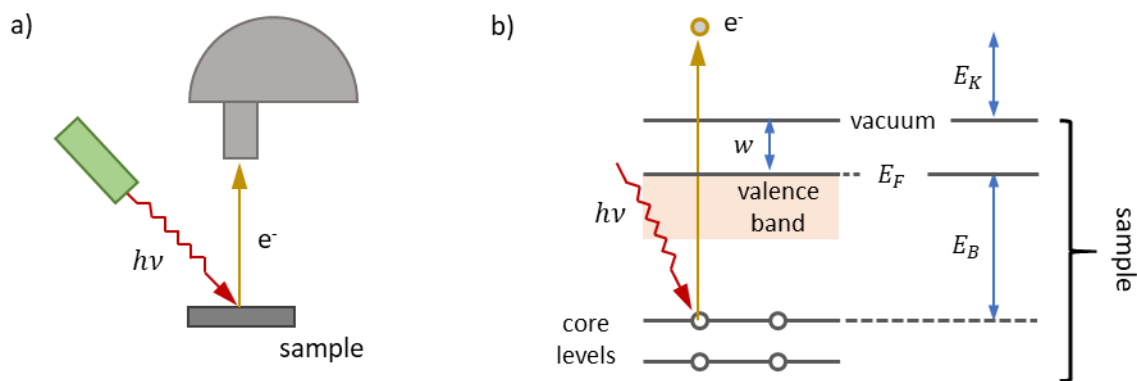


Figure 4-1. (a) Basic principle of photoelectron spectroscopy: incident light of energy $h\nu$ impinges the sample surface and it causes the emission of an electron e^- , that is detected and its kinetic energy analysed. (b) Energy diagram representing the same electron photoemission process of (a). The sample comprises atoms with deep energy core levels and a continuum band of valence energy levels.

$$h\nu = E_B + E_K + w \quad (4-1)$$

where E_B is the binding energy of the electron before emission; and w is the energy difference between the Fermi level and the vacuum, usually referred to as the surface work function in solid-state physic (see Figure 4-1b). The fixed radiation $h\nu$ may excite and cause the emission *-i.e.* ionization- of different levels of electrons, which are related to different atomic states/levels in the material. This leads to different kinetic energies E_K . A PE measurement consists in recording the number of photo-emitted electrons as a function of their kinetic energy and the acquired plot is the photoemitted spectrum. It is also common in literature to present E_B on the abscissa-axis, instead of E_K .

PS permits the study of density of states and valence band structures for ultraviolet radiation (UPS; $h\nu \approx 10 \div 10^2$ eV). On the other hand, core states are mainly associated with the use of soft x-ray radiation (XPS; $0.4 \text{ keV} < h\nu < 3 \text{ keV}$), as expressed by the acronym ESCA (Electron Spectroscopy for Chemical Analysis), a term by which it is also known in materials science. Because the latter is the tool used throughout this work, we only discuss XPS.

Atomic core states are those levels containing electrons not mainly involved in chemical bonding. They show corresponding peaks in the XPS spectrum of the investigated material

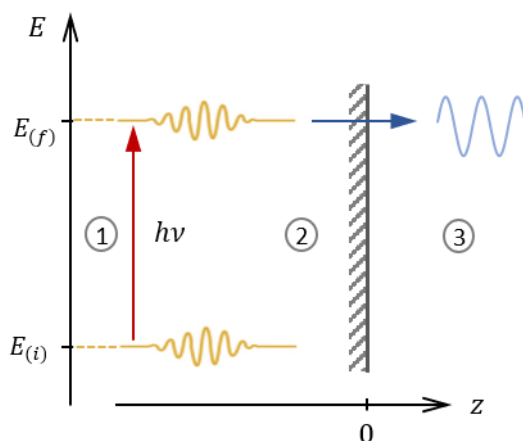


Figure 4-2. Approximated three-step model for the electron photoemission. Energy of electronic states is along the vertical axis, while the spatial coordinates are along the horizontal axis. $z=0$ indicates the interface between the sample ($z < 0$) and the vacuum ($z > 0$). In the first step of the process, (1) the electron is optically excited from initial state $E_{(i)}$ to $E_{(f)}$. Then, (2) it travels to the surface, and finally (3) is transmitted through the surface and emitted into the vacuum.

deriving from those ejected electrons. Since the E_B of an electron in a specific atomic shell is unique for each element, the material composition can be determined. The only exceptions are hydrogen and helium for which the photoionization cross-sections are too low to make the emission possible with lab-scale instrumentation [122,123]. Whereas x-ray radiation can penetrate deeply into a solid, excited electrons undergo inelastic scatterings with other bound electrons and energy losses over short distances. Their probability of escaping from the material decreases exponentially with increasing distance from the surface. Hence, only photoelectrons coming from the first few nanometres escape which explains the surface sensitivity of XPS.

From a theoretical point of view, calculation of the photoemission process must be carried out quantum mechanically by treating the electron excitation and its ejection to the vacuum as a single final state. However, this one-step model poses several computational difficulties and the process is often approximated as three independent steps [124], as schematised in Figure 4-2. In the first step, the absorption of a photon by the material causes the transition of an electron from an initial atomic state to $E_{(i)}$ a final one $E_{B(f)}$. Then, in a second step, the excited electron propagates from the (final) atomic state to the surface. During this phase, the electron could lose an energy ΔE_{loss} with respect to

$E_{(f)}$ through various scattering phenomena. The final step consists of transmission through the surface and electron emission into the vacuum.

Koopmans theorem states that the E_B of a core electron can be approximated by the energy difference between $E_{(i)}$ and $E_{(f)}$, where the orbital re-configuration due to the transition has been neglected (*i.e.*, frozen-structure approximation) [125]:

$$E_B = E_{(f)}(N - 1) - E_{(i)}(N) . \quad (4-2)$$

N is the number of electrons in the atomic system before the photoexcitation. Other than representing the fingerprint of atomic species, core level E_B provide information about the chemical state of the atoms. Indeed, changes in the valence states due to bonding between atoms strongly affect the core levels, even though they do not participate in the chemical bonding. For instance, if we consider an oxidised form of a metal, electron density is partially shifted from the metal atom towards the bonded oxygen, decreasing the effective electronic charge on that atom. This charge reduction causes a higher effective positive potential experienced by the escaping photoelectron and leads to a higher binding energy, shifted in energy ΔE_{shift} with respect to the pure element. The opposite occurs for metal bonding with a reducing element: the effective electronic charge increases and the photoemission shifts to lower binding energies (with respect to the pure metal signal). The effect is the so-called “chemical shift”, ΔE_{shift} , and is usually of the order of few eV.

In addition to structures arising via chemical shift, there is a common electronic fine structure observable in XPS spectra due to spin-orbit coupling. In this case, spin orbit interactions of core holes in degenerate subshells (orbital quantum number $\ell > 0$) produce a splitting of energy levels and a doublet structure can be resolved. If there are no other superimposed signals, the ratio among the areas I of the two peaks in the doublet is

$$I_{\ell-1/2} / I_{\ell+1/2} = \frac{2\ell}{2\ell+2} \quad (4-3)$$

The energy dispersive phenomena previously cited have their origin in multi-electron processes induced by electron correlation. Two typical processes are: “shake-up” and “shake-off”. In the first case, the ejection of a core electron is simultaneously coupled with excitation into higher levels of one or more valence electrons. Therefore, E_K is reduced

and a distinct satellite structure appears, with increased E_B of few eV. In the latter mechanism, instead, the valence electron is directly ejected together with the main core photoelectron. Shake-off appears as a broadening of the core level peak or as a contribution to the inelastic background. These signals are usually very weak and care must be taken in not misinterpreting them as chemical shifts.

Another dispersive mechanism is related to plasmonic losses. A plasmon is a collective oscillation of electrons in the material. These oscillations can of course interact with the photoelectron and cause discrete loss of energy, that will manifest as equally spaced multiple peaks from the primary signal.

By including chemical shift and energy losses terms, eqn. 4-2 can be re-written as

$$E_B = E_{(f)}(N - 1) - E_{(i)}(N) \pm \Delta E_{shift} + \Delta E_{loss} . \quad (4-4)$$

A basic XPS instrument is composed of an ultra-high vacuum (UHV) chamber, an x-ray source and an electron analyser. The instrument present at CNR-ISOF is equipped with a XR50 source and a *Phoibos 100 analyser*, fabricated by SPECS. Its chamber consists of three stages: a high-vacuum load lock chamber, a UHV preparation chamber and a UHV analysis chamber. Each sub-chamber is supplied with a dedicated pumping system. This multi-stage system is needed to keep the pressure as low as possible in the analysis area and permit the collection of photoelectrons. The analysis chamber base pressure after all wall desorption procedures (*i.e.* bake-out) is $5 \cdot 10^{-10}$ mbar.

The preparation chamber includes an ion gun connected with an argon gas line for sample sputtering and a special sample holder, which contains a resistive heater for sample thermal treatments.

The x-ray source mounts a Mg anode, which has its most intense x-ray emission in the $K\alpha$ characteristic line. $K\alpha$ indicates the radiative atomic transition $2p \rightarrow 1s$ following the creation of a $1s$ (or K) excitation by electron impact. The corresponding electromagnetic energy $h\nu$ is 1253.6 eV. The radiation of our instrument is not monochromatized, which means x-ray beam energy is spread around the central value of the transition. This has the counter-effect of little decreasing resolution. The source is operated at a power of 125W and continuously water-cooled. Care is taken in keeping a constant (low) conductivity of the cooling water. On the one hand, it prevents excessive corrosion of source walls; on the other, detrimental electrostatic discharge are avoided.

The analyser is composed of a system of lenses, by the hemispherical electrostatic analyser (HSA), which effectively performs the separation of photoelectrons at different E_K , and by a multichannel detector (Chevron microchannel plate type), which “counts” the electrons. The lens system images the sample plane on the HSA entrance plane, defines the sampled area (*i.e.* spatial resolution) and the accepting solid angle and accelerates/decelerates the electrons to a fixed energy. Only electrons of a given energy E_p (“pass” energy) will be accepted by the analyser and counted. We operated the analyser in a constant energy mode where E_p is held constant. E_p is one of the main factors which influence the energy resolution of the measurement. A lower E_p relates to a better energy resolution, at the expense of the intensity of the signal. Other factors that contribute to the broadening of the signal and to a decrease of resolution are the imperfections in the electron kinetic energy analysis; the intrinsic photoemission line width, due to the lifetime of the specific atomic levels in the process; and the broadening given by exciting x-ray source. In our instrument, we estimated a total spectral resolving power of 0.9 eV for $E_p = 10\text{eV}$, value that we used for high-resolved acquisition. The resolving power is not the only parameter to consider for extracting quantitative information from an XPS measurement: the signal-to-noise (S/N) ratio also plays an important role. S/N represents the peak intensity of a spectrum feature – *i.e.* signal from an atomic species - relative to the noise measured at some point off the peak. A high S/N value for a peak allows to clearly state the presence of the related chemical element. Assuming fixed the spectrometer performance, S/N can be improved by increasing the acceptance time per each energy value of the analyser or by averaging several measurements on the same energy range. Both routes lead to longer measurement times.

In a real measurement, the photoelectron also needs to overcome the work function w_A of the analyser to be detected. Therefore, w_A must be added to the *rhs* of equation 3.2. The problem is that w_A is typically unknown. To get around the issue, the practise is to calibrate the instrument by measuring standard/pure samples with known XPS spectra. The investigated sample spectrum is then referenced to the standard and w_A cancels out. We used the Au 4f_{7/2} signal ($E_B = 84.0\text{eV}$) or the Ag 3d_{5/2} one ($E_B = 368.3\text{eV}$) from freshly Ar⁺ sputtered samples.

Features to be taken care with during measurement are sample charging-related effects. Charging is caused by the difference in rates of electrons which are ejected from the sample and of electrons that arrive on its surface, which are stray electrons coming from the vacuum and/or electrons from the ground conducted through the bulk of the sample. In insulators and poor semiconductors, such as some GRM networks, this difference can be of several eV and not homogenous across their surface. The induced surface potential V_S increases the amount of energy required to emit the photoelectron and, in turn, influences apparent binding energies, leading to shift and broadening of PE signals. A simple way to limit surface charge formation is to electrically connect the surface with a metallic piece of the holder. Applying a bias potential to the sample is also effective in charge neutralisation, but V_S is often undetermined and several trials should be performed before full spectrum acquisition.

To analyse an XPS spectrum, the line-shape and the background of an atomic signal (peak) must be correctly assigned. The line-shape of the measured peak depends both on the intrinsic properties of the photoemission process and on the experimental conditions of the detection system, such as angular acceptance and energy resolution. The intrinsic contribution alone would produce a Lorentzian shape if the analysing process did not add Gaussian terms. Therefore, the measured peak is a convolution of the two functionalities. In peak fitting, a more flexible lineshape with a modified Lorentzian is often employed to force a finite area integral [126].

Inelastic processes always contribute to the formation of a broad signal, *i.e.* the background, superimposed over well-defined peaks. Simple ways to model backgrounds are to use a linear interpolation between the intensities at the limits of a defined energy range or using the Shirley function [127]. This last method considers the background contribution to be proportional to the intrinsic spectrum integrated over all signal energy range. An alternative procedure is the one of Tougaard [128]. In this case, the algorithm uses a phenomenological or experimental loss function to calculate the signal. The obtained background has a physical shape, but only expected loss phenomena must be accounted for.

We used XPS to quantify the chemical composition of GRMs and GRM networks. To a first approximation, the number of emitted electrons I at energy E_K is directly proportional to

the atomic concentration N_i of a specific element i . The dependence of I on material and instrument properties can be expressed by relation 4-5 [129].

$$I(E_K; s) = N_i \cdot J(h\nu) \cdot \sigma_i(h\nu, \theta; s) \cdot \lambda_I(E_K) \cdot T_f(E_K, E_P) \quad (4-5)$$

J is the x-ray flux; σ_i is the photoemission cross-section for the atomic transition s ; λ is the inelastic mean free path of emitted electrons; T_f is the transmission function of the analyser; and θ is the angle between the x-ray beam and the analyser.

If source parameters and sample-source distance do not change during a measurement and spurious anode discharges do not occur, J is, in turn, fixed.

σ_i is estimated by first principle quantum mechanical computation. It can be decomposed in two factors: one considering only the probability of photoemission (photoionization cross-section [122]), independently from the process geometrical configuration; and one linked to the angular dependency (asymmetry function), which tends to 1 at the magic angle θ of 54.7°.

λ_I is a parameter which quantifies the amount of photoelectron interactions with material atoms and it defines the surface sensitivity of the technique. It is the mean distance a photoelectron travels without undergoing a collision (*i.e.* inelastic mean free path). A quasi-universal empirical dependence was observed for a broad range of elements [130]. Thus, to the first order, λ_I is computed based only on the energy of the electron and not on the specific element.

T_f embodies the probability that photoelectrons are collected by the lens system, go through the HSA and reach the detector. The observed intensity distribution I will differ somewhat from the true distribution because of the presence of T_f .

The last three contributions are usually calculated for each instrument configuration and for each detectable atomic transition. They are expressed as unique parameters, called relative sensitivity factors (RSF), reported by the spectrometer manufacturer.

$$RSF_s = \sigma_i(h\nu, \theta; s) \cdot \lambda_I \cdot T(E_P) \quad (4-6)$$

The usual method for obtaining the oxygen to carbon (O/C) atomic ratio in GRM consists in computing the ratio of the intensities of O 1s and C 1s XPS signals, as in eqn. 4-7. The RSF of C 1s is taken as being equal to 1 as reference, while the RSF of O 1s is 2.85 in our experimental condition.

$$(O/C)_{area} = \frac{I_{O\ 1s}}{I_{C\ 1s}} \cdot \frac{RSF_{C\ 1s}}{RSF_{O\ 1s}} \quad (4-7)$$

The intensity I_s expresses the integral over all E_K contributing to transition s , *i.e.* the area. However, this method does not supply any information on the chemical functionalities and is prone to inaccuracies if other oxygen signals are present. Hence, we employed another fitting protocol developed by A. Kovtun *et al* [131] and used the value obtained from eqn. 4-7 as validation. This second method is based on the deconvolution of a highly-resolved C 1s signal into its various contributions. For RGO, for example, the components are graphitic carbon (C sp², B.E.=284.5 eV), sp³ carbons (B.E.=285.1 eV), and carbons bonded to hydroxyl (C-OH, B.E.=285.7 eV) and epoxy groups (C-O-C, B.E.=286.7 eV), and those from carbonyl (C=O, B.E.=288.0 eV) and carboxyl (O-C=O, B.E.=289.1 eV) groups [16]. The expression for the calculation of a GRM O/C ratio using the new protocol is shown in eqn.4-8.

$$(O/C)_{fit} = \frac{I_{C\ 1s}^{(C-OH)} + I_{C\ 1s}^{(C=O)} + \frac{1}{2}I_{C\ 1s}^{(C-O-C)} + 2 \cdot I_{C\ 1s}^{(O-C=O)}}{I_{C\ 1s}} \quad (4-8)$$

A novel aspect of the protocol is the use of an asymmetric pseudo-Voigt line-shape for the C sp² signal which accounts for the semi-metallic nature of this allotrope of carbon. A reliable estimation of the amount of C sp² in the GRM is thus possible. C sp² is a parameter that can be used to characterize GRM [131] and it plays an important role in defining their charge transport phenomenology [34].

4.2 Morphology

Atomic Force Microscopy (AFM)

Atomic Force Microscopy (AFM) is a wide-spread scientific tool which provides information on the nanoscale, and even beyond. An AFM image is constructed by probing the forces felt by a solid sharp tip while it is scanning the sample surface. Based on the tip characteristics and the way it is made to interact with the sample, different signals can be retrieved from the studied surface/nanostructures: morphological, mechanical, electrical, magnetic, electro-chemical, etc.. In principle, any material can be imaged – hard or soft, insulating or conducting. The typical range of these images is hundreds of nanometres

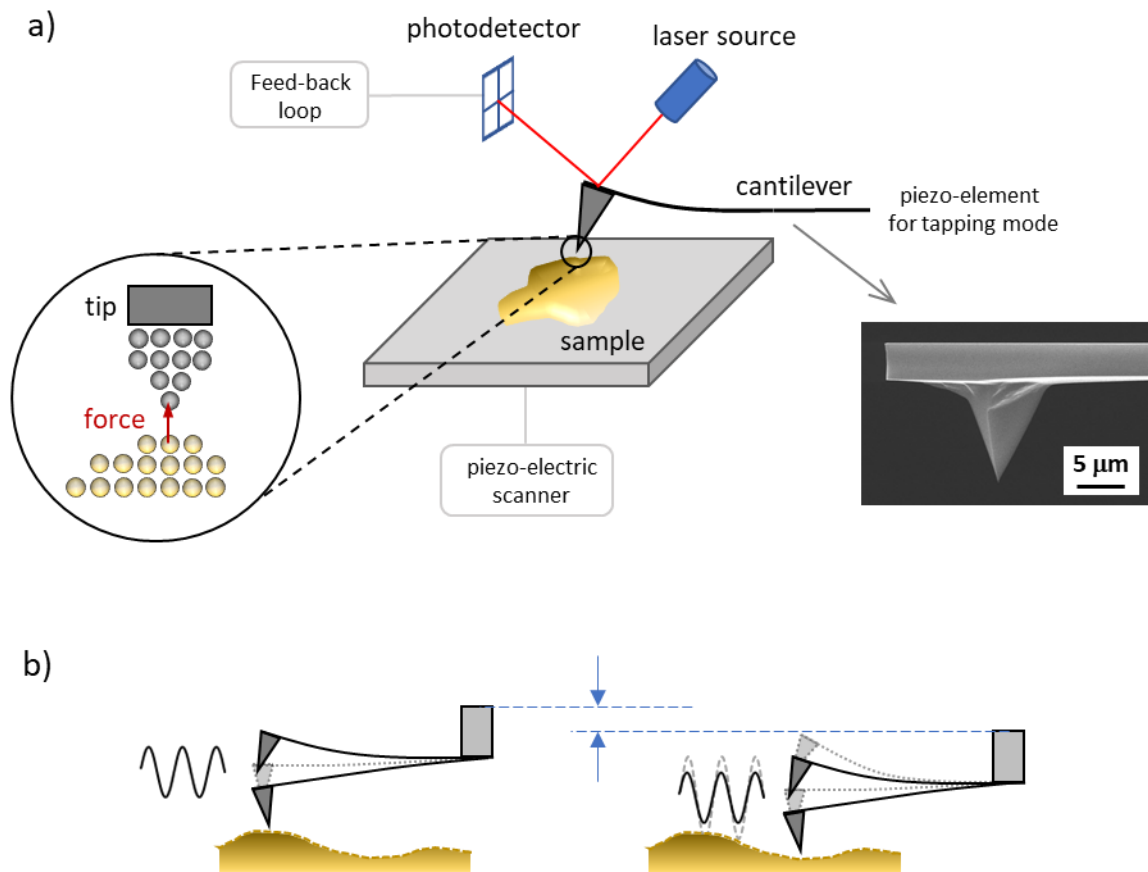


Figure 4-3. (a) A scheme of a typical AFM set-up. The imaging mechanism relies on the interaction occurring between a sharp tip and the sample structure. On the right corner, an electronic micrograph (SEM) of the tip used for topographic imaging.

(b) A sketch of “tapping” imaging mode: the change in sample-tip interaction due to a topography variation is met by a change in the applied potential to the cantilever to keep the amplitude constant.

vertically with sub-nanometre height resolution and several tens of micrometres laterally, up to $\sim 100 \mu\text{m}$, with a highest (physical) lateral resolution of only a few nm.

Measuring interatomic forces is a key part of the technique. They can be repulsive (short range order, 10^{-1} nm) or attractive (long range order, $10^0 \text{ nm} \div 10^1 \text{ nm}$). The attractive Van der Waals forces have different origins: dipole-dipole interaction, dipole-induced dipole interaction and induced dipole-induced dipole interaction. Repulsive forces are instead due to the Pauli exclusion principle which forbids electrons with the same quantum numbers to share the same region of space. Quantum mechanics plays a major role in the technique. If we consider the apex atom/molecule of an ultra-sharp tip and an

atom/molecule on the sample surface, the interaction can be described by the Lennard-Jones potential [132]:

$$V(z) = -\frac{A}{z^6} + \frac{B}{z^{12}}, \quad (4-9)$$

z is the distance between the two atoms/molecules; A and B are empirical parameters. For large z , the potential is negligible. At a certain distance, V starts to decrease (attractive region) until it reaches a minimum at z_0 , which represents the equilibrium distance of the two-particle system. On further decreasing z , V will increase and atoms will repel each other.

A typical AFM instrument is formed by a flexible cantilever with an end fixed and the other free to move, to which the tip is attached (see Figure 4-3a). Measurable forces range from 10^{-12} N to 10^{-6} N according to the cantilever stiffness. The sample is mounted on a stage under the tip. A piezoelectric device is used to move in the three spatial directions - x , y and z - either the sample stage relative to the tip or the tip relative to the sample. An area of the sample is scanned in x and y by moving the sample relative to the tip (or vice versa). The relative motion occurs from one side to the other along the points of a line, *i.e.* fast scanning direction, and repeating this for multiple lines along the perpendicular direction, *i.e.* slow scanning direction. At each point the interatomic force between the tip and the sample causes a deflection $\Delta z (= z_0 - z)$ of the cantilever, which is modelled to a first approximation as a driven harmonic oscillator. The cantilever deflection is usually measured by a laser system. The light emitted by the laser is reflected on the top part of the cantilever and its intensity is collected by a screen (*i.e.* photodetector). If the cantilever changes its free force position z_0 , the light will hit the screen at a different point. The signal coming from the photodetector is related to the morphology - or to another physical quantity - of the sample and it is used to form its surface image. When a feedback loop is present in the instrument, the photodetector signal is compared with a set point value. If differences occur, a counter signal is applied to the tip-sample to restore the set point value. This counter signal is then used to form a calibrated image. The simple way of performing a measurement requires the tip to be as close as possible to the sampled structure at each point, *i.e.* in contact. The meaning of "contact" is that tip-sample interactions lie in the repulsive part of potential curve in eqn. 4-9.

A slightly more complex, but typical class of AFM operating modes is intermittent contact. In this class, “tapping mode” (with amplitude modulation, as illustrated in Fig. 4-3b) is probably the most widely used among AFM users. Conversely to contact mode, the cantilever is forced to oscillate during the scanning. This is allowed by an additional piezo-electric device mounted on the cantilever. The chosen oscillation frequency is often a value slightly less than the cantilever natural frequency for accounting tip-sample engagement related shifts. The natural frequency depends on the sizes and the shape of the probe assembly (cantilever plus tip). Tip-sample interactions cause a change in the oscillation frequency and, hence, in the oscillation amplitude. At each imaging point, measured amplitude is compared with a set point value by the feedback loop. If an amplitude change occurs, a correction voltage is applied to the additional piezo-electric device in order to adjust the amplitude and track surface topography. The amplitude set-point is chosen considering the imaging goals, the tip wear and the sample surface. The set-point is related to the free (*i.e.* far from sample) amplitude and indicates how much the amplitude can vary before the feedback comes into play. Hence, a lower set-point means a greater tip–sample interaction force. In intermittent contact, the tip experiences alternating repulsive and attracting forces. The smaller time of interaction with the sample favours a slower degradation of the tip, minimum contribution from lateral forces, less damage to the sample and a lower probability of dragging particles with respect to an approach where the tip is always in contact with the sample. The latter are points of high concern when studying GRM deposited on – *i.e.* weakly adhering to - a substrate, instead of film structures. On the other hand, the cantilever response to large topographic changes is slower than contact mode and scanning may need to proceed at a slower rate.

AFM images are subjected to a series of artefacts. Some of them can be digitally corrected and image post-processing is often needed to improve the readability of data. Piezo-electric scanners are one of the main sources of artefacts. Among them, there are “scanner bow”, edge z-overshoot and scanner creep. The first effect occurs in tube piezoelectric devices fixed at one end of the microscope structure when the sample is scanned over relatively high dimensions (several μm). It manifests itself as a curvature, or “bow”, in z along the fast-scanning direction. Edge overshoots are caused by z-axis hysteresis in the piezoelectric ceramic material and, as the name suggests, step profiles

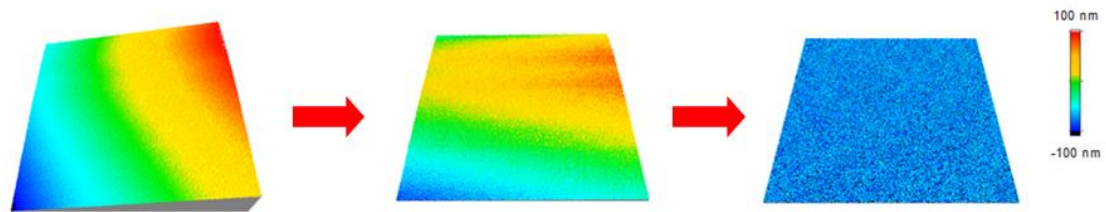
are not traced accurately with lower/higher z-values at the edges. Creeps instead verify when the response of the piezo material does not follow exactly the applied voltage. This produces distortions in the image, as if the sample is drifting. Possible solutions include waiting for the piezo response to stabilize or re-applying the voltage, practically re-starting the scanning from the initial position. Non-linearity in the piezo movements could also produce incorrectly wrong measured distances, however a proper calibration of the scanner sensors – if present – can prevent this. Other typical artefacts are related to the conditions of the tip, which can be damaged or contaminated during scanning and/or be too large (*i.e.* blunt tip) to correctly follow the features of an object. As a consequence, the image could show strangely shaped objects, repeating patterns and too small cavities. The formation of double (or multiple) tips at the tip apex is an example of probe damage that causes the appearance of double (or multiple) copies slightly shifted from each other in the image. Unfortunately, tip-related artefacts cannot be corrected digitally and, even if some tip cleaning procedures exist, the simplest solution is replacing the probe.

Artefacts present as regular oscillations in the image are generally linked with noise phenomena, caused either by mechanical vibrations in the environment (building, acoustic, lab-instruments connected vibrations...) or by faulty electronics in the microscope. Also, an improper choice of feedback parameters and scanning rate causes asymmetrically enlarged shapes or high-frequency oscillations.

Artefacts due to the z-height of the piezoelectric scanner are corrected by carefully subtracting averaged and line-by-line polynomials to the raw image, while filtering out the nano-objects from the operation (*i.e.* flattening procedure). We used SiO₂, either native or thermal wet growth, as standard ultraflat substrate (surface roughness <0.4 nm). The flattening procedure is monitored by histogram analysis, as shown in Figure 4-4 [133].

We utilized two commercial AFM instruments: a Bruker *Multimode 8* and an NT-MDT *Ntegra-I*. Both instruments integrate a tube scanner placed under the sample stage and a laser/photodetector measuring system. The two are also mounted on a gas-damped bench and on a mechanically damped stage, respectively, to isolate them from the lab environment and prevent vibrations. We operated them in intermittent contact to obtain information about GRM sheet morphology and about the fabricated films. We mainly

AFM image (3D visualisation)



Height histogram

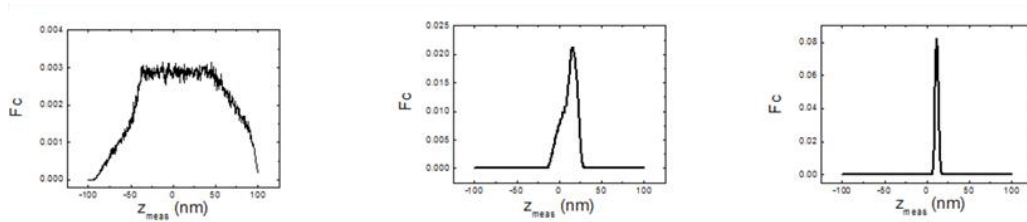


Figure 4-4. Summary of the flattening procedure for AFM images. Three AFM images with corresponding height histogram below are presented by increasing data processing, from left to right. The left image is the raw data, while the right image represents the real, flat substrate after polynomials subtraction. Image adapted from ref. [133].

used a rectangular Si cantilever with quite a high force constant k (RTESPA-300, Bruker, $k=40\text{N/m}$, $\omega=300\text{kHz}$).

The image processing was performed with the *SPIP* suite (version 6, *Image Metrology*). The “particle analysis” tool was employed for obtaining information on a statistically relevant set of GRM sheets. We applied filters on quantities such as mean z , area, and geometric shape to sort out the unwanted objects in the images. We followed a combination of the protocols for studying 2D particles reported in the works of Liscio, *et al* [108] and of the NPL institute [134]. Due to their fragmented nature, 2D GRM sheets commonly have wide shape distributions. A wide and thin (on the plane) particle can have a comparable length with a round, shaped particle but with a fragmented perimeter. Hence, the length or lateral size directly measured on the object cannot be a reliable parameter for describing sheet population. Conversely, we analysed the area of each object and the associated size was computed as the square root of the object area.

Optical Microscopy

Standard optical microscopy (OM) using visible light as the illuminating source is a fast and reliable technique to investigate the morphology of a sample from millimetric dimensions down to several micrometres. The working principle of OM is based on a system of physical lenses which focus and collect the light reflected or transmitted by the sample, providing an enlarged view of it. In typical lab instruments, the magnified sample image can be formed on human retina, through eyepieces, or saved digitally via a digital camera.

In this work, we employed a Nikon *Eclipse 80i* optical microscope operating in reflection mode for a fast morphological characterisation of fabricated GRM thin films. The microscope is equipped with a high-pressure light source, a digital colour camera (Nikon Coolpix 5400) and a set of suitable objective lenses (4x, 10x, 20x and 40x).

Electron Microscopy

High energy (keV) accelerated electrons are a fantastic tool for analysing condensed matter because they produce a wide range of signals from the sample, such as different kinds of electrons, x-rays or UV radiation. Overall, electron-based microscopic techniques do not suffer of the visible-light diffraction limit and can be employed to obtain material information at high spatial ($\leq \mu\text{m}$) and analytical resolution [135].

In scanning electron microscopy (SEM), a focused electron beam is rastered over the sample surface. An image of the sample is composed by combining the acquired signal at each point during the scan.

A typical instrument can be divided into three parts: beam production, beam-sample interaction and collection of the signals. The beam is usually generated by a thermionic gun or by a field-emission gun, operating under ultra-high vacuum conditions. In the first type, a W filament (or a LaB₆ crystal bonded to a metal wire) is heated by passing a current to reach temperatures where electrons overcome material work functions and are emitted by the thermionic effect. The electrons are then accelerated by a positive high voltage at the anode. A third element, named Wehnelt cylinder, is interposed between the filament and the anode and works as a small electrostatic lens. In the field emission gun, instead, electrons in the cathode tip tunnel the energy barrier thanks to a voltage

applied between it and a first anode. Then, electrons are accelerated to the desired kinetic energy by a second anode.

The beam produced travels through a set of alignment coils and magnetic lenses, before entering into the scan coil. The function of this coil is to deflect the beam over different points of sample surface. The scan coil controls the size of the analysed area and thus controls the magnification. Finally, the beam goes through the objective lens which focuses it. The beam size at the sample surface determines the minimum spatial resolution of the technique. One of the main signals, which is detected in a SEM, is related to secondary electrons. Secondary electrons are electrons that have undergone inelastic scattering with the incident electrons of the beam and gained enough energy to be ejected from the sample atoms. They give information about the topography of the sample and, in some cases, even about its composition. The secondary e^- detector is located next to (or in-line with) the objective lens and consists of a scintillator connected to a photomultiplier. Because secondary e^- have low kinetic energy, an accelerating voltage is usually applied before the scintillator to aid electron collection.

Two SEMs were utilized in this thesis, both installed at CNR-IMM laboratories in Bologna. A *Gemini 1530* with a field-emission gun and an *EVO LS 10* with a LaB_6 thermionic source, both manufactured by Zeiss. The *EVO LS10* can be operated at variable column pressure for analysis of poorly-conducting surfaces.

For isolated GRM sheet observation, we worked at low beam energy (<5 keV) and small working distance in order to optimise the image contrast and to increase spatial resolution.

Raman Spectroscopy

Raman spectroscopy is a technique used to probe vibrational and rotational modes in molecular systems. It relies on monochromatic light inelastically scattered by atomic vibrations, *i.e.* phonons. The scattered light has a shift of energy ΔE with respect to the incident light. By acquiring the scattered light and plotting ΔE intensities for each value of energy, information about the molecular structure of the sample can be revealed. It is customary to plot the quantity $1/\Delta\lambda$ expressed in cm^{-1} , instead of ΔE , by exploiting the relationship $\Delta E = hc/\Delta\lambda$, where h is Planck's constant, c is the speed of light and $\Delta\lambda$ the difference between incoming and scattered light wavelengths.

In single layer graphene, the G peak at about 1580cm^{-1} is related to photons elastically scattered by C=C in-plane stretching vibrations and is a fingerprint of aromatic graphene-like structures. The D peak at about 1340cm^{-1} is instead related to the six-membered ring breathing mode. In this case, photon-excited electrons are inelastically scattered by optical phonons between two different graphene energy valleys. The dispersive nature of the interaction causes a variation in the D position with respect to the excitation wavelength. The D peak is absent for pure, crystalline graphene and evolves with the introduction of defects, independently of their nature (chemical and/or topological) [136]. This kind of scattering can also occur in the same energy valley, producing the D' at around 1650 cm^{-1} .

For GRMs and multilayer graphene, another set of peaks are added to the Raman spectra of single layer graphene. They are caused by relative vibrations of the different planes, either perpendicular or parallel to their normal [137].

The ratio I_D/I_G of D and G peak intensities is used to estimate defect content. Unfortunately, Raman spectroscopy cannot give a reliable quantification of defect content in GRM systems for values greater than $\sim 3\%$ [138]. Indeed, I_D/I_G ends its monotonical increase above that value. Even when the defect nature is fully known, the average size of defective regions competes with the number of defects in producing the D peak. It is still not clear how to disentangle the two components in Raman spectra and further, complementary data are needed.

In this work, a *InVia Qontor* Raman instrument (of *Renishaw*) located in CNR-IMM labs of Tor Vergata (Rome) was used. The instrument is equipped with a confocal optical microscope and a high resolution *Andor* CCD camera. Raman spectra were collected with a $100\times$ objective (NA = 0.85) by employing a 532 nm excitation wavelength. The spot size was around $1\ \mu\text{m}$. This set-up allowed the acquisition of signals from specific areas of isolated and overlapped RGO sheets.

X-ray Diffraction (XRD)

Soft x-ray radiation with energies of few keV has a wavelength in the sub-nm range and, as a consequence, it can be exploited as a probe for resolving atomic structures. In fact, x-ray diffraction (XRD) measurements have been used for decades for non-destructive

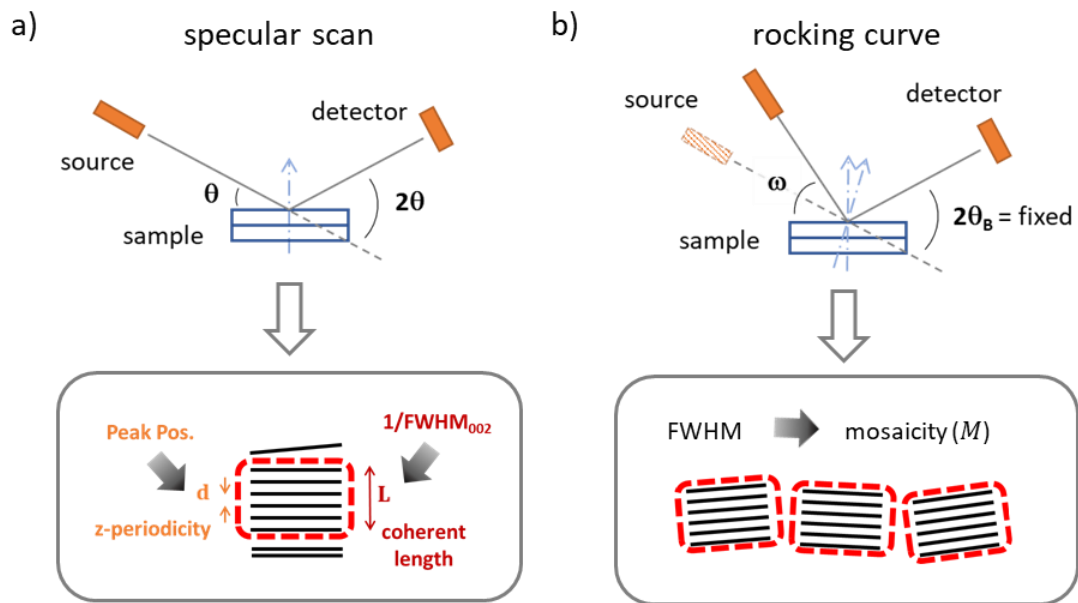


Figure 4-5. Scheme of XRD measurement configuration for (a) specular scan and for (b) rocking curve. In the bottom, the obtainable parameters from each kind of measurement are defined.

structural characterization of matter, from molecules to large polycrystalline alloys. The basic principle of x-ray diffraction is the coherent elastic scattering of radiation from ordered lattice planes in a crystal, which obeys Bragg's law [139]:

$$2d \sin(\theta_B) = n\lambda \quad , \quad (4-10)$$

where θ_B and λ are respectively the incident angle and the wavelength of the incoming electromagnetic wave, while d is the interplanar spacing between lattice planes with the same crystallographic orientation.

Two types of diffraction measurements were performed: a specular or θ - 2θ scan and rocking curves. In the case of thin film on a substrate, both analyses provide information along the surface normal, *i.e.* along the z direction.

In a specular scan, the scattering vector is kept parallel to the film surface normal. This causes that the angle of incident radiation and the angle of (collected) scattered radiation, θ and 2θ respectively, to be coupled. Both angles are relative to the film surface. Diffraction occurs and a peak appears in the spectrum when the lattice planes in the sample are parallel to the scattering vector. Following eqn.4-10, the peak position probes d .

Furthermore, the FWHM of the diffracted peak ($\Delta 2\theta_B$) is correlated with the coherence length L along the z - direction by the Warren-Scherrer formula [140]

$$L = \frac{K \cdot \lambda}{\Delta 2\theta_B \cdot \cos(\theta_B)}, \quad (4-11)$$

where K is a constant, generally equal to 0.9 for carbon structures, and θ_B is the angle at which Bragg reflection occurs. L can be viewed as the mean thickness (z -size) of crystalline domains in the sample. Indeed, a crystalline domain is composed of ordered lattice planes that do not disrupt the coherence of the x-ray beam.

In rocking curves, the crystalline domains misorientations with respect to z of a particular Bragg reflection are investigated. To do so, the detector is kept fixed at the chosen θ_B while the angle of the incident beam – called ω this time – is varied. The parameter which quantifies domains misorientation is the mosaicity M (or mosaic spread), given directly by the FWHM of the obtained peak. A schematization of the two XRD techniques is depicted in Figure 4-5.

A Rigaku *SmartLab* x-ray diffractometer, in the CNR-IMM labs in Bologna, was utilized for these ex-situ structural characterizations. We kindly thank Dott. F. Liscio for performing the measurements and for the assistance in the interpretation of XRD data.

The main parts of the diffractometer are an x-ray source with incident optics, a sample stage able to move in the x - y plane and a receiving system to detect the diffracted signal. Everything is mounted on a mechanical goniometer with 2 rotational degrees of freedom. X-rays are emitted by a rotating copper anode ($K\text{-}\alpha$: $\lambda = 1.54184 \text{ \AA}$) through the inverse photoelectric effect. Thermionic electrons are ejected at a tungsten cathode filament and accelerated towards the anode, which emits the radiation. Compared to the static version, the rotating anode disperses the heat of the incoming cathodic beam and enables long scans at high intensity. The incident optics is characterized by a paraboloidal synthetic multilayer mirror coupled with a germanium channel-cut crystal, which monochromatizes the emitted x-ray radiation and collimates it into a parallel beam before passing through a width-limiting slit, which restricts the width of the sample area irradiated by the x-rays. The receiving optics has another Ge channel-cut crystal (analyser), a receiving soller slit and the detector. A soller slit consists of a set of metal foils placed at constant intervals in the light path. Its function is to suppress the divergence of the x-ray beam. Indeed, it

determines the scattered beam angular resolution by extracting only the x-rays parallel to the gaps between the metal foils. In the used diffractometer the soller slit is designed to be inserted vertically or horizontally. The detector is a scintillation counter and is positioned on the receiving arm of the diffractometer, with possible motion along the x-y and z axes.

4.3 Electrical Characterisation

Electrical Resistance Measurements

Electrical resistance measurements of all samples were performed on two main set-ups: a Hall station of MMR Technologies for common electrical characterizations and a Physical Property Measurement System (PPMS) of Quantum Design, a multi-measurements system with accurate thermal control (down to 2K and beyond).

The Hall station is made of an assembly with 4 spring-loaded tip probes in a square configuration, shown in Fig. 4-6a, and a controller. The latter includes all the electronic components for biasing the sample and performing the measurements. The assembly and the controller are wired through 4 triaxial connectors, one for each probe. The sample is placed in the assembly under the probes and the electrical connection is obtained by simple contact of the tips on the sample surface. Tips at different distances are available. The station allows easy measurements of the electrical resistance of a sample in the Van der Pauw scheme [141]. According to this scheme, the resistance R is computed with the following formula:

$$R = F \frac{\pi}{2 \ln 2} \cdot (R_{12,34} + R_{23,41}) \quad (4-12)$$

where

$$R_{ij,kl} = \frac{V_{kl} - V_{lk}}{I_{ij} - I_{ji}} \quad (4-13)$$

V_{kl} is the voltage measured from probe k to probe l while a current I_{ij} is applied from probe i to probe j. Each index represents one of the four probes. Thus, R is the combination of 4 electrical measurements. The different measurement configurations are presented in Fig. 4-6b. In eqn.4-12, F is a form factor which quantifies electrical

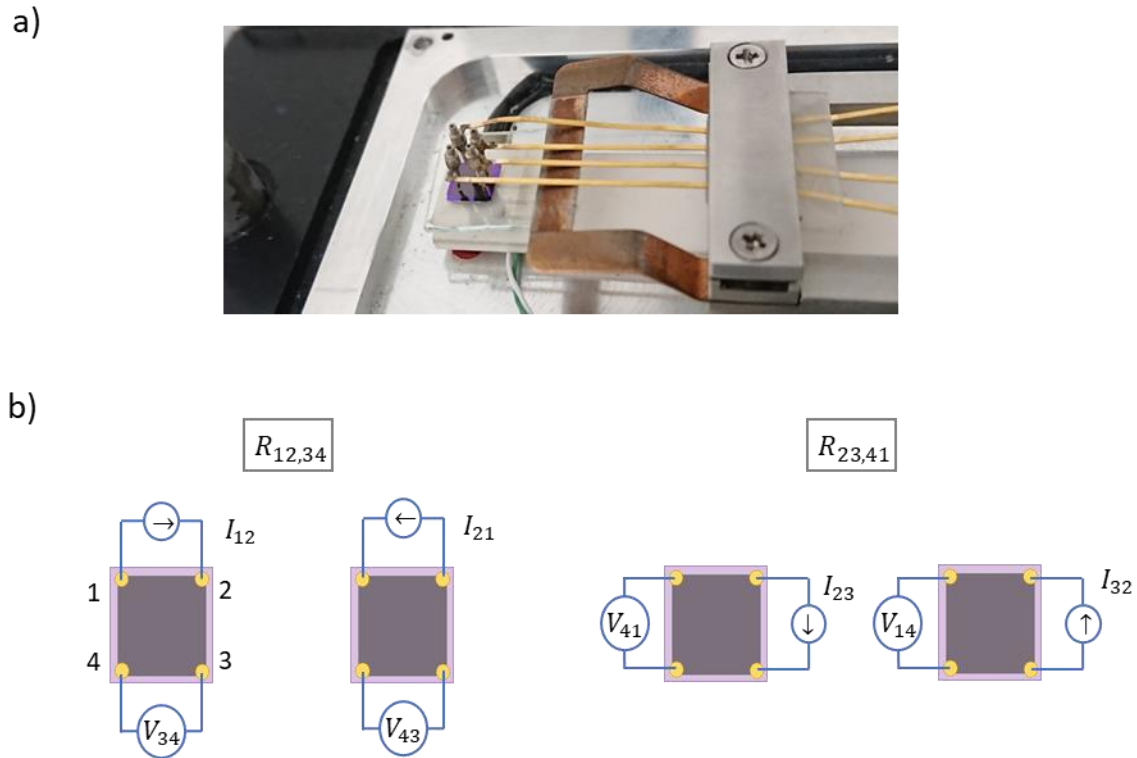


Figure 4-6. (a) Photograph of the Hall station probe assembly. A sample is placed below the 4 tip probes. Sample-probes electrical contact is achieved by lowering the reddish metal clip. (b) The electrical measurements performed in 4-probe Van der Pauw scheme.

asymmetries in the sample and is equal to 1 for $R_{12,34}=R_{23,41}$. We computed F by numerically solving the Van De Pauw equation [141] with the Newton method. An important requirement for the validity of the method is that the sample surface between electrodes was simply connected. The advantage of a 4-probe with respect to a 2-probe measurement lies in the fact that energy barriers connected to contact resistances are ruled out. Resistance in the range from $10^{-2} \Omega$ to $10^{10} \Omega$ can be accessed with this Hall station. The assembly could operate in low vacuum and down to liquid nitrogen temperature, but we only used it at standard temperature and pressure for our preliminary characterizations.

Electrical measurements as a function of temperature, on the other hand, were made with the PPMS. The PPMS is basically a large cryostat equipped with a 7 T superconducting magnet and with dedicated electronics for different measurement routines. Its main

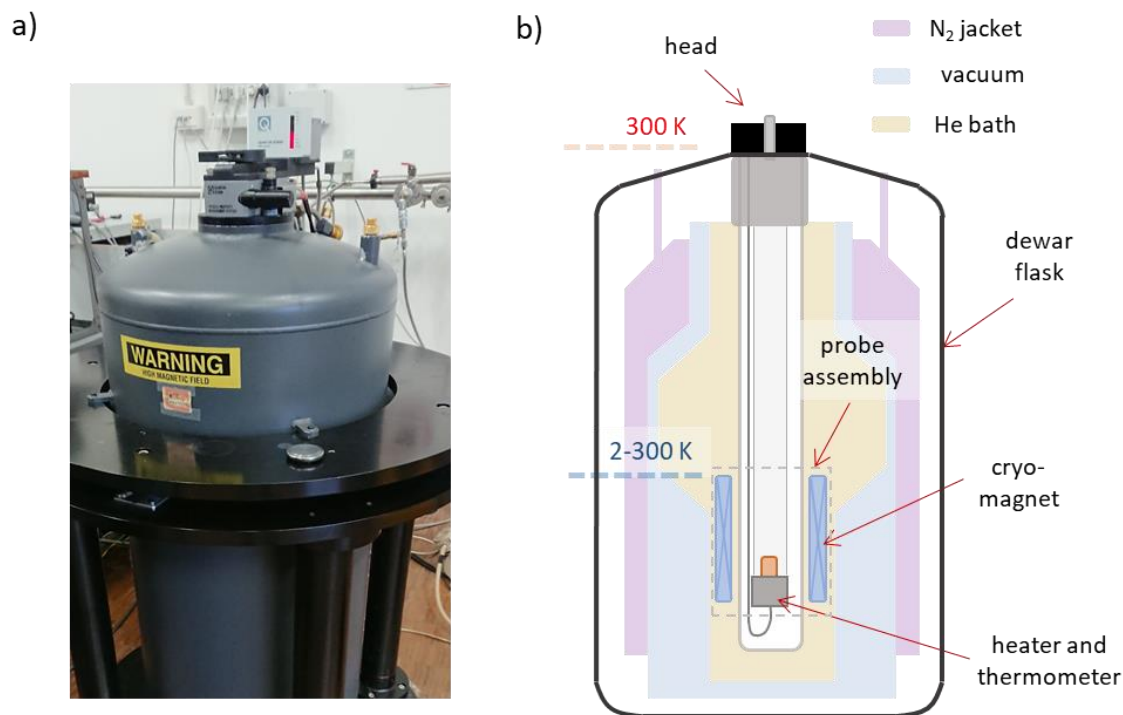


Figure 4-7. (a) Digital photograph of the PPMS dark grey Dewar flask. (b) Simplified scheme of the PPMS flask with the layered structure coloured for clarity.

components are the Dewar flask, the measurement/probe assembly and the electronics cabinet.

The Dewar flask isolates the sample from the environment. A digital photograph and a simple scheme of it are shown in Figure 4-7. The flask contains the liquid helium bath in which the probe is immersed. A layer filled of liquid nitrogen and one with vacuum are interposed between the flask external wall and the helium bath. The flask external walls are made of a special aluminium alloy which favours insulation. A reflective coating, named super-insulation, is also employed to prevent heat absorption by the helium bath. This layered structure guarantees lower energy consumption and higher cooling efficiency, especially at extremely low temperatures.

The probe assembly includes all the controls and sensors needed for the measurements, as well as the sample holder (puck) and the superconducting magnet. It also incorporates a gas line for purging purposes. The assembly is composed of several concentric stainless-steel tubes which isolate the different parts. The inner part, included in two vacuum tubes, constitutes the sample chamber and it is made of copper, in order to favour a region of uniform temperature. The sample puck is located at the bottom of chamber. A

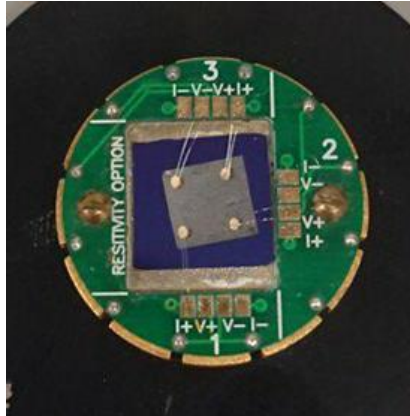


Figure 4-8. Photograph of the sample holder, named puck, used for electrical measurements with the PPMS. It is a version particularly designed for resistivity measurements (“resistivity option” of Quantum Design PPMS). The 12 gold-plated pads, divided in groups of 4, are visible on the green insulating cover. A GRM self-standing membrane (grey square) on SiO_2 (violet region) is wire bonded to some of the pads.

thermometer and a heating coil are placed underneath. Their proximity to the copper puck helps to ensure good thermal contact during the experiments. The thermometer is composed of a platinum resistance, with a working range between 80 K and 400 K, and by a negative temperature coefficient thermistor, which supplies reading between 1.9 K and 100 K.

To warm and cool the sample, helium is allowed to flow in a controlled way into a region between the sample chamber and the inner vacuum tube. The wiring for the sample puck runs up to the probe head. The puck used in this work, which is shown in Figure 4-8, is specially designed for electrical measurements. It has 12 gold-plated pads, which surround the area for sample positioning (*i.e.* puck base). Electrical connections can be created by soldering or wire bonding the pads with the sample. In our configuration, the pads electrical signals are directly extracted through a gray lemo connector cable and decomposed in the 12 independent pad connections (plus one for a common ground) via a custom-made circuit.

While electrical insulation between the sample and the conductive puck base is required, thermal connection is also desired in electrical characterizations to guarantee a correct reading of sample temperature by the thermometer underneath. Hence, the use of quartz or glass as substrates with thicknesses above hundreds of μm does not allow a proper thermalization of the sample and should be avoided completely, if possible.

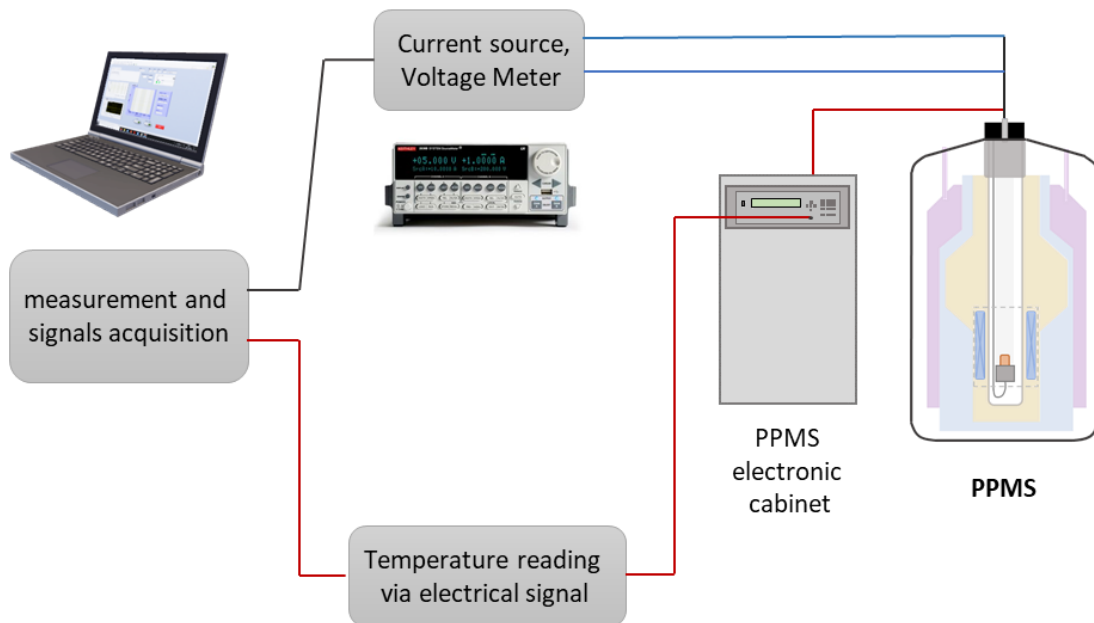


Figure 4-9. Scheme of the $\rho(T)$ characterization using the Physical Property Measurement System (PPMS) and a “home-coded” acquisition software.

4-probe, $\rho(T)$ measurements were performed following the scheme of Figure 4-9 by connecting an external Keithley 2636 Source-Meter to the PPMS sample holder. The use of an external current generator and electrometer guarantees greater flexibility in current-voltage ranges with respect to the internal PPMS resistivity bridge. In particular, the Keithley 2636 can achieve sub-pA current sensitivity while being capable to source DC voltages up to 200 V. The temperature was directly read from the PPMS sensor. The sample was kept at a few mbar under helium exchange gas during the whole experiment. We performed all acquisition and control routines either by a “home-coded” acquisition software or by the *Multivu* software suite of PPMS.

Before $R(T)$ data acquisition, we measured current-voltage (I - V) curve for each sample to determine the linear response (*i.e.* ohmic) region. Then, the injected current was set to a fixed value, properly chosen to avoid non-ohmic behaviour on one hand and to guarantee enough decimal digits in the measured voltage drop across the sample on the other.

We carried out the $R(T)$ measurements by scanning the temperature at a constant rate, from a maximum value to a minimum value and vice versa. We stress that with this system

we must perform one of the two configurations each time and physically reconnect the cables to switch to the other, after having acquired a full range $R(T)$ curve. We usually first performed a fast cycle at 5 K/min of cooling and successive heating. The aim was to let the sample structure absorb the “thermal (cooling) shock” and recover. Successive cooling and heating scans were instead performed at 1 K/min. Most of the time, the faster rate curves present only some limited resistance variations with respect to the slower rate curve.

Resistivity ρ was calculated for each temperature point according to

$$\rho(T) = t \cdot R(T) , \quad (4-14)$$

with t corresponding to the thickness of the film, as obtained by AFM; and using formulas 4-12 and 4-13 for R .

Electrical Noise Measurements

Stochastic fluctuations of electrical quantities are commonly referred to as electrical noise. Its origin can arise from different types of phenomena. The investigation of noise as a function of external parameters reveals information about kinetic processes occurring in matter, such as charge transport.

One of the most important types of noise for electronic device design is flicker noise. It consists of low frequencies (<100 kHz) with a spectral density S that assumes a form $1/f^\gamma$, where f is the frequency and γ is an empirical parameter close to 1 [142]. This type of noise influences the sensitivity of sensor amplifiers and transducers [143], independently of the measurement time. Moreover, non-linearities in devices cause an up conversion of its contributions to high frequency, having an impact even on telecommunication systems [144]. It can be caused by fluctuations in either number of the charge carriers or their mobility, or both. In graphene devices, the $1/f$ noise component is commonly attributed to mobility fluctuations [145].

Noise measurements were performed by Prof. C. Barone and Prof. S. Pagano (University of Salerno, Italy). The experimental set-up consists of a closed-cycle cryo-cooler system, operating over the [8; 325] K temperature range, connected to external electrical equipment. The sample is measured in a linear, four-contact configuration. Gold electrodes were fabricated *ad hoc* by thermal evaporation. Distances between electrodes

were optimised to reduce possible electrical interferences. Electrical contact was guaranteed by wire bonding the electrodes to circuital lines on the sample holder. Sample bias was applied to the two external contacts with a low-noise dc current source (model 6221, *Keithley*). The resulting voltage was detected at the inner contacts with a dynamic signal analyser (model 35670A, *HP*), through a low-noise preamplifier (model 5113, *Ametek*). The power spectral density is computed by integrating voltage fluctuations δV on time, with a time step Δt .

$$S_V(f) = \lim_{\Delta t \rightarrow \infty} \frac{2}{\Delta t} \left| \int_{-\frac{\Delta t}{2}}^{\frac{\Delta t}{2}} dt e^{i\omega t} \delta V(t) \right|^2 \quad (4-15)$$

The overall instrumental background noise was typically $1.4 \cdot 10^{-17}$ V²/Hz. In order to exclude external noise sources, such as electrical connections at the contacts, a procedure based on the combination of two- and four-probe measurements was employed [146]. Temperature was measured by a Cernox[®] resistor thermometer placed in contact with the sample holder. Temperature stabilization was achieved through a computer-controlled feedback loop with an accuracy within 0.1 K.

4.4 References

- [16] Dimiev, A.M., *Mechanism of Formation and Chemical Structure of Graphene Oxide*, in *Graphene Oxide*, A.M. Dimiev and E. S., Wiley, p. 36-84 (2016). www.doi.org/10.1002/9781119069447.ch2
- [34] Mattevi, C., *et al.*, *Evolution of Electrical, Chemical, and Structural Properties of Transparent and Conducting Chemically Derived Graphene Thin Films*. *Advanced Functional Materials* **19**, 16, p. 2577-2583 (2009). www.doi.org/10.1002/adfm.200900166
- [108] Liscio, A., *et al.*, *Evolution of the size and shape of 2D nanosheets during ultrasonic fragmentation*. *2D Materials* **4**, 2, p. 025017 (2017). www.doi.org/10.1088/2053-1583/aa57ff
- [120] Hertz, H., *Ueber einen Einfluss des ultravioletten Lichtes auf die elektrische Entladung*. *Annalen der Physik* **267**, 8, p. 983-1000 (1887). www.doi.org/10.1002/andp.18872670827
- [121] Einstein, A., *Über einen die Erzeugung und Verwandlung des Lichtes betreffenden heuristischen Gesichtspunkt*. *Annalen der Physik* **322**, 6, p. 132-148 (1905). www.doi.org/10.1002/andp.19053220607
- [122] Scofield, J.H., *Hartree-Slater subshell photoionization cross-sections at 1254 and 1487 eV*. *Journal of Electron Spectroscopy and Related Phenomena* **8**, 2, p. 129-137 (1976). [www.doi.org/10.1016/0368-2048\(76\)80015-1](http://www.doi.org/10.1016/0368-2048(76)80015-1)
- [123] Zhong, J.-Q., *et al.*, *Synchrotron-based ambient pressure X-ray photoelectron spectroscopy of hydrogen and helium*. *Applied Physics Letters* **112**, 9, p. 091602 (2018). www.doi.org/10.1063/1.5022479
- [124] Damascelli, A., *Probing the Electronic Structure of Complex Systems by ARPES*. *Physica Scripta* **T109**, p. 61 (2004). www.doi.org/10.1238/physica.topical.109a00061
- [125] Koopmans, T., *Über die Zuordnung von Wellenfunktionen und Eigenwerten zu den Einzelnen Elektronen Eines Atoms*. *Physica* **1**, 1, p. 104-113 (1934). www.doi.org/10.1016/S0031-

- [8914\(34\)90011-2](https://doi.org/10.1016/0009-2614(70)80309-8); Manne, R., *et al.*, *Koopmans' theorem for inner-shell ionization*. *Chemical Physics Letters* **7**, 2, p. 282-284 (1970). [www.doi.org/10.1016/0009-2614\(70\)80309-8](https://doi.org/10.1016/0009-2614(70)80309-8)
- [126] Fairley, N., *CasaXPS French Cookbook*, Casa Software Limited (2014).
- [127] Shirley, D.A., *High-Resolution X-Ray Photoemission Spectrum of the Valence Bands of Gold*. *Physical Review B* **5**, 12, p. 4709-4714 (1972). [www.doi.org/10.1103/PhysRevB.5.4709](https://doi.org/10.1103/PhysRevB.5.4709)
- [128] Tougaard, S., *Practical algorithm for background subtraction*. *Surface Science* **216**, 3, p. 343-360 (1989). [www.doi.org/10.1016/0039-6028\(89\)90380-4](https://doi.org/10.1016/0039-6028(89)90380-4)
- [129] Briggs, D., *Handbook of X-ray and ultraviolet photoelectron spectroscopy*, Heyden & Son LTD (1979).
- [130] Seah, M.P., *An accurate and simple universal curve for the energy-dependent electron inelastic mean free path*. *Surface and Interface Analysis* **44**, 4, p. 497-503 (2012). [www.doi.org/10.1002/sia.4816](https://doi.org/10.1002/sia.4816)
- [131] Kovtun, A., *et al.*, *Accurate chemical analysis of oxygenated graphene-based materials using X-ray photoelectron spectroscopy*. *Carbon* **143**, p. 268-275 (2019). [www.doi.org/10.1016/j.carbon.2018.11.012](https://doi.org/10.1016/j.carbon.2018.11.012)
- [132] Lennard-Jones, J.E., *Cohesion*. *Proceedings of the Physical Society* **43**, 5, p. 461-482 (1931). [www.doi.org/10.1088/0959-5309/43/5/301](https://doi.org/10.1088/0959-5309/43/5/301)
- [133] Liscio, A., *Scanning Probe Microscopy beyond Imaging: A General Tool for Quantitative Analysis*. *ChemPhysChem* **14**, 6, p. 1283-1292 (2013). [www.doi.org/10.1002/cphc.201200880](https://doi.org/10.1002/cphc.201200880)
- [134] Pollard, A., *et al.*, *Good Practice Guide No. 145 -Characterisation of the Structure of Graphene*. 2017, National Physical Laboratory (NPL).
- [135] Williams, D.B., *et al.*, *Transmission Electron Microscopy: a textbook for materials science*, Springer (2009). [www.doi.org/10.1007/978-0-387-76501-3](https://doi.org/10.1007/978-0-387-76501-3)
- [136] Ferrari, A.C., *et al.*, *Raman Spectrum of Graphene and Graphene Layers*. *Physical Review Letters* **97**, 18, p. 187401 (2006). [www.doi.org/10.1103/PhysRevLett.97.187401](https://doi.org/10.1103/PhysRevLett.97.187401)
- [137] Ferrari, A.C., *et al.*, *Raman spectroscopy as a versatile tool for studying the properties of graphene*. *Nature Nanotechnology* **8**, 4, p. 235-246 (2013). [www.doi.org/10.1038/nnano.2013.46](https://doi.org/10.1038/nnano.2013.46); Pimenta, M.A., *et al.*, *Studying disorder in graphite-based systems by Raman spectroscopy*. *Physical Chemistry Chemical Physics* **9**, 11, p. 1276-1290 (2007). [www.doi.org/10.1039/B613962K](https://doi.org/10.1039/B613962K)
- [138] Dimiev, A.M., *Raman Spectroscopy*, in *Graphene Oxide*, A.M. Dimiev and E. S., Wiley, p. 100 - 111 (2016). [www.doi.org/10.1002/9781119069447.ch2](https://doi.org/10.1002/9781119069447.ch2)
- [139] Bragg, W.H., *et al.*, *The reflection of X-rays by crystals*. *Proceedings of the Royal Society of London. Series A, Containing Papers of a Mathematical and Physical Character* **88**, 605, p. 428-438 (1913). [www.doi.org/10.1098/rspa.1913.0040](https://doi.org/10.1098/rspa.1913.0040)
- [140] Warren, B.E. *X-ray study of the graphitization of carbon black*. in *First and Second Conferences on Carbon*. 1956.
- [141] van der Pauw, L.J., *A method of measuring specific resistivity and Hall effect of discs of arbitrary shape*. *Philips Res. Rep* **13**, 1, p. 1-9 (1958).
- [142] Kogan, S., *1/f noise and random telegraph noise*, in *Electronic noise and fluctuations in solids*, Cambridge Univ. Press, p. 239 (1996).
- [143] Letzter, S., *et al.*, *Noise in amplifiers*. *IEEE Spectrum* **7**, 8, p. 67-75 (1970). [www.doi.org/10.1109/MSPEC.1970.5213514](https://doi.org/10.1109/MSPEC.1970.5213514); Mohammadi, A., *et al.* *Dealing with 1/f noise in MEMS electrothermal sensing*. in *IECON 2011 - 37th Annual Conference of the IEEE Industrial Electronics Society*. 2011; Stoop, R.L., *et al.*, *Charge Noise in Organic Electrochemical Transistors*. *Physical Review Applied* **7**, 1, p. 014009 (2017). [www.doi.org/10.1103/PhysRevApplied.7.014009](https://doi.org/10.1103/PhysRevApplied.7.014009)
- [144] Levantino, S., *et al.*, *Frequency dependence on bias current in 5 GHz CMOS VCOs: impact on tuning range and flicker noise upconversion*. *IEEE Journal of Solid-State Circuits* **37**, 8, p. 1003-1011 (2002). [www.doi.org/10.1109/JSSC.2002.800969](https://doi.org/10.1109/JSSC.2002.800969)
- [145] Balandin, A.A., *Low-frequency 1/f noise in graphene devices*. *Nature Nanotechnology* **8**, 8, p. 549-555 (2013). [www.doi.org/10.1038/nnano.2013.144](https://doi.org/10.1038/nnano.2013.144)
- [146] Barone, C., *et al.*, *Experimental technique for reducing contact and background noise in voltage spectral density measurements*. *Review of Scientific Instruments* **78**, 9, p. 093905 (2007). [www.doi.org/10.1063/1.2786271](https://doi.org/10.1063/1.2786271)

Chapter 5

CHARACTERIZATION OF GRM THIN FILM STRUCTURES

This chapter presents the chemical and physical properties of GRM thin films produced for this thesis work.

Given the diverse nature of their assembly, the properties of GRM thin films do not depend only on those of the building block but also on how their structures are formed (*i.e.* networks) with different geometries. Here, we study the use of two nanoflake types with different structural complexity and dimensionality: pure 2D reduced graphene oxide (RGO) and electrochemically exfoliated GO (EGO) showing a multi-layered structure. Their assembly into GRM thin films is described.

5.1 Reduced Graphene Oxide (RGO)

Reduced graphene oxide (RGO) was obtained by the thermal reduction of GO. An AFM image of RGO sheets deposited on a SiO₂/Si substrate is reported in Figure 5-1 with the corresponding histogram analysis. All the RGO sheets are mono-layer objects (*i.e.* purely 2D nanosheets) with thickness = 0.6 ± 0.1 nm, in excellent agreement with literature values [147].

This value is larger than the sheet-to-sheet interspacing in graphite (≈ 0.335 nm) [148] and is due to by the interplay of various phenomena: no Bernal stacking between RGO and substrate, different tip interactions between nanosheet and substrate and also the presence of residual water trapped under the nanosheet. [149].

By acquiring and analysing multiple AFM images (as shown in Fig. 5-1), as well as optical and SEM images on larger scales, it was possible to retrieve statistical information about the morphology of the sheets: thickness, size and shape. Figure 5-2 reports the distributions of sheet thickness and sheet size from the analysis of AFM images

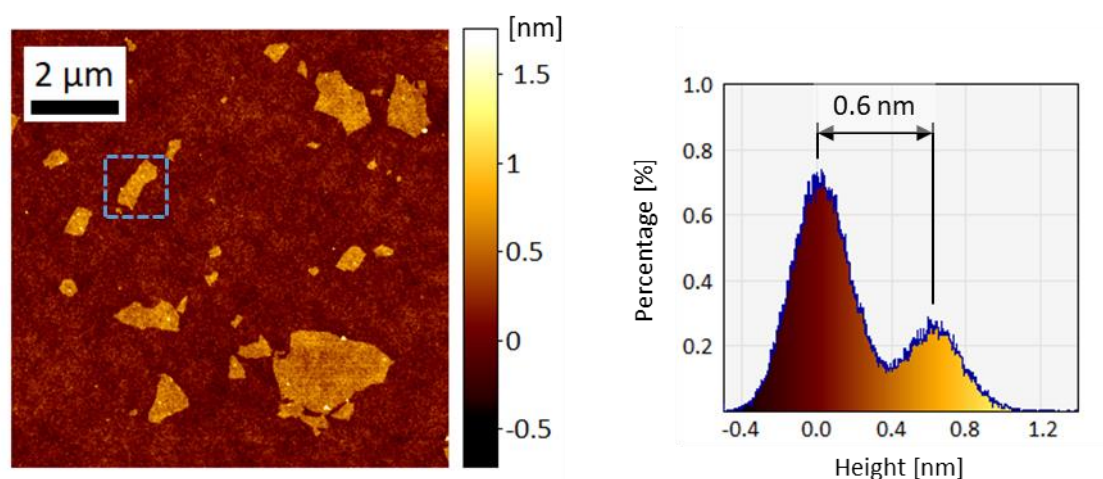


Figure 5-1. AFM image of isolated RGO sheets deposited on SiO_2 by spin-coating. The z-colour scale indicates the height of measured objects in a false colour system: RGO sheets are shown in yellow, while the substrate is in a dark red nuance. RGO owns a uniform thickness of (0.6 ± 0.1) nm including the substrate contribution, as shown in the height distribution on the right (from dashed, blue line area in the image).

corresponding to 774 nanosheets. The thickness distribution is quite narrow and peaked to 0.6 nm, as already observed. The slight asymmetry at lower heights is ascribed to the causes mentioned above, including trapped water. Fig. 5-2b shows a broad distribution of lateral size ranging from 100 nm to 2 μm with a mean value of (320 ± 20) nm.

The chemical composition of RGO was studied by XPS. In our RGO thin films, given the high treatment temperature of 900 °C, the O 1s signal was almost absent. Moreover, the XPS spectra showed no signals from trace metals (see Appendix A.3). Figure 5-3 shows the

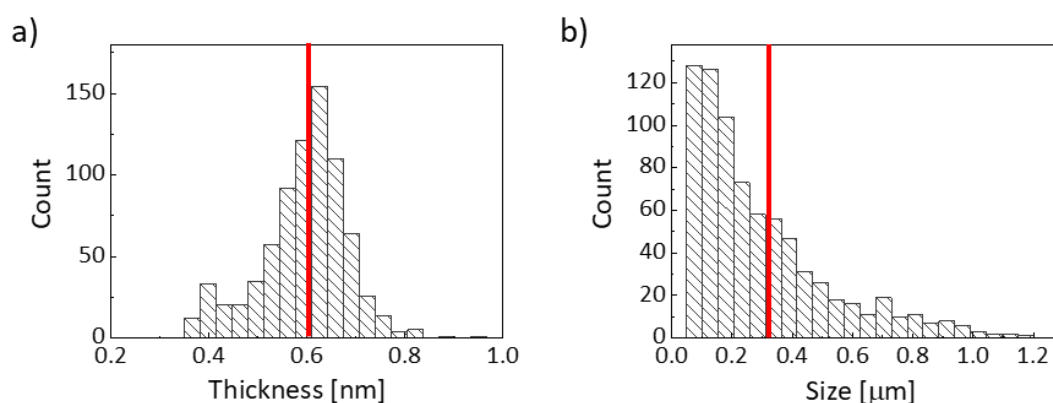


Figure 5-2. (a) Thickness distribution and (b) Size distribution of RGO sheets, as determined from AFM images. A total of 774 objects were analysed. The red line in both graphs indicates the mean value. We recall that Size is equal to the square root of RGO sheet area.

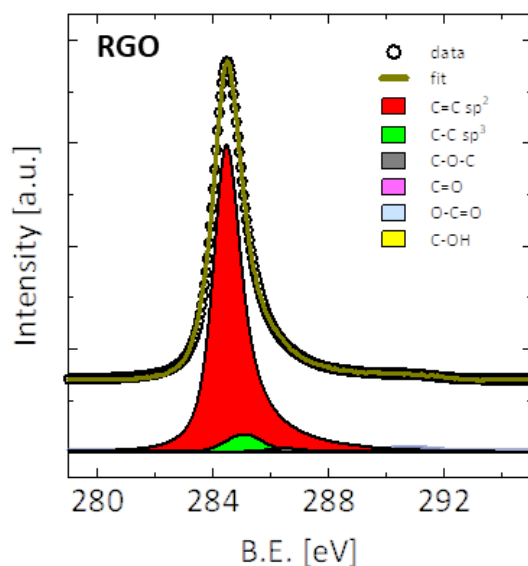


Figure 5-3. High-resolved XPS spectra of C 1s for filtered RGO. B.E. in x-axis refers to binding energy E_B . The colored peaks below the data represents the components used in the analysis. RGO is composed mainly by sp^2 hybridised carbon (>90%) with a small amount of C sp^3 and residual oxygen functional groups.

C 1s XPS signal of a filtered RGO film. The main C 1s peak at 284.5 eV is attributed to sp^2 hybridized carbon. The high percentage of C sp^2 , above 92%, confirms the successful reduction with partial restoration of the graphene structure. The amount of sp^2 hybridized carbon is comparable to values measured for liquid-phase exfoliated graphene nanoplatelets [15,150]. The low intensity C sp^3 signal is due mainly to out-of-plane topological defects, as well as holes and in minor part by residual oxygen functionalities, such as hydroxyl groups, which are still present. The percentages of C sp^3 are reported in Table 5-1 for the three kinds of films.

Comparison of XPS spectra of single RGO sheets [102] and RGO thin films (*ca.* 60 nm thick) reveals the same chemical composition allowing one to neglect possible unwanted chemical modifications, such as inter-sheet bonding, as well as the presence of solvent residue trapped between stacked sheets during thermal reduction of the films. Furthermore, the observation that the sp^3 peak (related to the topological defects) does not change between single sheet and multi-sheet films, indicates that the trapped water is removed without damaging the film structure.

Table 5-1. Representative parameters of the studied RGO films. Carbon sp^2 and sp^3 fractions were determined by fitting the high-resolution C 1s XPS signal. Thickness was estimated by AFM.

	C sp^2 [%]	C sp^3 [%]	thickness [nm]
spin-coated RGO	92 ± 2	6.0 ± 1.2	55 ± 6
filtered RGO	93 ± 2	3.9 ± 1.6	61 ± 7
spray-coated RGO	94 ± 2	3.6 ± 0.6	66 ± 4

The possibility of inter-sheet chemical bonding after reduction was investigated using Raman spectroscopy. The GO sheets were deposited by spin-coating on a clean SiO_2 substrate. To obtain partially overlapped sheets, the deposition was repeated twice on the same substrate. Then, they were reduced in high vacuum at $900^\circ C$ (defect content $\lesssim 3\%$ based on the XPS analysis above). The GO suspension was deposited directly from the reaction vessel, without further sonication. This produces large sheets, up to hundreds of μm in length. Three Raman spectra acquired for different numbers of layers are presented in Figure 5-4. The G peak confirms the presence of a graphitic-like structure. As expected, the D peak is also visible in all three spectra. The RGO sheet is indeed

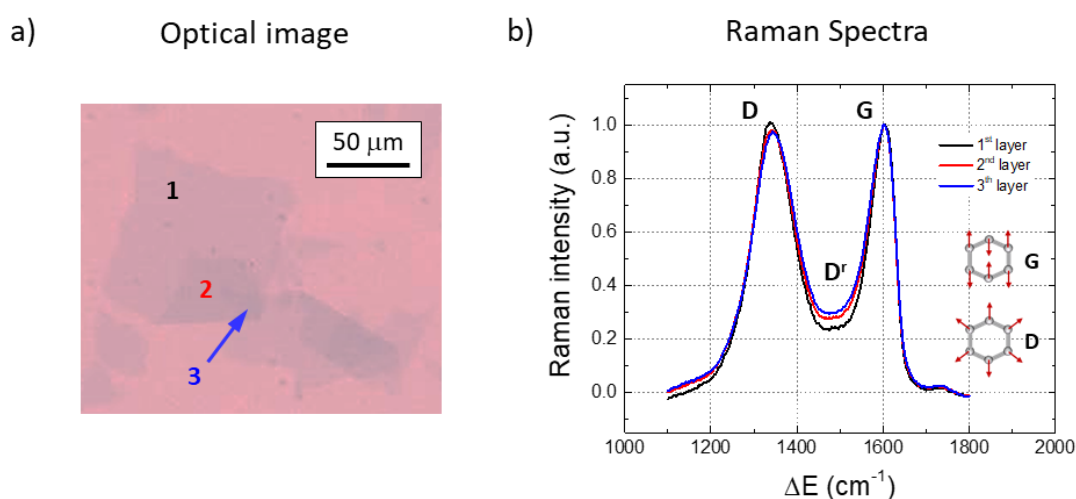


Figure 5-4. (a) Optical image of large RGO sheets. The sheets are superimposed and were reduced at $900^\circ C$ in high vacuum after deposition. Coloured numbers indicate the micrometric regions where Raman spectroscopy was performed. (b) Raman spectra of RGO in (a). We thank V. Mussi of CNR-IMM (Italy) for performing the measurements.

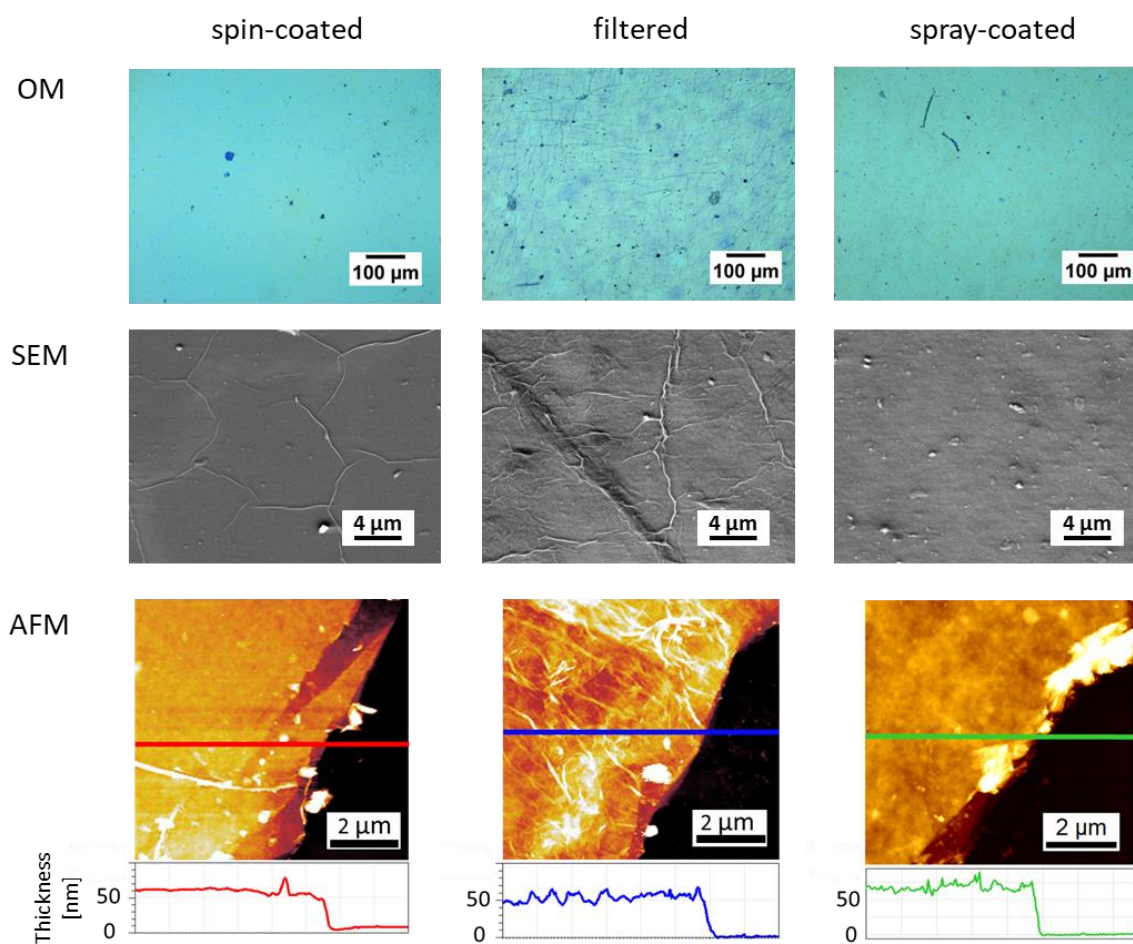


Figure 5-5. Multi-scale morphological images of RGO thin films fabricated by spin-coating, filtration and spray-coating deposition techniques. Images obtained by (OM) Optical, (SEM) Scanning Electron and (AFM) Atomic Force Microscopies. AFM images show the film borders obtained by scratch. Profile heights correspond to the traced horizontal lines. AFM z-ranges: 100 nm.

topologically and chemically disordered with respect to a single-layer of pure graphene. Negligible differences in G and D peaks are observed by increasing the number of layers. An additional contribution to the G peak, D' , is visible at about 1400 cm^{-1} . D' is caused by deformation of the RGO sheet connected with residual oxygen functionalities [151]. D' differs between single- and multi-layer samples and is roughly constant for two- and three-layer sheets. In agreement with XPS, this indicates that new defects “trapped” between layers are negligible.

Finally, we employed optical microscopy, SEM and AFM to study the surface morphology of the obtained RGO thin films on different length scales. Representative images are shown in Figure 5-5.

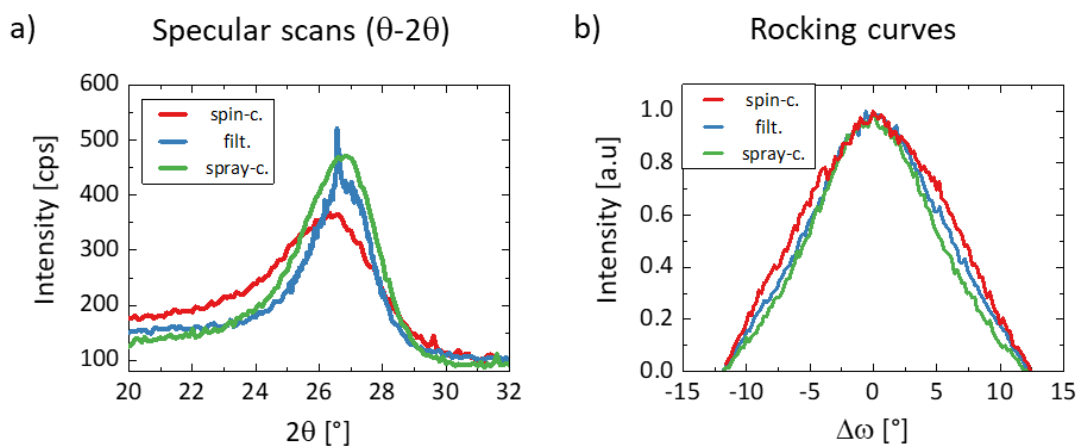


Figure 5-6. XRD spectra for the three type of RGO films. Intensity- 2θ spectra (a) and Intensity- $\Delta\omega$ spectra (b) obtained by specular scan measurements and by rocking curves measurements, respectively. x-axis of (b) is reported with respect to $2\theta_{002}$ positions.

Filtered RGO films are the only ones to show visible surface wrinkles on the sub-millimetre scale. In fact, the filtered film surface imaged was in contact with the nylon filtering membrane before the transfer. These wrinkles are thus probably related to the morphology of the membrane used and do not seem to influence the film structure underneath nor, more importantly, sheet stacking.

On the micro-metric scale, there are thinner surface wrinkles in addition to the previous ones on filtered RGO films and in spin-coated RGO films. These are shown in the SEM micrographs in Figure 5-5 as bright curved lines, but are not observed in spray-coated films suggesting that this surface perturbation could be ascribed to longer contact time with water during sheets deposition. Indeed, a process of stacking and re-stacking can occur on a time scale of tens of seconds. This occurs in the spin-coating procedure when multiple deposition steps have been performed (see Chapter 3).

AFM analysis quantified the fabricated thin film thickness by measuring the height profile at their borders (bottom row in Fig. 5-5). The thickness of the thin films prepared using the various procedures amounts to about 60 nm, average values being shown in Table 5-1.

The structure of the RGO films was analysed using XRD comparing the results obtained on films prepared using the three different deposition methods. For all the samples, θ - 2θ measurements (see Chapter 4) show a single Bragg diffraction peak centred around 26.6° ,

corresponding to the characteristic [002] crystal direction of graphene planes in turbostratic graphite [148,152]. No peak is observed at 11.2° (*i.e.* the characteristic [001] peak of GO, as shown in Figure A.3), nor at other angles in the measured range from 3° to 50° . In the case of filtered films, a further sharp peak superimposed over the [002] one clearly indicating the presence of a small amount of additional thick graphite flakes in the film. However, since we have no optical evidence of such crystalline structures, we consider that they do not affect the macroscopic charge transport behaviour of the thin film. Thus, we focus on the [002] peak and fit it with a Lorentzian curve.

Using the Bragg and Scherrer equations (eqn. 4- and eqn. 4- respectively) we calculated the peak position and its FWHM obtaining the z-periodicity d between graphene planes and their z-coherence length L [153]. To a first approximation, the crystalline domains are graphene sheets stacked in parallel and L corresponds to the average value of the domain thicknesses.

The misalignment of the domains (*i.e.* mosaicity) was measured by the rocking curves (see section 4.2) acquired at the [002] Bragg peak of each sample. All the measurements were performed on two independent samples for each deposition technique. Both XRD data (θ - 2θ and rocking curves) are depicted in Figure 5-6, all the results being reported in Table 5-2.

Table 5-2. Measured and computed XRD structure parameters of the three kind of RGO thin films. The parameters (indicated with $\langle \dots \rangle$) are the average calculated over values of independent samples. d : z-periodicity; L : z-coherence length; and M : mosaicity.

	$\langle 2\theta_{002} \rangle [^\circ]$	$\langle \text{FWHM}_{002} \rangle [^\circ]$	$\langle d \rangle [\text{\AA}]$	$\langle L \rangle [\text{nm}]$	$\langle M \rangle [^\circ]$
spin-coated RGO	26.16 ± 0.03	3.57 ± 0.06	3.40 ± 0.03	2.28 ± 0.04	21 ± 4
filtered RGO	26.69 ± 0.03	2.31 ± 0.05	3.34 ± 0.05	3.6 ± 0.2	12 ± 1
	26.70 ± 0.01	/	3.35 ± 0.07		
spray-coated RGO	26.65 ± 0.03	2.56 ± 0.03	3.34 ± 0.09	3.20 ± 0.1	12 ± 1

The most disordered films are those obtained by spin-coating as they show shorter coherence lengths and higher mosaicities. This can be ascribed to the large number of

repeated depositions (*i.e.* 50 times, see Section 3.2) performed to complete the spin-coating process. Interactions between substrate and deposited nanosheet depends on the deposition step and, indeed, the drop of the suspension can cause a slight re-mixing of previously deposited material. We observed that M increases after 10 depositions. Conversely, the films obtained with the other two methods show similar values corresponding to better stacking of sheets and larger z -domains. In general, the lower mosaicity value is *ca.* 12° ; for the sake of comparison, the lower quality commercial highly ordered pyrolytic graphite (HOPG, grade ZYH) has M values of $3.5^\circ \pm 1.5^\circ$ [154].

5.2 Electrochemically exfoliated GO (EGO)

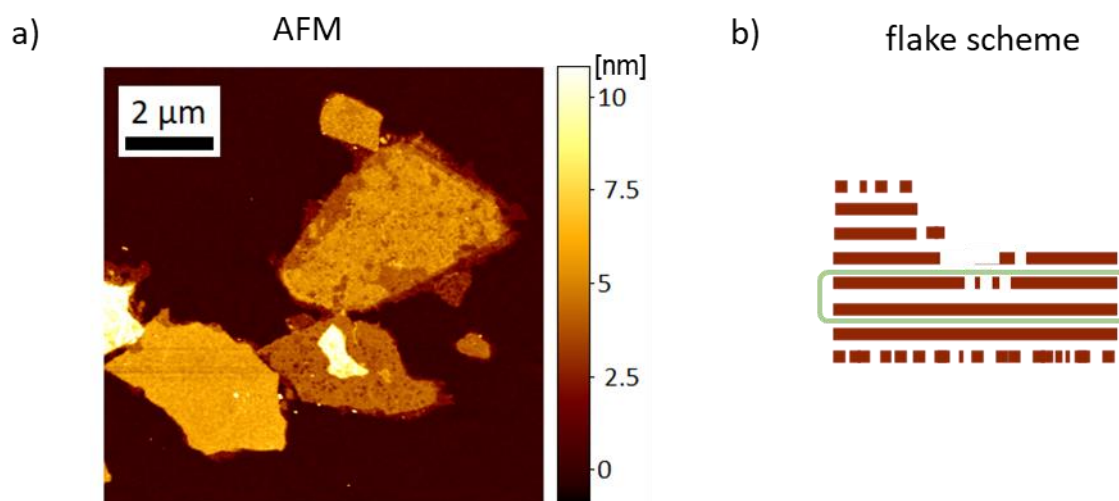


Figure 5-7. (a) AFM image of representative EGO sheets deposited on SiO_2 by spin-coating. The height is represented by a set of false colours, from dark brown (*i.e.* the substrate) to deep yellow. The sheets have different thicknesses and are composed by multiple (*bi*-)layers. Holes and wrinkles, visible on the top surface of two sheets, are caused both by the fastness of the electrochemical oxidation-exfoliation process and by the amount of released energy. (b) A scheme of a representative EGO flake.

EGO flakes show a multi-layered structure, as clearly evinced by the stepped features observed in the AFM image in Figure 5-7a, with heights ranging from 1.6 nm to 16 nm. The repeating unit of the layered structure is given by partially oxidized graphene bilayers still stacked in an AB configuration (thickness ≈ 2 nm), with most of the oxygen atoms

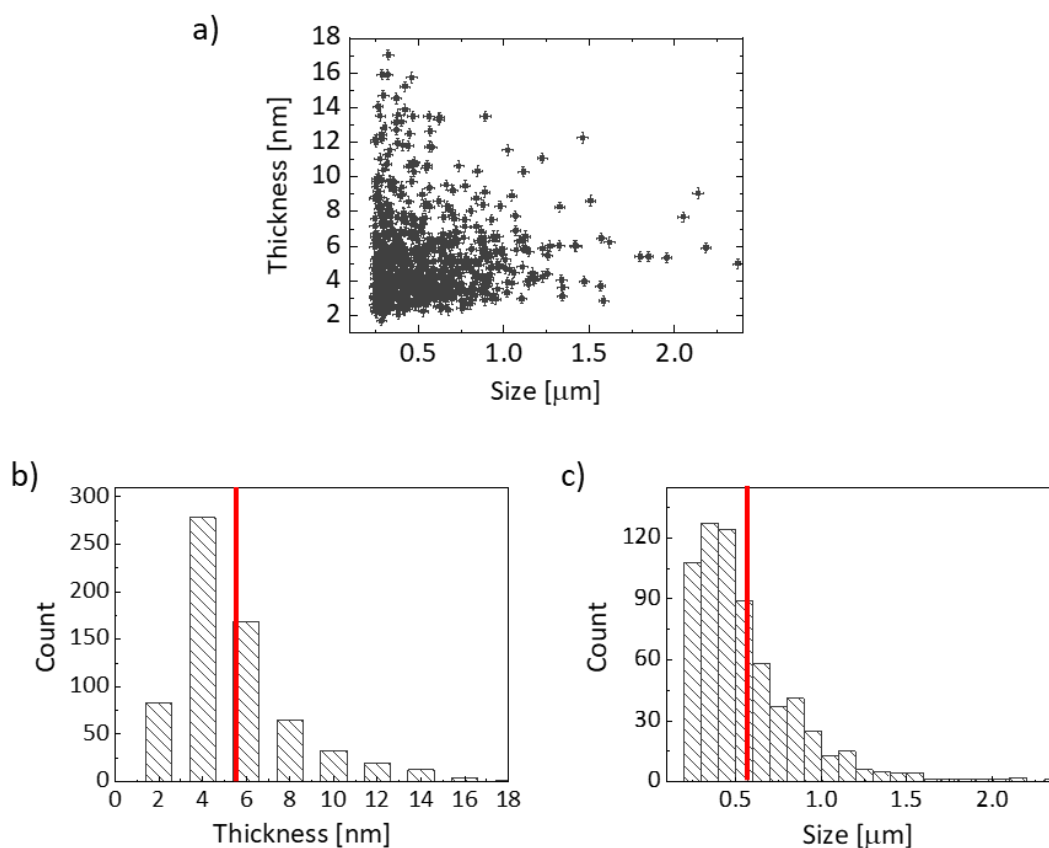


Figure 5-8. (a) Thickness versus Size plot of studied EGO flakes. It is immediately evident that EGO is not simply mono-atomic in thickness, but it comprises thicker structure. The corresponding (b) thickness and (c) size distributions are also reported. The red line in (b) and (c) indicates the mean value.

decorating the external surfaces which show holes of tens of nanometres and small fragments caused by the relatively fast synergic ion intercalation and oxidation during the synthesis process, together with adsorbed oxidative debris [33]. A scheme of the flake is depicted in Fig. 5-7b.

Compared to single-layer structures, the dimensions of EGO disperse both in height and lateral size. Figure 5-8a shows the measured values of 665 EGO flakes in a height vs. lateral size plot (*i.e.* out-of-plane size vs in-plane size). Using the same plot to represent RGO, all the datapoints should lie on a line at fixed height. A qualitative analysis of EGO shows that the datapoints are quite scattered in the plot suggesting that heights and lateral dimensions are decoupled and that therefore there are no families of flakes with distinct geometric properties.

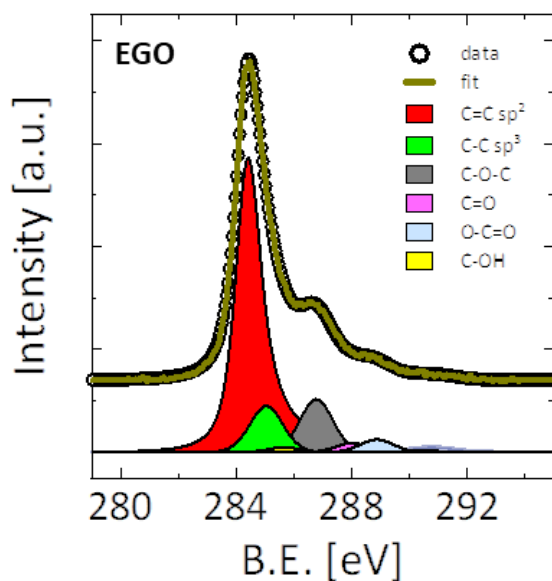


Figure 5-9. High-resolved XPS spectra of C 1s for EGO. B.E. in x-axis refers to binding energy E_B . The colored peaks below the data represent the components used in the analysis.

Analysis of the height distributions shows a mean value (5.5 ± 0.1) nm, while the lateral dimensions of EGO flakes are similar to those of RGO corresponding to a mean size of (570 ± 20) nm.

Chemical analysis from XPS measurements confirms the mild oxidation of EGO with an aromatic content of 71% (Table 5-3.). Indeed, epoxides, hydroxides and carboxylic groups are still present on the EGO flake. This is highlighted by the larger C sp^3 signal, amounting to 11%, with respect to the lower RGO signal. Solvent residues are excluded from the final thin film by the fabrication technique chosen (*i.e.* filtration), which guarantees efficient solvent removal. In addition, undesired metallic elements are not observed (see Appendix A.3). Figure 5-9 reports the C 1s XPS spectrum of the prepared EGO.

Table 5-3. Representative parameters of EGO thin films fabricated by vacuum-assisted filtration. For comparison, the second row recalls the same values defined for filtered RGO films in Table 5-1.

	C sp^2 [%]	C sp^3 [%]	thickness [nm]
EGO	71 ± 2	11 ± 2	140 ± 20
RGO	93 ± 2	3.9 ± 1.6	61 ± 7

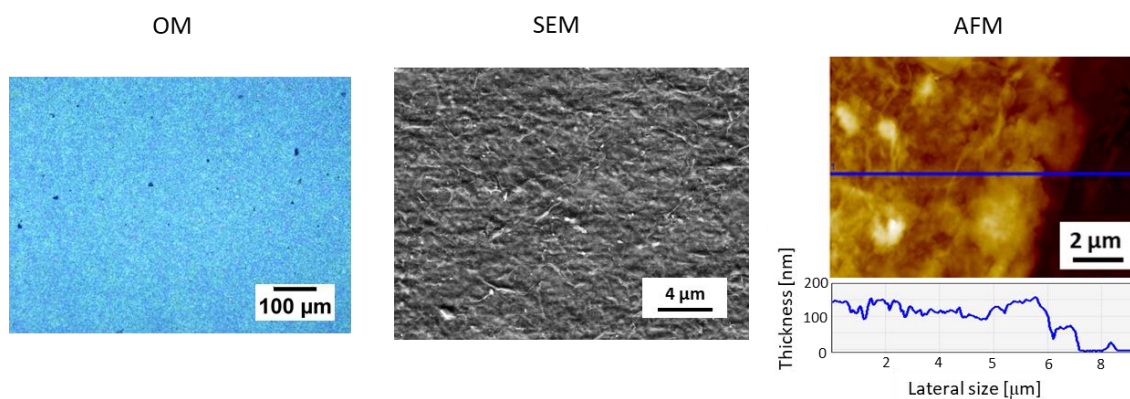


Figure 5-10. Multi-scale morphological images of EGO thin films fabricated with filtration deposition technique. Images obtained by (OM) Optical, (SEM) Scanning Electron and (AFM) Atomic Force Microscopies. AFM images show the film borders obtained by scratch. Profile heights correspond to the traced horizontal lines. AFM z-ranges: 200 nm.

Surface wrinkles observed in filtered RGO films are also visible in EGO films (OM and SEM images in Figure 5-10). However, they appear not as distinct here because the wider distribution of flake thicknesses in EGO contributes to a rougher film surface. This observation is quantitatively supported by AFM analysis of the EGO film surface, showing the height profile in Fig. 5-10.

The specular scan XRD plot of an EGO thin film is shown in Figure 5-11a (blue line). EGO shows a single feature at 26.5° similar to that measured for RGO (corresponding to the [002] Bragg peak of graphite). The peak has a slightly asymmetrical shape with a steep low-angle tail, indicating structural disorder in the flake stacking. The z-coherence length

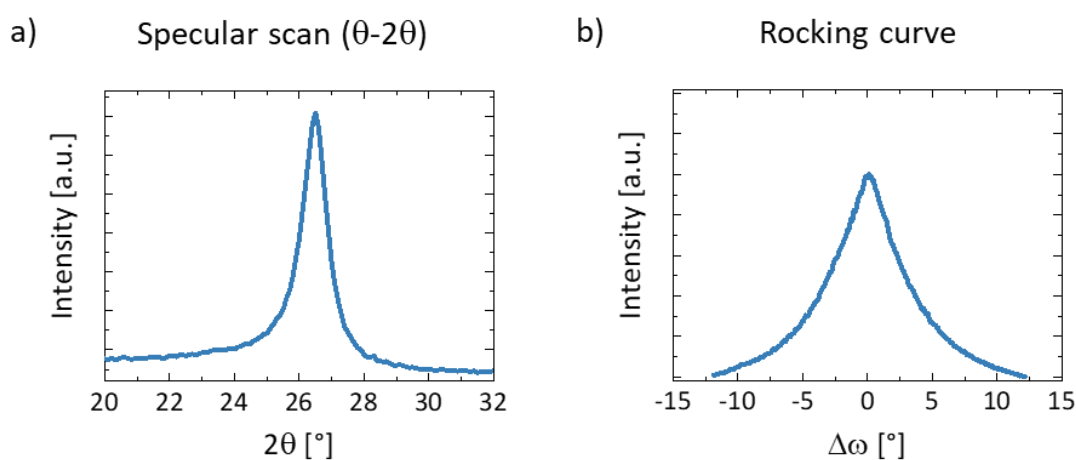


Figure 5-11. XRD measurements on EGO thin films: (a) specular scan and (b) rocking curve.

Table 5-4. Measured and computed XRD structure parameters of the EGO and RGO filtered, thin films. Values (indicated with $\langle \dots \rangle$) are averaged over independent samples. The RGO parameters are the one already presented previously.

	$\langle 2\theta_{002} \rangle$ [°]	$\langle \text{FWHM}_{002} \rangle$ [°]	$\langle d \rangle$ [Å]	$\langle L \rangle$ [nm]	$\langle M \rangle$ [°]
EGO film	26.46 ± 0.03	0.93 ± 0.02	3.37 ± 0.02	8.8 ± 0.2	6.0 ± 0.5
RGO film	26.69 ± 0.03	2.31 ± 0.05	3.34 ± 0.05	3.6 ± 0.2	12 ± 1

L amounts to (8.8 ± 0.2) nm and is systematically larger than the mean height value calculated from the height distribution: $h_{\text{mean}} \approx 5.5$ nm, suggesting that the building block consists of single or two-stacked EGO flakes.

The mosaicity spread M is obtained from the rocking curve in Fig. 5-11b and amounts to $(6.0 \pm 0.5)^\circ$. For the EGO film, M is significantly lower than those for RGO thin films. All the XRD parameters obtained are compared in Table 5-4 for the two types of GRM filtered films.

The higher order of alignment of the building blocks in the case of the EGO films can be ascribed to the mechanical properties of the GRM during deposition. As the EGO flakes

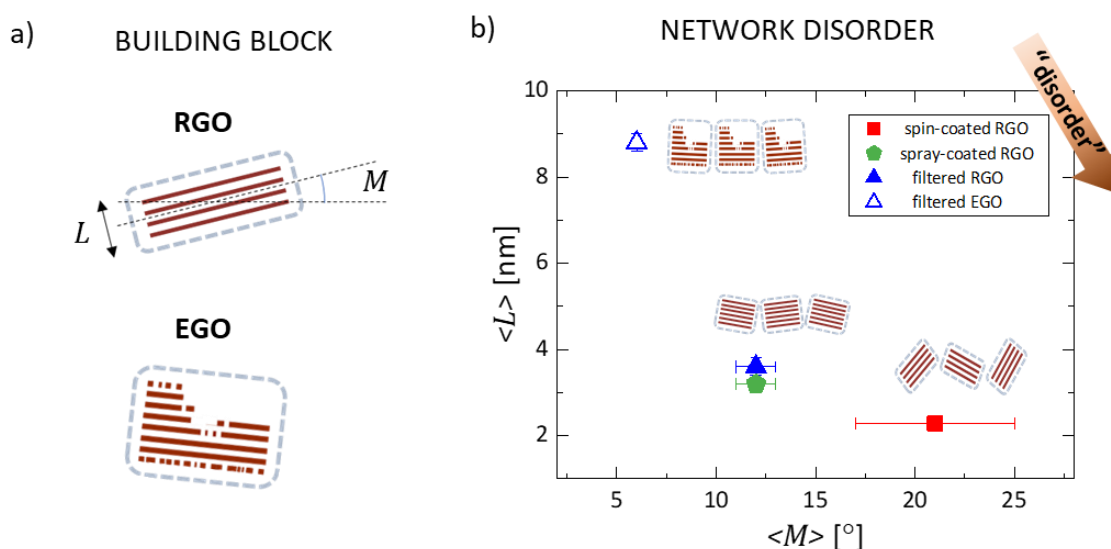


Figure 5-12. Structural analysis of RGO and EGO thin films. (a) Scheme of the building blocks and (b) their arrangement plotted as z-coherence length L vs. mosaicity M (averaged value over independent samples). A sketch of the proposed structural model for each sample is depicted next to each square marker.

are more rigid with respect to single GO sheets, they arrange into a thin film with larger voids and slightly less-misoriented flakes.

In Figure 5-12 the structural data are plotted as z-coherence length L vs. mosaicity M with the corresponding cartoon of the structural schemes.

Summarising, both RGO and EGO thin films show a nanometric coherence length along the z-axis larger than the thickness of a single sheet (or flake), indicating a multi-scale structure of the thin films which can be described as networks of different building blocks, such as *ca.* 5 stacked RGO sheets and 1 or 2 EGO flakes, respectively.

5.3 References

- [15] Kovtun, A., *et al.*, *Benchmarking of graphene-based materials: real commercial products versus ideal graphene*. 2D Materials **6**, 2, p. 025006 (2019). www.doi.org/10.1088/2053-1583/aafc6e
- [33] Xia, Z., *et al.*, *Dispersion Stability and Surface Morphology Study of Electrochemically Exfoliated Bilayer Graphene Oxide*. The Journal of Physical Chemistry C **123**, 24, p. 15122-15130 (2019). www.doi.org/10.1021/acs.jpcc.9b03395
- [102] Di Filippo, G., *et al.*, *The evolution of hydrogen induced defects and the restoration of π -plasmon as a monitor of the thermal reduction of graphene oxide*. Applied Surface Science **512**, p. 145605 (2020). www.doi.org/10.1016/j.apsusc.2020.145605
- [147] Gupta, A., *et al.*, *Raman Scattering from High-Frequency Phonons in Supported n-Graphene Layer Films*. Nano Letters **6**, 12, p. 2667-2673 (2006). www.doi.org/10.1021/nl061420a; Liscio, A., *et al.*, *Charge transport in graphene-polythiophene blends as studied by Kelvin Probe Force Microscopy and transistor characterization*. Journal of Materials Chemistry **21**, 9, p. 2924-2931 (2011). www.doi.org/10.1039/COJM02940H
- [148] Franklin, R.E., *The structure of graphitic carbons*. Acta Crystallographica **4**, 3, p. 253-261 (1951). www.doi.org/10.1107/s0365110x51000842
- [149] Shearer, C.J., *et al.*, *Accurate thickness measurement of graphene*. Nanotechnology **27**, 12, p. 125704 (2016). www.doi.org/10.1088/0957-4484/27/12/125704
- [150] Marchesini, S., *et al.*, *Gas physisorption measurements as a quality control tool for the properties of graphene/graphite powders*. Carbon **167**, p. 585-595 (2020). www.doi.org/10.1016/j.carbon.2020.05.083
- [151] Claramunt, S., *et al.*, *The Importance of Interbands on the Interpretation of the Raman Spectrum of Graphene Oxide*. The Journal of Physical Chemistry C **119**, 18, p. 10123-10129 (2015). www.doi.org/10.1021/acs.jpcc.5b01590
- [152] Li, Z.Q., *et al.*, *X-ray diffraction patterns of graphite and turbostratic carbon*. Carbon **45**, 8, p. 1686-1695 (2007). www.doi.org/10.1016/j.carbon.2007.03.038
- [153] Ju, H.-M., *et al.*, *Structures of thermally and chemically reduced graphene*. Materials Letters **64**, 3, p. 357-360 (2010). www.doi.org/10.1016/j.matlet.2009.11.016
- [154] *Graphite Monochromators -Product Bulletin*, Momentive, www.momentive.com/en-us/categories/ceramics/graphite-monochromators

Chapter 6

NEW PROTOCOL FOR VRH DATA ANALYSIS

The present chapter introduces a new protocol, fully developed in this work, to analyse charge transport in VRH.

Chapter 2 lists various charge transport models describing the analytic expressions of the temperature dependence of the electrical resistivity and introduces a self-consistent analysis of the experimental data called *Reduced Activation Energy*, $W(T)$. Here, we generalise the approach for a quantitative analysis of the $\rho(T)$ data in the Variable Range Hopping (VRH) regime. Developed to describe the case of RGO thin films, such protocol can be applied to describe all the various VRH regimes of GRM and other materials.

6.1 General Description of VRH

For the sake of clarity, we briefly summarise the results shown in Chapter 2. The analytic equation of the VRH resistivity is given by:

$$\rho_{VRH}(T) = \rho_{0,VRH} \cdot \exp\left\{\left(\frac{T_0}{T}\right)^p\right\} \quad (6-1)$$

where $\rho_{0,VRH}$ is the pre-exponential term, T_0 is the characteristic temperature and p is the exponent describing the type of model. All the terms are referred to VRH regime, for clarity the subscript VRH is omitted being used only in the case of other regimes. Since ρ_0 has only weak temperature dependence, it is commonly taken as a constant value. From a mathematical point-of-view, considering a temperature-independent pre-factor allows one to simplify the calculations, the $W(T)$ equation assumes the following form:

$$W(T) = -\frac{\partial \ln \rho}{\partial \ln T} = p \cdot \left(\frac{T_0}{T}\right)^p \quad (6-2)$$

In a log-log plot ($\ln W$ vs. $\ln T$ plot), the equation takes the linear form:

$$\ln W = -p \cdot \ln T + A \quad (6-3)$$

where the VRH exponent p can be directly obtained from the slope.

In RGO, we observe a clear linear slope at low temperature with $p = \frac{1}{2}$ corresponding to ES-VRH transport. The VRH regime is valid up to a transition temperature T^* , beyond which $W(T)$ becomes constant and the transport is described by the PL regime. This was found to be valid for all the measured RGO devices, from the case of a single RGO sheet, to several sheets partially in contact, up to macroscopic thin films (*ca.* 1x1 cm², thickness up to 60 nm). A representative $W(T)$ curve is depicted in Figure 6-1a.

In the case of thin films with higher conductivity (room temperature resistivity, $\rho_{RT} < 10^{-5}$ $\Omega \cdot m$), instead of a single transition temperature we observe a region of temperatures (marked as ΔT^*) in which the trend becomes sublinear and then constant, as reported in Figure 7-1b. Moreover, the transition region increases as the variation in W (marked as ΔW in the Figures) decreases. Similar behaviour has been previously reported and several models proposed: i) as a transition to a different VRH model [155] or ii) as the presence of two mechanisms acting simultaneously [156].

However, these proposed descriptions show an intrinsic problem: although an increase in the number of parameters allows to a better fit with the experimental data, their use requires a strong theoretical support. Below, we show that the sublinear region can be simply described in terms of ES-VRH regime.

Considering the temperature dependence of the VRH pre-factor, $\rho_0 = \rho_0(T)$, as described by Efros and Shklovskij [157] using percolative methods for a wide range of systems, including inorganic semiconductors, amorphous or lightly doped systems:

$$\rho_0(T) = \rho'_0 \cdot \left(\frac{T_n}{T}\right)^n, \quad (6-4)$$

where ρ'_0 is the temperature-independent prefactor, T_n and n represent the characteristic temperature and the power exponent, respectively. The case $n=0$ corresponds to the temperature-independent pre-factor, as discussed in Chapter 2 and as typically reported in the literature. Conversely, a general framework describing the case $n \neq 0$ is still lacking. Using random resistors networks approaches, n is modelled in terms of a phononic contribution and the electrical potential screening effect due to defects. The calculated n value shows a universal behaviour ranging between -0.8 and -0.7 in the case of amorphous

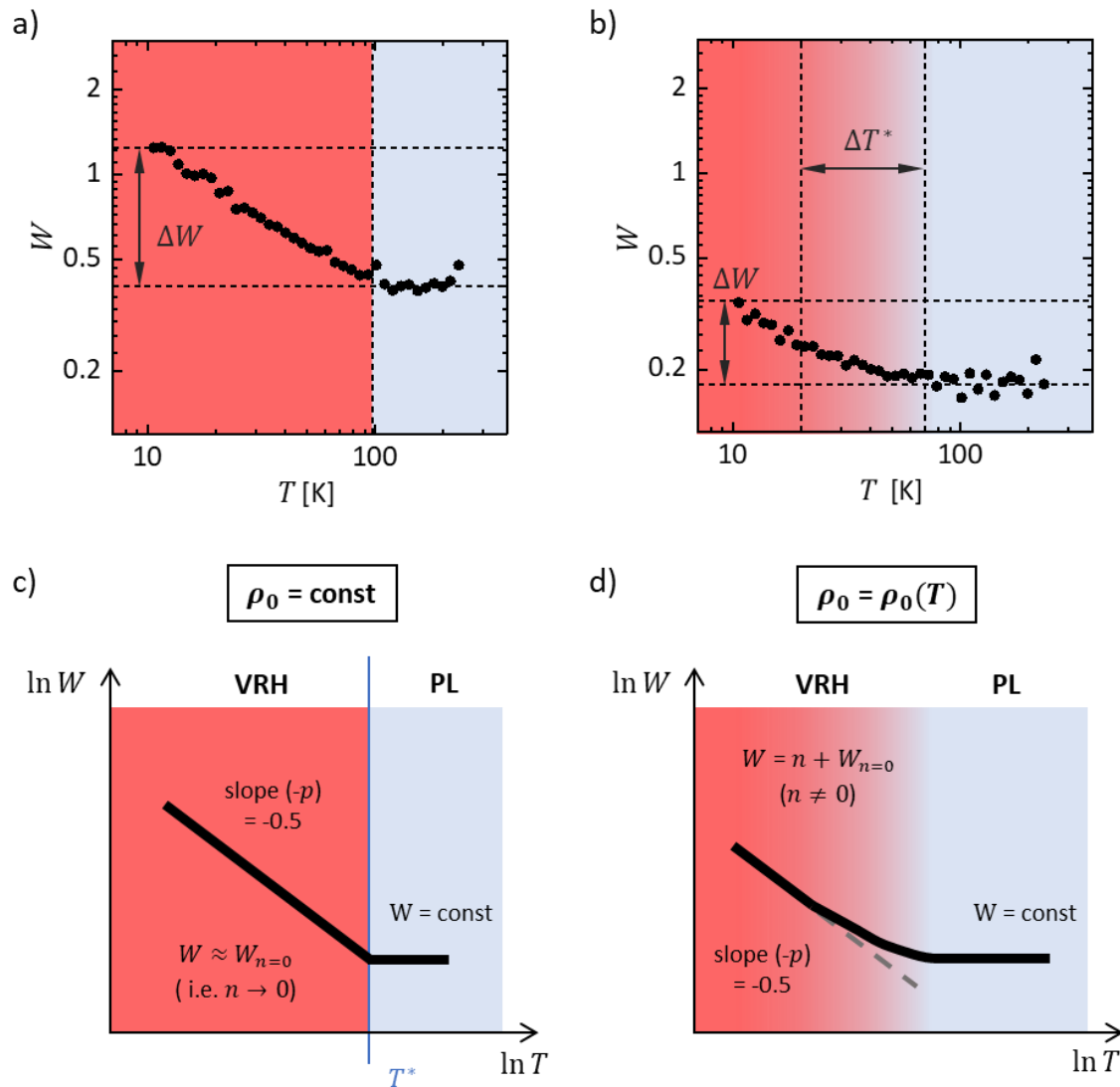


Figure 6-1. Experimental $\ln W(\ln T)$ curves of two RGO thin films. In (a), a large variation of reduced activation energy ΔW occurs at low T and the transition between another regime is clearly defined. In (b), the variation ΔW at low T is instead small. Hence, it exists a corresponding region ΔT^* where the transition is poorly defined. A sketch of the two situations is depicted below: (c) ρ_0 is constant because $n \approx 0$ at low T ; and (d) $\rho_0 = \rho_0(T)$ because $n \sim W_0$.

systems. However, the experimental measurements agree with this approach only in the case of inorganic semiconductors. For self-organized carbon networks, Govor et al. [98] reported a value of n between 1.20 and 0.04, where n decreases with room temperature resistivity.

We can treat this issue with a systematic $W(T)$ analysis. By combining equations 6-1 and 6-4 we obtain the general formula for describing the VRH regime:

$$\rho(T) = \rho_0(T) \cdot f(T) = \rho'_0 \cdot \left(\frac{T_n}{T}\right)^n \cdot \exp\left\{\left(\frac{T_0}{T}\right)^p\right\}, \quad (6-5)$$

where $f(T)$ represents the VRH resistivity given in eqn. 6-1 (*i.e.* $n=0$ case). The corresponding eqn. 6-2 then takes the form:

$$W(T) = n + p \cdot \left(\frac{T_0}{T}\right)^p. \quad (6-6)$$

Since equation 6-6 has not analytical solution in the $\ln W$ vs. $\ln T$ plot, we propose a new approach to decouple the two temperature dependences in ρ . Consider the logarithmic form of eqn. 6-6:

$$\ln W = \ln W_{n=0} + \ln\left(1 + \frac{n}{W_{n=0}}\right), \quad (6-7)$$

where $W_{n=0} = p \cdot \left(\frac{T_0}{T}\right)^p$. The two terms in eqn. 6-7 correspond to the two features in the $\ln W$ vs. $\ln T$ plot: the linear and nonlinear contributions, respectively.

When n is small with respect to $W_{n=0}$, the term $n/W_{n=0}$ can be neglected and eqn. 6-7 simplifies to: $\ln W \approx \ln W_{n=0}$. Graphically, the non-linear term can be neglected and $W(T)$ shows a linear trend in a log-log plot. The VRH electrical resistivity is fully described by the exponential term and the pre-factor ρ_0 is temperature-independent. This case is described in Figure 2-4b (Chapter 2), where the behaviour of $W(T)$ behaviour across the charge transport regimes is described by a broken line: a negative slope for VRH and a constant value for PL. The transition between the two regimes is localised at a given transition temperature T^* .

Otherwise, when n is comparable to $W_{n=0}$, the term $n/W_{n=0}$ cannot be neglected. Using the first order approximation of the Taylor series ($n < W_{n=0}$), equation 6-7 can be written as:

$$\ln W \approx \ln W_{n=0} + \frac{n}{W_{n=0}} = -p \cdot \ln T + A + \frac{n}{p} \cdot \left(\frac{T}{T_0}\right)^p \quad (6-8)$$

The second equality refers to the VRH model of eqn. 6-5 and although a detailed analysis of the analytic form is beyond the scope of this thesis, we can briefly discuss some of the results. At low temperature, the last term can be neglected and eqn. 6-8 becomes linear with negative slope in the log-log plot. With increasing temperature, a positive term adds to the linear one resulting in a sub-linear trend.

These two cases are shown in Figure 6-1c,d, where the calculated trend shows excellent agreement with the experimental data (Figure 6-1a,c) clearly indicating that ES-VRH can fully describe the measured $W(T)$ data without invoking other charge transport regimes. Unlike the case in Chapter 2, when n is not negligible (*i.e.* the VRH pre-factor only depends weakly on temperature) a simple and straightforward assignment of the parameters n and T^* from the experimental data is not possible because of the complex analytical behaviour of the equations.

6.2 Operative Approach for Fitting Analysis

The use of an analytical approach by Taylor series expansion is, however, not practical for fitting the experimental data. An interpretative problem is associated with an operational problem, as the series expansion does not allow a clear analysis of the physical meaning of the fitting parameters. We overcome such issue by developing an analysis protocol to apply to the experimental results discussed in Chapter 7.

The aim is to linearize the mathematical problem in order to calculate a clear value of the n parameter while dealing with experimental data. For this reason, we start from the simplest equation among those developed above and, in particular, we analyse equation 6-6 which clearly shows a straight line when plotted as $\ln(W - n)$ vs. $\ln T$.

For all the RGO networks we showed that the value of p value amounts to $\frac{1}{2}$, unambiguously indicating that the charge transport is described by the ES-VRH regime. We use this information to decouple the two terms in eqn. 6-6. Thus, by using $p = \frac{1}{2}$, the activation energy of eqn. 6-6 becomes simply:

$$W(T) = n + \frac{\sqrt{T_0}}{2} \cdot \frac{1}{\sqrt{T}} \quad (6-9)$$

which clearly shows a linear trend as W vs. $1/\sqrt{T}$; the values of n and T_0 can then be obtained from the y -intercept and the slope, respectively.

Figures 6-2a,b depict the experimental $W(T)$ of Figure 6-1 with the linear fits performed using eqn. 6-9.

The T_0 values calculated from the linear fit analysis were (54 ± 5) K and (3.6 ± 0.5) K, respectively, in agreement with expected values. Similarly, the n values were 0.00 ± 0.03

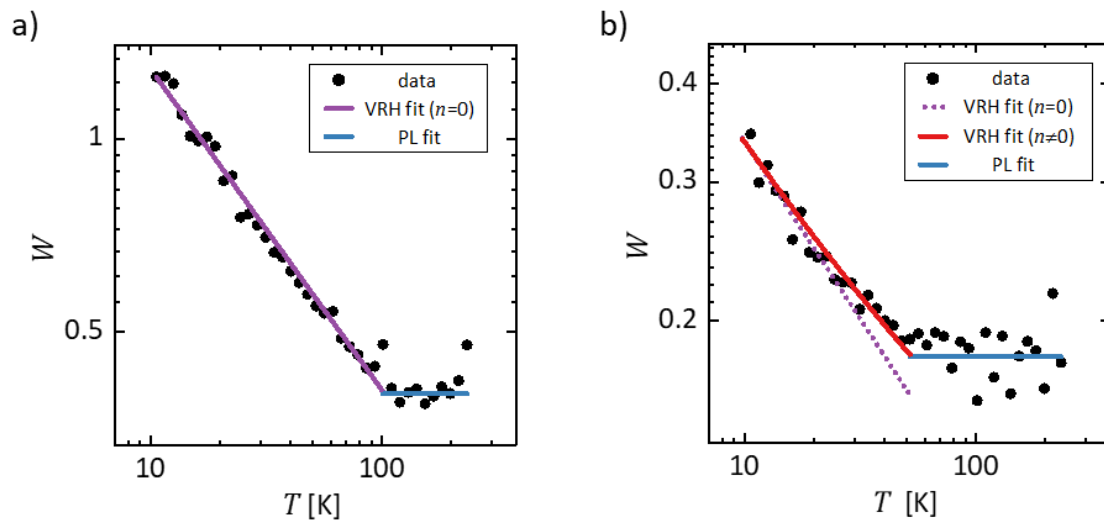


Figure 6-2. $\ln W(\ln T)$ curves for two RGO thin films with fits according to the analysis protocol explained in the text. (a) RGO sample having a large variation of ΔW at low temperatures and $\rho_0 = \text{const}$; (b) RGO sample in the opposite case with $\rho_0 = \rho_0(T)$. In the latter, the developed protocol is needed and the VRH fit with $n=0$ (violet dotted line) cannot follow the measured data.

and 0.05 ± 0.01 , respectively. It should be stressed that, in the case of $n=0$, the confidence interval does not allow one to clearly discriminate it with respect to the $n \neq 0$ situation. This statistical aspect will be discussed in more detail in the last part of this chapter.

The direct estimation of n , given by the linearization of eqn. 6-6, allows to analyse quantitatively the experimental data in the $\ln(W - n)$ vs. $\ln T$ plot using the same approach reported in Chapter 2 (where $n=0$) to calculate T^* , *i.e.* the transition temperature between ES-VRH and PL regimes.

Experimentally, the measured $\rho(T)$ data and the corresponding $W(T)$ curve do not show discontinuities at the transition temperature T^* between the two regimes. Thus, we make explicit the equivalence $W_{VRH}(T^*) = W_{PL}(T^*)$ generalising eqn. 2-14 where $n \neq 0$, as:

$$T^* = T_0 \left(\frac{p}{m-n} \right)^{1/p} . \quad (6-10)$$

The value of T^* can be easily calculated because all the parameters are defined. The theoretical value of the power exponent is $1/p = 2$ (ES-VRH). The initial T^* guess ($n=0$) is used to define the VRH and PL regimes in the experimental $W(T)$ data-plots, n and T_0 are

estimated by fitting the VRH regime data using eqn. 6-10 and m by fitting the corresponding PL regime data using eqn. 2-11.

6.3 Results and Discussion

We have used the developed approach to analyse the data described in Section 2.4 [66,95], and compared and discussed the results of the two approaches. All the experimental data have been fitted with the equations described in the previous section. The set of calculated values of m , T_0 and T^* parameters (marked with $n \neq 0$) have been compared with literature values ($n=0$).

For all the three data sets, we have reported two graphs in Figure 6-3: (a,b,c) parameter vs. room temperature resistivity ρ_{RT} (only for ref. [66], black dots for $n \neq 0$ and red circles for $n=0$) and (d,e,f) the corresponding correlation plot of the parameters calculated using the two approaches (open circles for ref. [66] data and open triangles for ref. [95] data). A direct confirmation of the validity of the developed model is given by the correlation plot analysis. Ideally, the estimated parameter should not depend on the approach used ($n=0$ or $n \neq 0$) and should lie on the bisector line (in blue in Fig. 6-3). This was achieved for all three parameters: the correlation plots clearly show that the data-points lie on the bisector line within the variance, and the reduced Chi-squared values (χ_v^2) calculated for the three parameters are close to unity.

Taking into account the parameter n , it is simple to generalise eqn. 2-14 of VRH-PL correlation with the following compact mathematical expression:

$$p \cdot \ln T^* + \ln(m - n) = -p \cdot \ln \xi + K \quad (6-11)$$

$$\text{where } K = p \cdot \ln \xi \cdot T_0 + \ln p$$

The right-hand side shows the localization length ξ as given by the relation $T_0 =$

$$\frac{2.8 e^2}{4\pi \epsilon_0 \epsilon_r k_B \xi} = \frac{\delta}{\xi}.$$

Figure 6-4 shows the correlation plot $\ln \xi$ vs $p \cdot \ln T^* + \ln(m - n)$, where each point corresponds to the data of each RGO network and the red line corresponds to a linear fit from eqn. 6-11. The plot shows an excellent linear behaviour, with slope = $-p_{\text{mean}} = -0.54 \pm 0.02$, in good agreement with $p = \frac{1}{2}$.

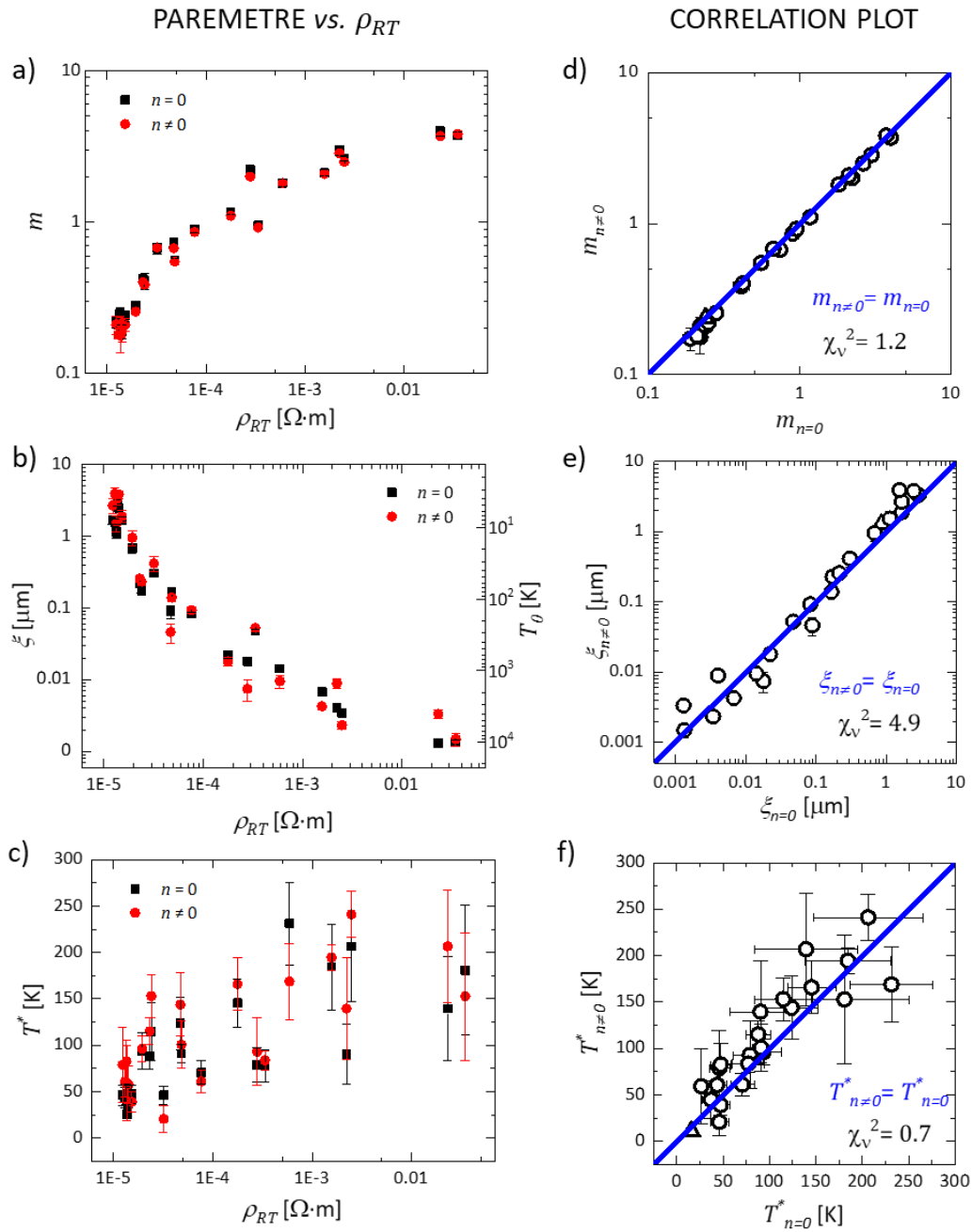


Figure 6-3. m , T_0 and T^* parameters computed considering $n \neq 0$ (from eqn. 6.9 and eqn. 6.10) for devices of ref. [66] and ref. [95]. The parameters are plotted as a function of (a,b,c) ρ_{RT} and of (d,e,f) the same quantities computed with $n=0$.

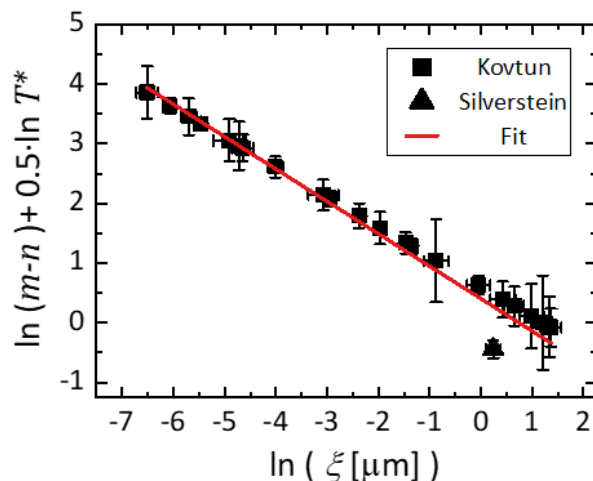


Figure 6-4. Generalised correlation plot between VRH and PL regimes of Kovtun et al data [66] (square) and Silverstein et al data [95] (triangle). The red line shows the linear fit, having slope $-p_{mean} = -0.54 \pm 0.02$.

Verified the robustness of the developed approach, we move on to discuss the experimental findings. All the estimated n values are depicted in Figure 6-5, as plotted vs. ξ . All the RGO thin films show the same n value of 0.07 ± 0.01 , independently of their oxidation state, their thickness and average sheet size. The occurrence of a unique n for all RGO films would indicate a common physical mechanism. As the localization length ξ varies among the RGO systems, the exponent n appears to be independent of ξ . However, the measured n value shows a large variability for $\xi < 100\text{nm}$, due to a large uncertainty obtained with the fitting.

A detailed analysis of this issue will be presented in Chapter 7 where we will discuss the results of more accurate $\rho(T)$ measurements obtained with the approach developed here.

We have explained the $W(T)$ features observed at low T in RGO networks by including the T dependence of the pre-exponential factor of the ES-VRH model. This scheme rules out the transition to any other VRH type of transport and/or the superposition of other CT mechanisms.

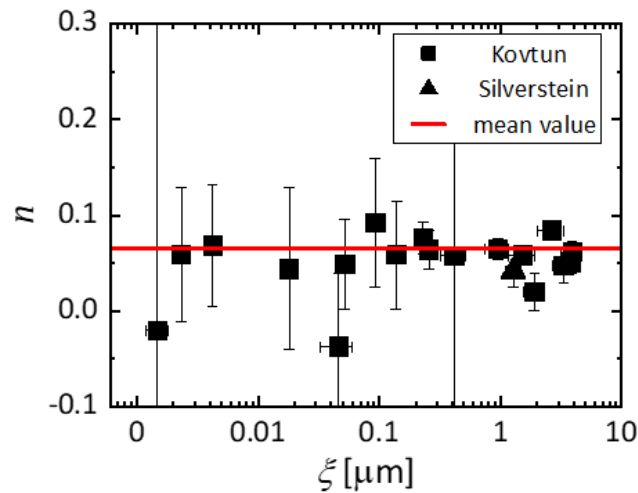


Figure 6-5. n values vs. ξ , as obtained for the data of ref. [66] (square) and ref. [95] (triangle). The red line shows the weighted mean value of 0.07 ± 0.02 . All RGO devices have a value of n compatible with the mean value, within the uncertainty limits.

6.4 References

- [66] Kovtun, A., *2D graphene-based materials: interplay between composition and electrical properties.*, PhD Thesis; Università di Modena e Reggio Emilia (2017). <https://morethesis.unimore.it/theses/available/etd-02162016-220621/>; Kovtun, A., et al., *Multiscale Charge Transport in van der Waals Thin Films: Reduced Graphene Oxide as a Case Study.* ACS Nano **15**, 2, (2021). [www.doi.org/10.1021/acsnano.0c07771](https://doi.org/10.1021/acsnano.0c07771)
- [95] Silverstein, K.W., et al., *Voltage-reduced low-defect graphene oxide: a high conductivity, near-zero temperature coefficient of resistance material.* Nanoscale **11**, 7, p. 3112-3116 (2019). [www.doi.org/10.1039/C8NR08285E](https://doi.org/10.1039/C8NR08285E)
- [98] Govor, L.V., et al., *Coulomb gap and variable-range hopping in self-organized carbon networks.* Journal of Applied Physics **90**, 3, p. 1307-1313 (2001). [www.doi.org/10.1063/1.1383021](https://doi.org/10.1063/1.1383021)
- [155] Rosenbaum, R., *Crossover from Mott to Efros-Shklovskii variable-range-hopping conductivity in InO films.* Physical Review B **44**, 8, p. 3599-3603 (1991). [www.doi.org/10.1103/PhysRevB.44.3599](https://doi.org/10.1103/PhysRevB.44.3599)
- [156] Skákalová, V., et al., *Electronic transport in composites of graphite oxide with carbon nanotubes.* Carbon **72**, p. 224-232 (2014). [www.doi.org/10.1016/j.carbon.2014.02.006](https://doi.org/10.1016/j.carbon.2014.02.006)
- [157] Shklovskii, B.I., et al., *Electronic properties of doped semiconductors*, Springer-Verlag (1984).

Chapter 7

MEASUREMENT OF GRM THIN FILM CHARGE TRANSPORT

The chapter presents charge transport measurement in RGO and EGO thin films. Results and discussion.

GRM thin films are macroscopic materials formed by the assembly of a great number of nano-objects. Generally, the geometrical structure of these materials can be described in terms of two elements: a building block and the way such nano-objects are assembled (*i.e.* network). The purpose of this Chapter is to investigate the role of these two elements in charge transport through the thin film by comparing two building blocks of different dimensionalities: RGO and EGO, as well as by arranging them in structures of varied network order (Figure 7-1). First, we study the effect of network structure using pure 2D building blocks (RGO), then CT mechanisms are investigated by varying the building block of the fabricated networks.

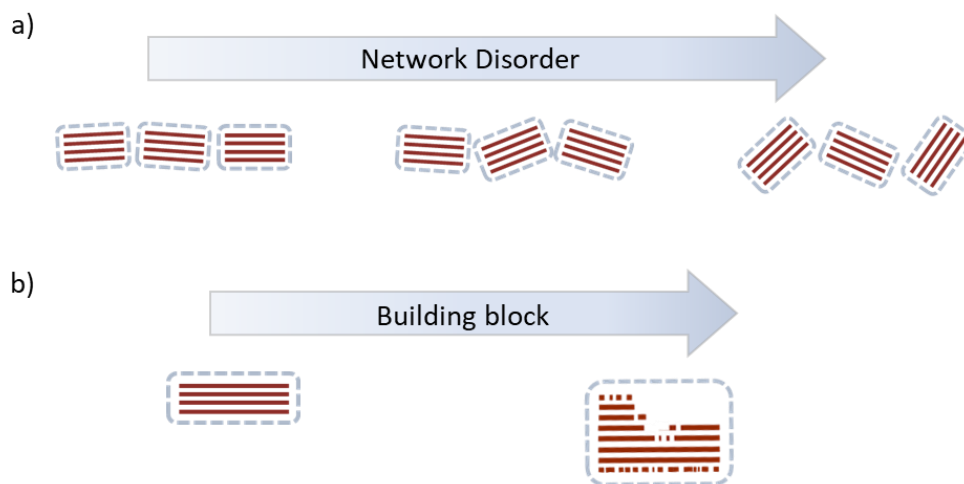


Figure 7-1. Operational scheme of present CT investigation in GRM thin films: (a) varying the network order and (b) varying the network building block.

7.1 The Role of Film Structure

We focus our attention on comparing CT in RGO thin films with different structures, fabricated with three different techniques: vacuum-assisted filtration, spray-coating and spin-coating deposition, as described in Chapter 5. The different arrangement of RGO sheets is described by two geometrical parameters: the z-coherence length (L), corresponding to the building block thickness and the mosaicity (M), indicating the average misalignment angle with respect to the stacking plane. Qualitatively, structural disorder of the film increases with M and decreases with L . This corresponds to an increase in the polycrystallinity of the thin film because the building blocks are smaller and more disorderly arranged.

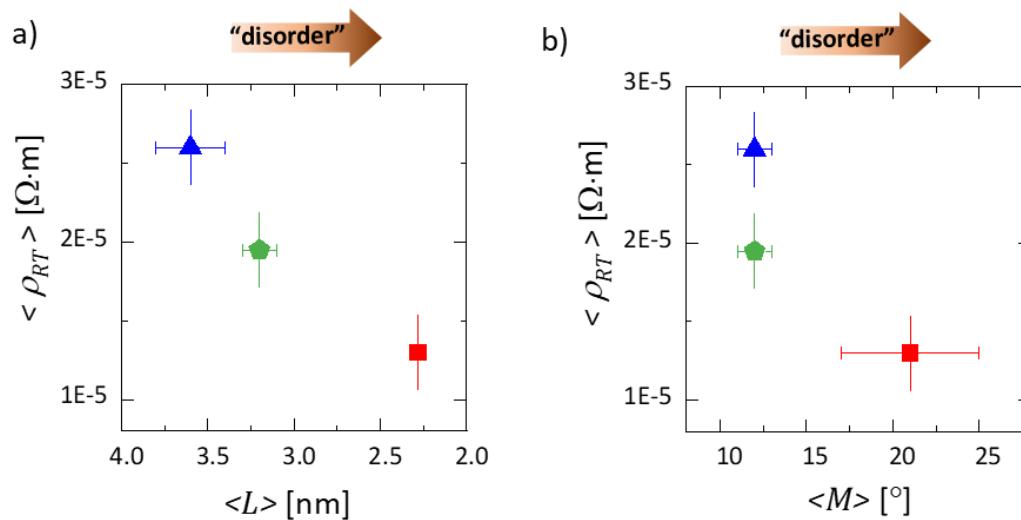


Figure 7-2. Room temperature resistivity ρ_{RT} vs. (a) z-coherence length L and (b) mosaicity M for the three types of RGO film: spin-coated (red square), filtered (blue triangle) and spray-coated (green pentagon). The faded brown arrow in both plots helps to visualize the direction of increasing structural disorder. Inserted ρ_{RT} values are the averaged values of all measured samples (for the same structure).

Figure 7-2 shows the correlation between electrical resistivity measured at room temperature ρ_{RT} and the two geometrical parameters. For each deposition technique we prepared a number of samples. We report the mean value with the corresponding uncertainty given by the reproducibility and experimental uncertainties.

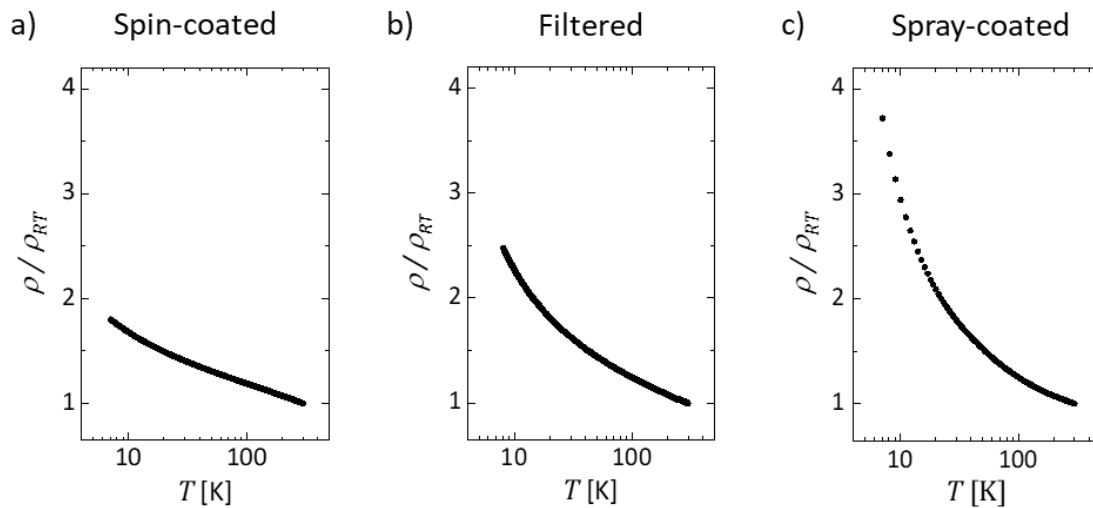


Figure 7-3. $\rho(T)$ curves of (a) a spin-coated RGO film, (b) a filtered RGO film and (c) a spray-coated RGO film. For clarity, the curves are normalised by the resistivity value $\rho_{RT} \equiv \rho(T = 297K)$.

All the thin films show a similar electrical resistivity ranging between $1 \times 10^{-5} \Omega \cdot m$ and $3 \times 10^{-5} \Omega \cdot m$. We observe that the resistivity of the film ρ_{RT} decreases with L and with increasing M corresponding to better electrical conductivity with increasing film polycrystallinity. Such a counterintuitive finding indicates a complex behaviour connecting multiscale properties of the nano-object arrangement with macroscopic electrical properties.

Thus, the charge transport in the thin films were studied by measuring the electrical resistivity vs. temperature $\rho(T)$ from 7 K to 297 K. Three representative resistivity $\rho(T)$ curves are shown in Figure 7-3, one for each deposition technique. We normalise the measured electrical resistivities to the value measured at room temperature: $\rho(T)/\rho_{RT}$. This allows better comparison and highlights possible differences in the resistivity temperature trend. In all cases, resistivity decreases with increasing temperature, clearly indicating that all the RGO thin films possess a semiconducting behaviour.

The variation of electrical resistivities over the measured temperature range is given by the relation: $\rho_r = \rho_{10K}/\rho_{RT}$, where ρ_{10K} corresponds to the electrical resistivity measured at 10 K. Taking into account the theory developed by Heeger [158] to describe the CT of

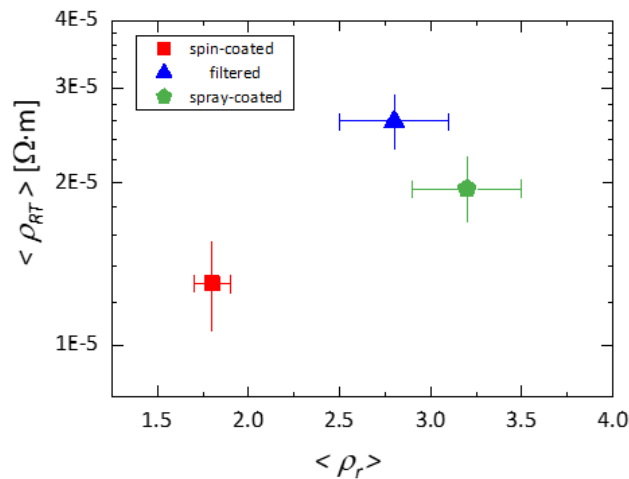


Figure 7-4. Room temperature resistivity ρ_{RT} vs. $\rho_r (= \rho(10K)/\rho(297K))$ ratio of RGO thin films.

π -conjugated conductive polymeric thin films, we define $\rho_r > 1$ as an “effective energy order parameter”: the lower the ρ_r value, the lower the energy disorder. When $\rho_r = 1$ the resistivity does not depend on the temperature. Finally, the case of $\rho_r < 1$ corresponds to metallic-like behaviour.

Spin-coated films show the lowest value: $\rho_r = 1.8$, while filtered and spray-coated films show higher values: 2.8 and 3.2, respectively. This corresponds to an opposite trend between energy disorder and structural disorder (z-coherence length and mosaicity discussed in Chapter 5). As expected, electrical properties are affected by energy disorder and the measured ρ_{RT} increases with the latter, as reported in Figure 7-4.

A quantitative analysis of the trend in the measured $\rho(T)$ curves was performed using the *Reduced Activation Energy* method, $W(T)$, as described in Section 2.2. The corresponding $W(T)$ curves are depicted in Figure 7-5.

RGO thin films produced by different deposition techniques show different $W(T)$ behaviours. Measurements were repeated for a total of eight independent samples: three each for spin-coated and filtered films and two for spray-coated films.

We can clearly identify different regimes: at low T all the samples show a linear trend corresponding to ES-VRH transport (slope = 1/2 in log-log scale), at higher T films behave differently. In the case of RGO thin films we identified two further regimes: with $30 \text{ K} < T$

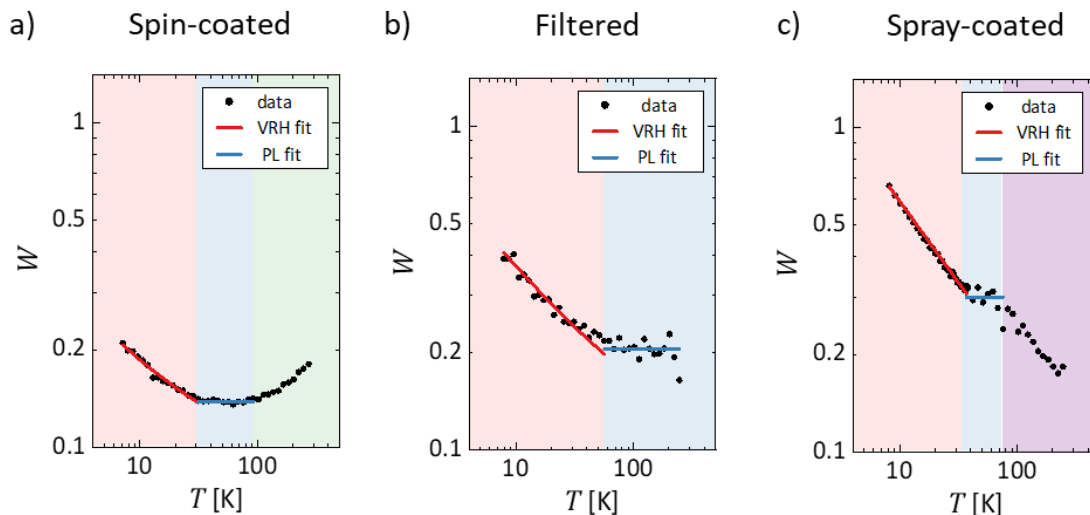


Figure 7-5. $W(T)$ in log-log space computed from the curves of Figure 6-1: (a) spin-coated RGO film, (b) filtered RGO film and (c) spray-coated RGO film. The T regions showing different CT regimes are highlighted with different colours. VRH (red) and PL (light blue) fitting lines are also reported.

< 90 K, there is PL (power law) behaviour where W is constant, and a region (with $T > 90$ K) with a positive slope indicating the presence of a thermal-induced insulator-metallic transition (MIT), as observed in polymeric thin films [85]. In the case of filtered RGO thin films, we only observed the PL regime from $T > 50$ K up to the room temperature, corresponding to the case in which the film approaches the MIT. Spray-coated thin films, however, generally show a negative slope of $W(T)$ and a rough PL regime between 35 K and 75 K. In Fig. 7-5c, the slope of -0.36 ± 0.03 for $T > 75$ K would suggest a 2D Mott type of VRH, but this observation was not confirmed in the other measured sample (with a slope of *ca.* -0.8). Thus it seems that competitive CT mechanisms are occurring at high T in spray-coated RGO films. All these findings are summarised in Table 7-1.

Since ES-VRH is observed at low temperatures for all the samples, we calculated the localization length ξ from eqn. 2-5, corresponding to the spatial localization of the charge involved in such hopping processes. In eqn. 2-5, we used a dielectric permittivity $\epsilon=3.5$ as previously reported for other RGO systems [55].

All the samples show ξ in the micrometre range and are listed in Table 7-2 at the end of this Section. For the sake of comparison, we computed the average ξ values ($\langle \xi \rangle$) for each deposition technique. $\langle \xi \rangle$ is different for each of the deposition methods: spin-coated

Table 7-1. Summary of transport regimes observed in RGO thin films by computing reduced activation energy $W(T)$.

Fabrication technique	Low T		Mid T		High T	
	T range	Transport Model	T range	Transport Model	T range	Transport Model
spin-coating	< 30 K	ES-VRH	30 K ÷ 90 K	PL	> 90 K	metal-like
filtration	< 50 K	ES-VRH	> 50 K	PL	/	PL
spray-coating	< 35 K	ES-VRH	35 K ÷ 75 K	PL	> 75 K	2D VRH + thermal activation

films have the largest $\langle \xi \rangle$ amounting to $(21 \pm 8) \mu\text{m}$; while filtered and spray-coated films have lower $\langle \xi \rangle$, $(2.6 \pm 0.9) \mu\text{m}$ and $(0.85 \pm 0.05) \mu\text{m}$, respectively. We observed some dependence of ξ on ρ_{RT} : a greater delocalisation of charges (*i.e.* a large ξ) corresponds to a better macroscopic conductivity (*i.e.* a lower ρ_{RT}).

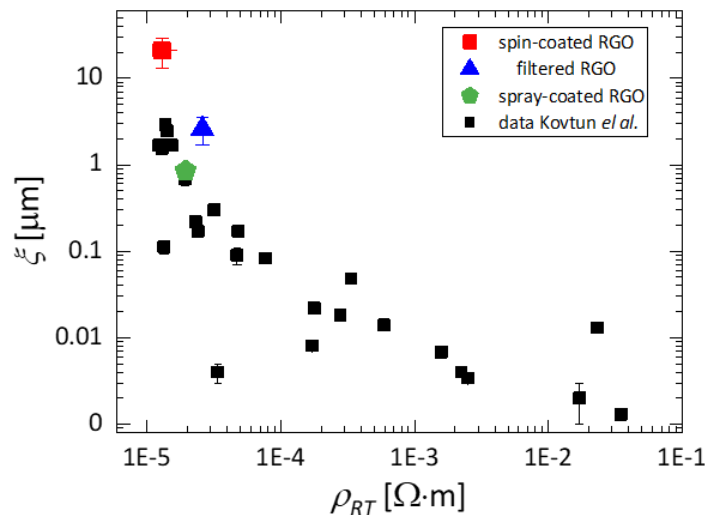


Figure 7-6. Localization length ξ vs. room temperature resistivity ρ_{RT} of the different RGO thin films. Black squares correspond to data of ref. [66]. For samples measured in this work, the reported ξ and ρ_{RT} are the averaged values.

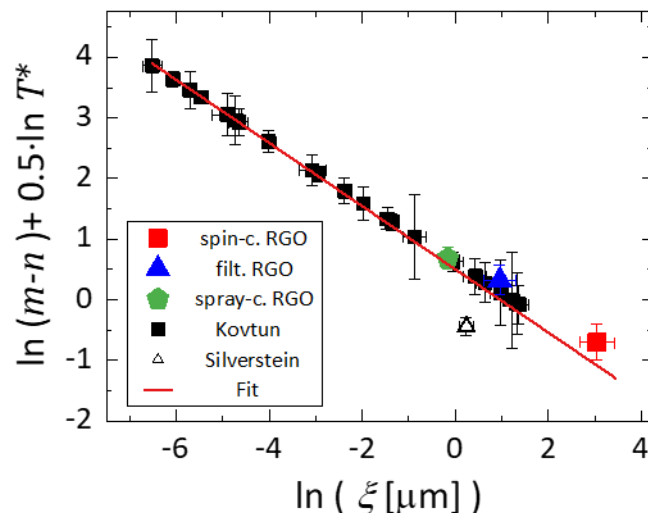


Figure 7-7. Generalised correlation plot between VRH and PL regimes (see eqn. 6-11). Current RGO film data are inserted together with Kovtun et al data [66] (square) and Silverstein et al data [95] (open triangle). The red line shows the linear fit, having slope $-p = -0.52 \pm 0.02$.

Such a trivial result is better explained by plotting the values of ξ obtained here with those in reference [66], as shown in Figure 7-6 as a function of ρ_{RT} . We immediately see that our values follow the ξ vs. ρ_{RT} trend of RGO thin films of varying thickness and oxidation state. The same data - ours plus literature data on RGO films - also fit linearly with the generalised relationship which correlates the VRH and PL regimes (see eqn. 6-11). This is shown in Figure 7-7, where the red fitting line has a slope $= -0.53 \pm 0.02$ in accordance with the ES-VRH model. Therefore, we can describe the CT in RGO networks with low structural order using the geometrical model (*i.e.* spaghetti-like model) employed previously for RGO thin films (see Section 2.4). RGO networks are modelled as composite materials with quasi-1D conductive nanofillers of length ξ , given by the superposition of inter-sheet sp^2 clusters.

Thus, we correlate the localization length with the geometrical parameters describing the structural disorder of the thin films: z-coherence length (L) and mosaicity (M), as shown in Figure 7-8a,b.

We observe two distinct situations: spin-coated films show a large ξ due to higher structural disorder (small L and quite large M); whereas spray-coated and filtered films have a smaller ξ having more structural order (larger L and not so large M).

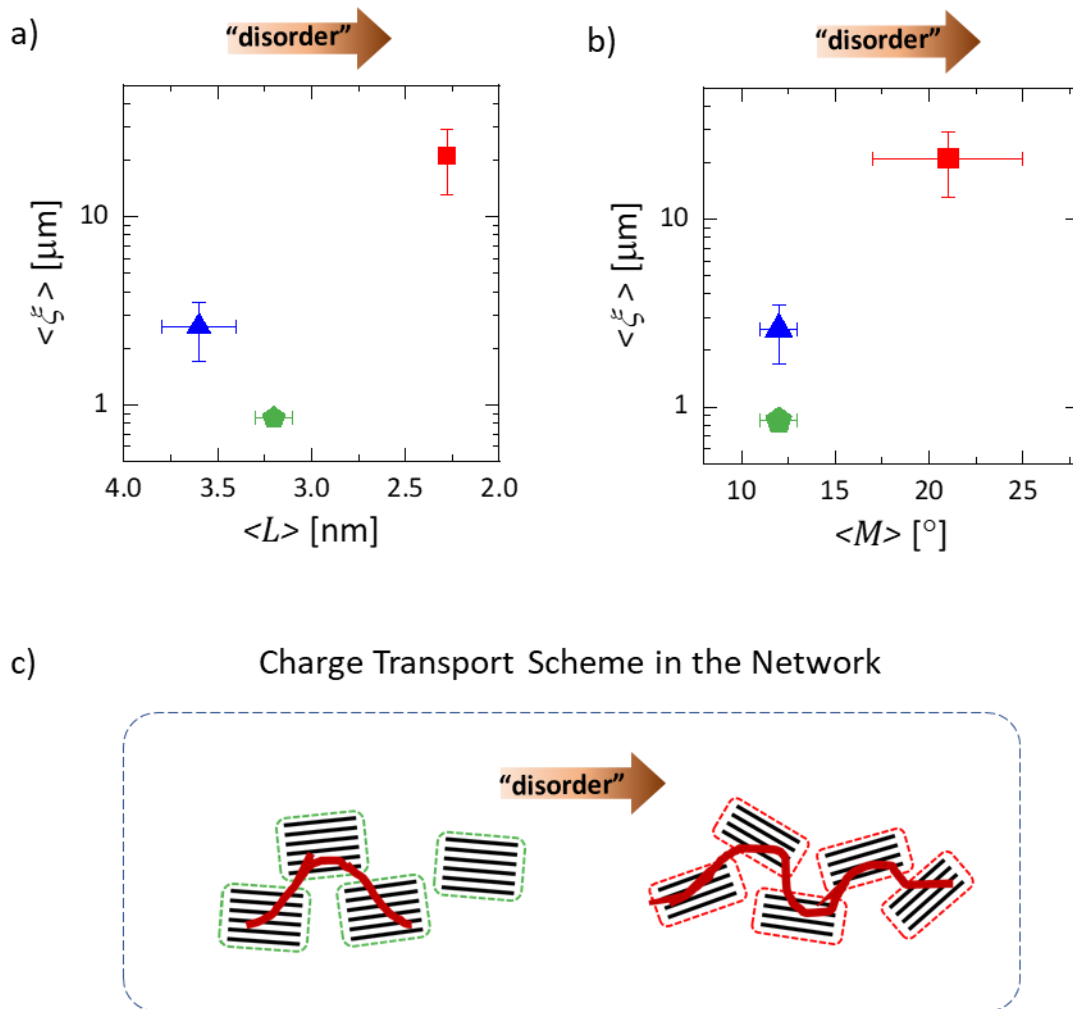


Figure 7-8. Localization length ξ as a function of the geometrical parameters – (a) z-size domain L and (b) mosaicity M - for the three RGO thin films: spin-coated (red square), filtered (blue triangle) and spray-coated (green pentagon). We plotted the average values for each deposition technique. The arrow points towards increasing structural disorder.

(c) Scheme of CT in the network structure. For all kind of studied RGO films, ξ spans over different building blocks: charge carriers are delocalized along a wire of length ξ , that it is depicted with a wine line.

An important conclusion is that the ξ -long, conductive domains span over several building blocks, independently of the structural order, as schematised in Figure 7-7c.

Moreover, generally the larger the polycrystallinity of the network, the more delocalised are the carriers. Such a result is unexpected: well stacked graphitic planes should conduct better, as in graphite. On the other hand, as noted for ρ_{RT} , the multi-scale complexity of the network can lead to multiple possible conducting paths. Indeed, networks with less mis-oriented and thicker building blocks will have more voids (*i.e.* non conducting regions

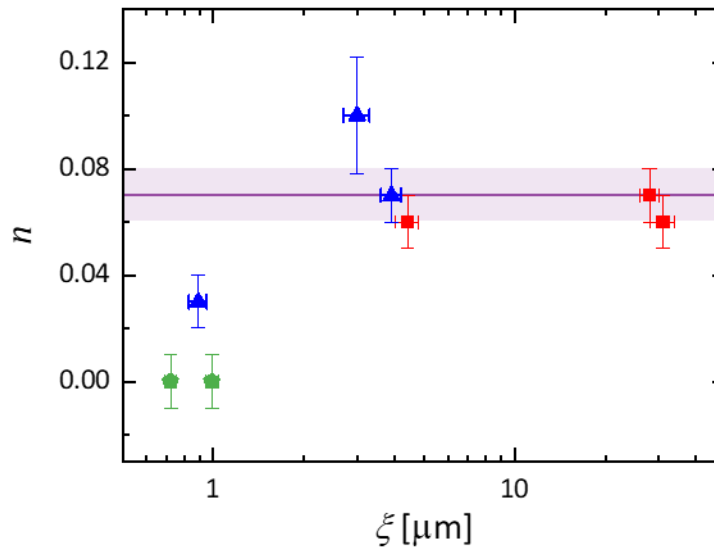


Figure 7-9. Pre-factor exponent n vs. localisation length ξ for the measured RGO thin films: spin-coated (red square), filtered (blue triangle) and spray-coated (green pentagon). The shaded purple region represents the constant value ($=0.07 \pm 0.01$) obtained for RGO devices of ref. [66] in Chapter 6.

in the geometrical model), which interrupt the conducting path, compared to smaller building block structures with larger mis-alignments. Continuing the analogy for composite materials, the latter present higher surface areas. In the geometrical model for RGO systems, the enhanced delocalisation is related to the overlapping of sp^2 clusters in different sheets and the transport is dominated by interfaces (*i.e.* in-plane sheet surfaces). Thus, structural disorder increases the total surface area of the system and, in turn, increases the delocalisation of charge carriers.

We have seen that resistivity ρ shows a small variation with T in RGO current networks. For this reason, they are valid candidates for studying the temperature dependence of the pre-exponential factor in VRH transport. We followed the protocol developed in Chapter 6 assuming a T power law for VRH pre-factor with exponent n (see eqn. 6-4). Then, we computed n for the eight RGO samples.

n values against ξ are plotted in Figure 7-9. At relatively low ξ values, n is close or equal to 0; with increasing ξ , n increases and tends to a constant value which is comparable to that calculated for RGO systems in Section 6.3. Moreover, because clusters of the same colour (*i.e.* networks with similar structures) are not visible in the plot of Fig. 7-9, and n seems independent of the complexity of the RGO network. The latter result indicates that

the *spaghetti-like* geometrical scheme that models CT in RGO systems could also be independent of network complexity.

In the literature there is no general consensus about the underlying physical mechanism giving rise to the pre-factor power law behaviour. From the theoretical point of view, the exponent n depends on the details of electronic DoS and on the properties of the phonon subsystem in the material [159]. On the other hand, n calculated using scaling approaches contains a dependence upon the critical exponent (ν) of the correlation radius in a random resistance network [157].

To determine its analytical form, the wave function of the electronic state could be taken equal to a power-cut exponential [160], in analogy with a system of charge that screens the charge carriers:

$$F_i(\mathbf{r}) \sim \frac{e^{-|\mathbf{r}-\mathbf{r}_i|/\xi}}{|\mathbf{r}-\mathbf{r}_i|^\zeta} . \quad (7-1)$$

\mathbf{r} and \mathbf{r}_i are the positions wherein the potential is evaluated and of the i -th charge carrier (*i.e.* the energy level where it is located), respectively. ζ is a constant value that characterizes the strength of the screening. For instance, ζ is 0 for a hydrogen-like wavefunction and it is 1 for a screened, short-range wavefunction. By computing the transition probability, the exponent n is then expressed as function of ζ as

$$n = (4 \zeta + \nu - 2) \cdot p . \quad (7-2)$$

The formula agrees with the two equations reported explicitly by Shklovskii's monography [157]. The relation thus becomes $n = \frac{\nu-2}{4}$ for the Mott 3D scheme of VRH ($\zeta=0$, $p=1/4$) and $n = \frac{\nu+2}{4}$ for an amorphous system with larger charge screening ($\zeta=1$, $p=1/4$). As $\nu > 0$, it is immediately evident that n can be positive or negative based only on the system being studied.

In our RGO networks, the large ξ ($\gtrsim 1 \mu\text{m}$) observed indicates that the wavefunction cannot be highly screened. On the other hand, the characterisation data discussed in Section 5.1 highlight a system where defects, both chemical and topological, are still present. Combining these two considerations, a ζ value equals to a fraction of unity is plausible.

Table 7-2. Fits parameters of $W(T)$ obtained for all RGO thin films measured in this work.

Fabrication technique	Sample Name	ρ_{RT} [$10^{-5} \Omega \cdot m$]	T^* [K]	n	T_0 [K]	ξ [μm]	m
spin-coating	s1	0.9 ± 0.1	31 ± 5	0.07 ± 0.01	0.50 ± 0.04	28 ± 2	0.14 ± 0.01
	s2	1.5 ± 0.2	26 ± 5	0.06 ± 0.01	0.45 ± 0.05	31 ± 3	0.12 ± 0.03
	s3	1.4 ± 0.1	49 ± 10	0.06 ± 0.01	3.1 ± 0.3	4.4 ± 0.4	0.18 ± 0.01
filtration	f1	2.9 ± 0.3	28 ± 5	0.10 ± 0.02	4.7 ± 0.5	3.0 ± 0.3	0.30 ± 0.04
	f2	2.8 ± 0.3	57 ± 10	0.07 ± 0.01	3.6 ± 0.3	3.9 ± 0.3	0.21 ± 0.02
	f3	2.2 ± 0.2	92 ± 14	0.03 ± 0.01	16 ± 1	0.89 ± 0.06	0.23 ± 0.01
spray-coating	spr1	2.2 ± 0.2	40 ± 5	0.00 ± 0.01	14.0 ± 0.5	0.99 ± 0.01	0.30 ± 0.02
	spr2	1.7 ± 0.2	32 ± 5	0.0	19 ± 1	0.72 ± 0.01	0.36 ± 0.05

For $\zeta=0.2$ and using $\nu = 1.4$ [73] and $p=0.5$ (for ES-VRH), n becomes 0.1, compatible with our observed value of 0.07.

Now, we should try to explain why n is negligible for low ξ values (see Fig. 7-9). In low-dimensional systems such as carbon nanotubes, it has been reported that ν depends on the aspect ratio (AR) of the conducting structure [161]. In particular, ν is close to 2 for spherical objects and then decreases with an increase in the object aspect ratio. For instance, ν can be less than 1.4 for AR greater than 1000. In the geometrical model for RGO charge transport, the conducting structure can be a wire of length ξ and of transversal size corresponding to the average extension of RGO aromatic domains (*i.e.* several nm). Thus, the aspect ratio of conducting domains in RGO networks can be tuned mainly by the varying ξ . At low ξ values, the critical exponent ν could vary as well as the exponent n . However, the scheme proposed for nanotubes would predict an opposite behaviour of n : the exponent n increases as ξ decreases. To sum up, the dependence of the critical exponent ν upon the nano-object dimensionality is an interesting point but does not fully explain our observations.

7.2 The Role of Film Building Block: EGO vs. RGO

Having discussed the effects of network disorder on CT, we can proceed by studying the electrical behaviour of films fabricated with a different building block material: EGO. For this kind of film, the two geometrical parameters – L and M – amount to *ca.* 8.8 nm and 6.0° , respectively. Such values correspond to thicker and less-misaligned building blocks, or smaller polycrystallinity, compared to any type of RGO network investigated.

The measured room temperature resistivity ρ_{RT} of EGO films is $(11\pm 1)\times 10^{-5} \Omega\cdot\text{m}$. The ρ_{RT} value is 4 to 10 times greater than in the RGO networks. This observation confirms the counter-intuitive result for which a smaller polycrystallinity of the network corresponds to a larger ρ_{RT} and to a lower macroscopic, electrical conduction (see Fig. 7-2 for comparison). Moreover, ρ_{RT} in EGO agrees well with the higher presence of chemical functional groups compared to RGO (C sp^3 of 11% against *ca.* 4%).

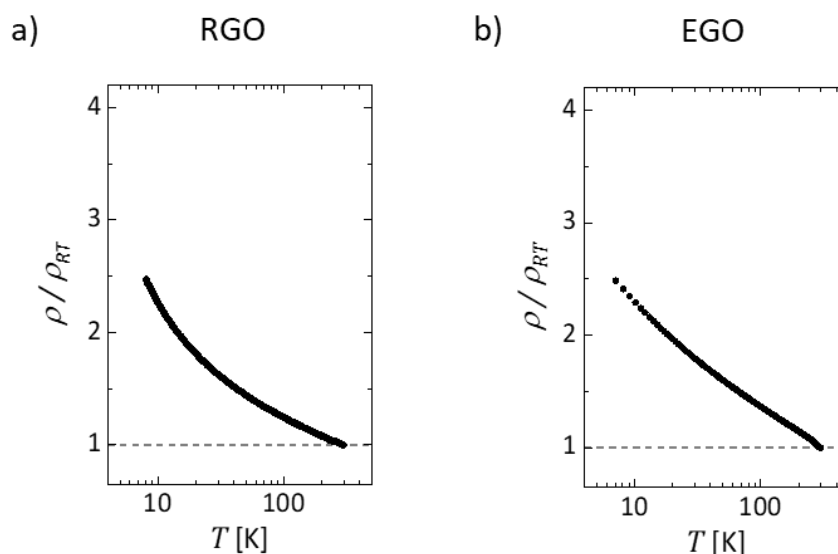


Figure 7-10. $\rho(T)$ curves of filtered GRM thin films made with different building blocks: (a) RGO and (b) EGO. For clarity, the curves are normalised by the resistivity value $\rho_{RT} \equiv \rho(T = 297\text{K})$.

Again, we performed resistivity ρ vs. T measurements from 7 K to 297 K to investigate CT mechanisms in EGO networks.

In Figure 7-10, the $\rho(T)$ curve of an EGO thin film is shown. For the sake of clarity, we also report $\rho(T)$ of a filtered RGO film. The $\rho(T)$ trend in the EGO film is similar to that in RGO

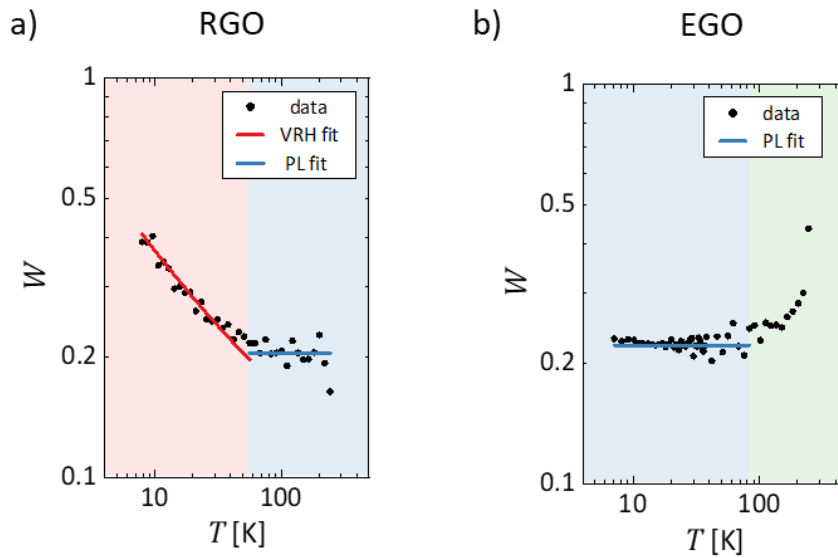


Figure 7-11. $W(T)$ in log-log space: (a) filtered RGO film and (b) EGO film. Data are computed from the $\rho(T)$ curves of Figure 7-10.

samples: ρ always increases with decreasing temperature, corresponding to an overall semiconducting nature of the system. The $\rho_r = \rho_{10K}/\rho_{RT}$ ratio of EGO, amounting to 2.3, is also close to RGO values. However, the curvature of the $\rho(T)$ plot toward higher resistivity is more marked in RGO with respect to EGO.

The activation energy scheme was also applied to EGO thin films, as for the RGO samples. The resulting $W(T)$ in log-log is shown in Figure 7-11b. The benefits of W are immediately evident by comparing the EGO curve with the previous RGO film curve: while their $\rho(T)$ values are qualitatively very similar, their $W(T)$ show quite different features, suggesting different transport regimes. In the EGO film, W is constant from a few K to around 80 K (“low T ” region) then increasing in log-log space for larger T . The invariant W in the “low T ” region highlights temperature power law functionalities, as opposed to the ES-VRH of RGO films. The value of m , 0.22 ± 0.03 , is compatible with a transition of the system to a critical regime. Furthermore, m is also comparable with that of RGO in the “mid T ” region, showing a common transport mechanism occurring over different temperature ranges. This result indicates that CT can be described by the same *spaghetti-like*, geometrical model used for RGO films, despite the lack of ES-VRH transport in $W(T)$ and the

Table 7-3. Comparison of transport regimes observed in EGO and RGO filtered, thin films by computing reduced activation energy W . The values for RGO corresponds to the ones in Table 7-1.

System	Low T		High T	
	T range	Transport Model	T range	Transport Model
EGO	< 80 K	PL	> 80 K	metal-like
RGO	< 50 K	ES-VRH	> 50 K	PL

impossibility of estimating ξ in EGO films. In fact, PL and ES-VRH transport regimes are coupled in RGO networks.

In the “high T ” region of W , a pure phonon-limited (metal-like) conduction [162] is ruled out by the $\rho(T)$ behaviour in the EGO films. Instead, the increase in activation energy with T could be caused by low-frequency phonons which, together with impurities and sheet edges, scatter charge carriers, as is typically observed in granular metals [85,163].

Because of the different CT regime at high T between RGO and EGO, we propose the two systems as two phases of the same metal-to-insulator geometrical transition: with the RGO film approaching the transition from insulating (*i.e.* semiconducting) state, and the EGO film from the metallic state. A similar phenomenology in proximity to the metal-to-insulator transition has already been observed in other carbon network structures [27] and conducting polymers [164]. However, in those works the macroscopic conductivity correlates with increasing local order in the structure. We envisage that the two geometrical elements in our films explain the data: the building block influences the electrical nature of the systems - *i.e.* semiconducting or metal state of the MIT; while the network disorder is responsible for the observed macroscopic room temperature resistivity ρ_{RT} , as discussed above for RGO. All the observed regimes are summarised in Table 7-3.

Additionally, we performed electrical noise measurements of both thin film types (EGO and RGO) to improve the understanding of transport mechanisms in the different regimes. Unlike $\rho(T)$ measurements, it is sufficient to measure the noise only at a few relevant temperature values.

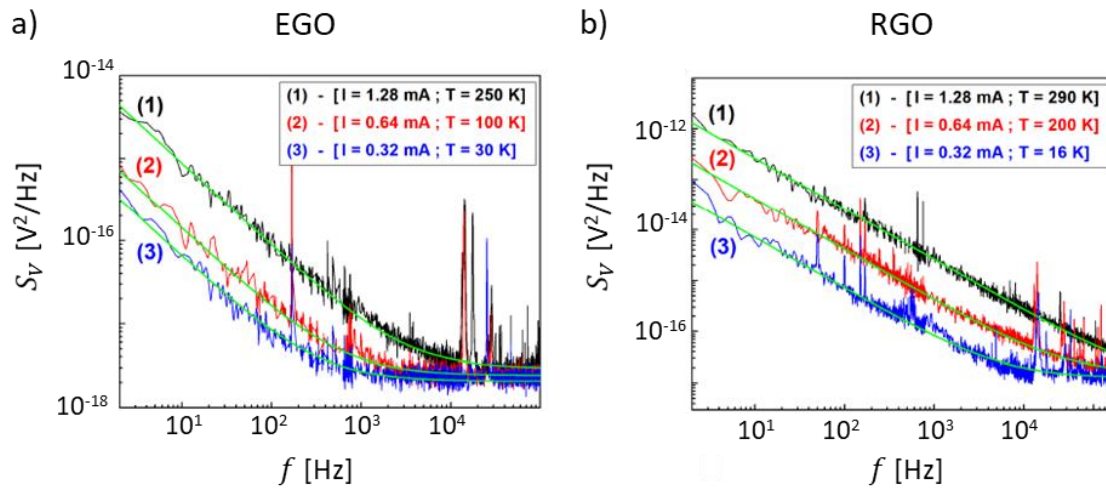


Figure 7-12. Spectral power density S_V versus frequency f for (a) EGO film and (b) RGO film. The different coloured lines represent spectra acquired at different temperature and inject current values. All the $S_V(f)$ signals show a common shape: a $1/f$ dependence at low frequencies and a f independence (S_{white}) at high frequencies.

The measured power spectral density S_V versus frequency is presented in Figure 7-12 for the two GRM films. Independently of film type, S_V is characterized by the presence of two components: $1/f$ (*i.e.* flicker) noise at low frequencies ($f < 10^3 \div 10^4$ Hz) and “white” noise S_{white} in the high-frequency range. The latter component is the frequency-independent noise caused by the sum of thermal, shot and background noise contributions. Moreover, the S_V behaviour was observed at all investigated bias current values (up to 1.28 mA) and over the whole temperature range, from 16 K to 290 K. Overall, we found that the noise signal S_V is at least two orders of magnitude lower in EGO with respect to RGO. Concerning the electrical nature of the samples, a lower $1/f$ amplitude is typical of metal systems compared to semiconducting ones [142]. This result suggests the proximity at high T to a metallic phase for EGO films, as observed in $W(T)$ analysis.

We used the following functional form to separate the two noise contributions in S_V

$$S_V(f) = \frac{K(I,T)}{f} + S_{white} \quad (7-3)$$

Figures 7-13a,b show the two components obtained as a function of applied current I , for different temperatures. As expected, the “white” noise component is almost current-

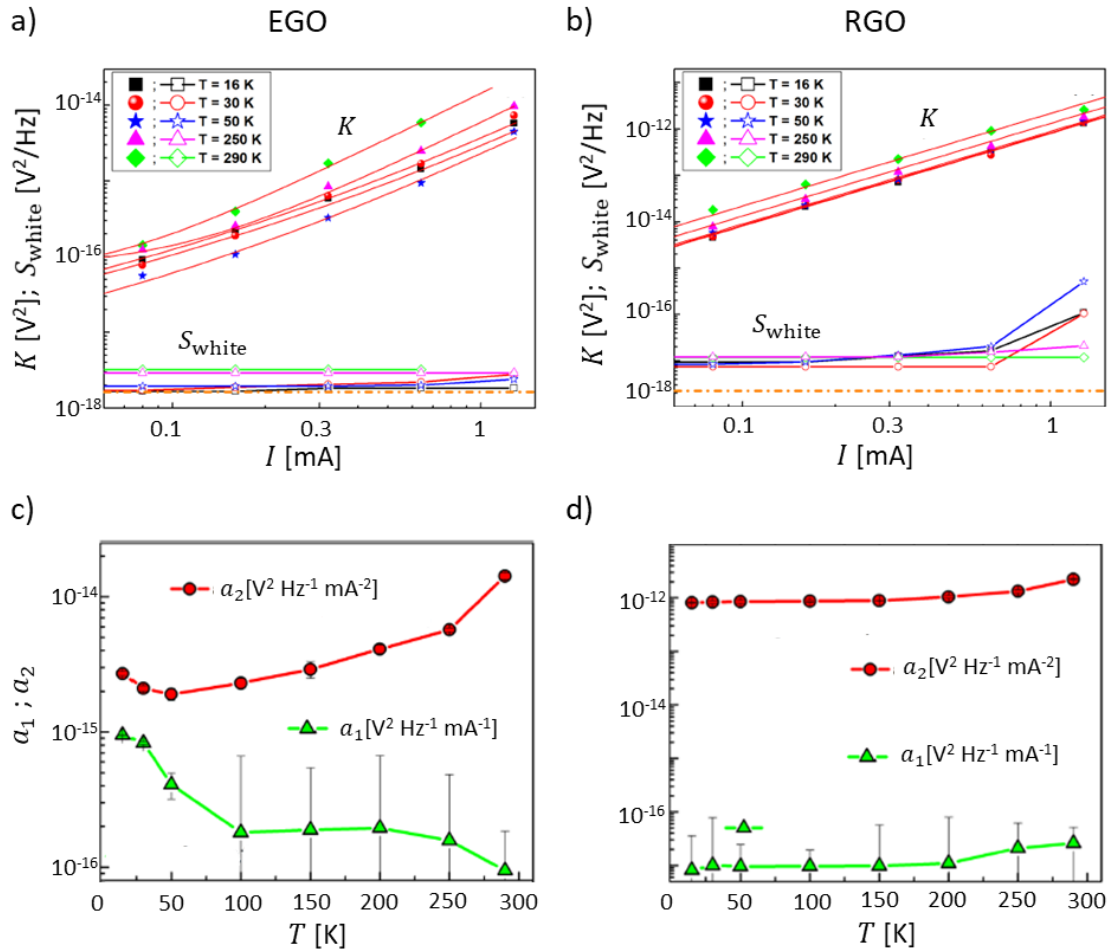


Figure 7-13. Experimental values and fits of noise components. (a) and (b) depict the flicker noise amplitude K and the white noise term S_{white} vs. the injected current I . The different marks represent signals acquired at different temperatures, from 16K to 290K. $K(I)$ is fitted with a second order polynomial (red line). In (c) and (d), the quadratic coefficient a_2 and the linear coefficient a_1 of $K(I)$ are plotted as a function of temperature.

The plots in (a) and (c) are for the EGO film, the ones in (b) and (d) for the RGO film.

independent. The amplitude K of $1/f$ noise, however, increases with I in both systems. Hence, we focus on the $1/f$ component because it carries useful information about CT. The functional form of $K(I)$ can be described with a second-order polynomial:

$$K(I) = a_2 \cdot I^2 + a_1 \cdot I + a_0 \quad (7-4)$$

By fitting the $K(I)$ signal with eqn. 7-4 at different temperatures, CT mechanisms can be studied. In Figures 7-13c,d, quadratic (a_2) and linear (a_1) coefficients of K vs. temperature are presented for EGO and RGO films, respectively. For both films, a_2 is always different

from zero over the investigated temperature range. It monotonically increases with T in the filtered RGO film, while in the EGO film it slightly decreases up to 50K and then it starts to increase with T . In the EGO film, a_1 is always zero except below 50K. The anisotropy of scattering cross sections between different impurities in the films, as well as different interference patterns for charges in the film network can cause the resistivity fluctuations which lead to the non-vanishing values of a_2 [142]. However, the behaviour of K coefficients in EGO is peculiar and not commonly found in other thin films [165]: a_1 behaviour suggests that weak localization effects contribute to ρ below 30 K; while, because a_2 does not vanish below 30 K, one or more mechanisms superimpose to weaken localization to give the power dependence. These results are not in contradiction for what was observed in $W(T)$ of the EGO film: a superposition of interference transport mechanisms can explain the less than perfect constancy of W and the departure (of around 6%) from pure PL transport below *ca.* 10 K (see Fig. 7-11b).

Further magneto-resistance measurements could be helpful to fully unravel the nature of transport in EGO flake networks.

To summarise, the *spaghetti-like* geometrical model used for RGO systems can be extended to EGO. Within this framework, the EGO film moves towards a metallic phase with an elevated concentration of coupled conductive wires [105].

Moreover, noise measurements show that weak localisation effects are superimposing to produce the critical transport in EGO films for $T < 30$ K.

7.3 References

- [27] Takai, K., *et al.*, *Structure and electronic properties of a nongraphitic disordered carbon system and its heat-treatment effects*. Physical Review B **67**, 21, p. 214202 (2003). www.doi.org/10.1103/PhysRevB.67.214202
- [55] Joung, D., *et al.*, *Efros-Shklovskii variable-range hopping in reduced graphene oxide sheets of varying carbon $\$s\{p\}^{\{2\}}\$$ fraction*. Physical Review B **86**, 23, p. 235423 (2012). www.doi.org/10.1103/PhysRevB.86.235423
- [66] Kovtun, A., *2D graphene-based materials: interplay between composition and electrical properties.*, PhD Thesis; Università di Modena e Reggio Emilia (2017). <https://morethesis.unimore.it/theses/available/etd-02162016-220621/>; Kovtun, A., *et al.*, *Multiscale Charge Transport in van der Waals Thin Films: Reduced Graphene Oxide as a Case Study*. ACS Nano **15**, 2, (2021). www.doi.org/10.1021/acsnano.0c07771
- [73] Shklovskii, B.I., *et al.*, *Correlation Effects on the Density of States and Hopping Conduction*, in *Electronic properties of doped semiconductors*, Springer-Verlag, (1984).
- [85] Reghu, M., *et al.*, *Metal-insulator transition in doped conducting polymers*, in *Handbook of conducting polymers*, p. 27-84 (1998).

- [95] Silverstein, K.W., *et al.*, *Voltage-reduced low-defect graphene oxide: a high conductivity, near-zero temperature coefficient of resistance material*. *Nanoscale* **11**, 7, p. 3112-3116 (2019). www.doi.org/10.1039/C8NR08285E
- [105] Prigodin, V.N., *et al.*, *Metal-insulator transition in an irregular structure of coupled metallic chains*. *Synthetic Metals* **65**, 2, p. 195-201 (1994). [www.doi.org/10.1016/0379-6779\(94\)90181-3](http://www.doi.org/10.1016/0379-6779(94)90181-3)
- [142] Kogan, S., *1/f noise and random telegraph noise*, in *Electronic noise and fluctuations in solids*, Cambridge Univ. Press, p. 239 (1996).
- [157] Shklovskii, B.I., *et al.*, *Electronic properties of doped semiconductors*, Springer-Verlag (1984).
- [158] Reghu, M., *et al.*, *Transport in polyaniline networks near the percolation threshold*. *Physical Review B* **50**, 19, p. 13931-13941 (1994). www.doi.org/10.1103/PhysRevB.50.13931; Yoon, C.O., *et al.*, *Transport near the metal-insulator transition: Polypyrrole doped with PF_6^-* . *Physical Review B* **49**, 16, p. 10851-10863 (1994). www.doi.org/10.1103/PhysRevB.49.10851
- [159] Đekić, M., *et al.*, *Variable range hopping conductivity in nanocrystalline films of $\text{K}_0.3\text{MoO}_3$* . *Thin Solid Films* **591**, p. 210-214 (2015). www.doi.org/10.1016/j.tsf.2015.04.008
- [160] Rodríguez, M., *et al.*, *Preexponential factor in variable-range hopping conduction in CuInTe_2* . *Solid State Communications* **136**, 4, p. 228-233 (2005). www.doi.org/10.1016/j.ssc.2005.07.018
- [161] Foygel, M., *et al.*, *Theoretical and computational studies of carbon nanotube composites and suspensions: Electrical and thermal conductivity*. *Physical Review B* **71**, 10, p. 104201 (2005). www.doi.org/10.1103/PhysRevB.71.104201
- [162] Pendry, L.A., *et al.*, *Electrical transport properties of natural and synthetic graphite*. *Journal of Materials Science* **15**, 8, p. 2103-2112 (1980). www.doi.org/10.1007/BF00550638
- [163] Abeles, B., *et al.*, *Structural and electrical properties of granular metal films*. *Advances in Physics* **24**, 3, p. 407-461 (1975). www.doi.org/10.1080/00018737500101431
- [164] Stadler, P., *et al.*, *Local order drives the metallic state in PEDOT:PSS*. *Journal of Materials Chemistry C* **4**, 29, p. 6982-6987 (2016). www.doi.org/10.1039/C6TC02129H
- [165] Barone, C., *et al.*, *Universal origin of unconventional $1/f$ noise in the weak-localization regime*. *Physical Review B* **87**, 24, p. 245113 (2013). www.doi.org/10.1103/PhysRevB.87.245113; Barone, C., *et al.*, *Nonequilibrium fluctuations as a distinctive feature of weak localization*. *Scientific Reports* **5**, 1, p. 10705 (2015). www.doi.org/10.1038/srep10705

Concluding Remarks and Outlook

Graphene-based materials (GRM) thin films are macroscopic assemblies of a great number of 2D building blocks. Thus, the macroscopic electrical properties depend on both the nanometre structure of the building blocks and how they assemble together on micro- and macro- scale (network). Recently, a multiscale geometrical model has been proposed to describe the charge transport in ordered RGO thin films similar to the case of composite materials where quasi-1D building blocks behave as conductive fillers in an insulating matrix (a.k.a. “*spaghetti-like*” structure). The length of the quasi-1D wires is defined by the localization length ξ of the charge carriers.

This thesis aimed to generalize this approach in order to describe the charge transport (CT) of the entire class of GRM thin films, studying the role of building blocks and their arrangement in the film.

We compared two different GRM produced at CNR-ISOF: reduced graphene oxide (RGO) and Electrochemical exfoliated Graphene Oxide (EGO) and we fabricated thin film with different arrangements using three different deposition techniques: i) spin-coating, ii) spray-coating and iii) vacuum assisted filtration. The multiscale structural analysis of the films has been performed combining X-Ray Diffraction (XRD), as well as optical (OM), Scanning Electron (SEM) and Atomic Force (AFM) microscopies. Chemical analysis (*i.e.* oxidation degree, presence of contaminants and chemical functionalization) has instead been performed using X-ray Photoelectron Spectroscopy (XPS).

Described in terms of polycrystalline system, we investigated the CT of the fabricated GRM thin films by measuring the temperature-dependence of the electrical resistivity (ρ) from room temperature down to 7 K. Data analysis have been carried out using the reduced activation energy method, $W(T)$, allowing to assign the various transport regimes in a self-consistent way. In the case of RGO we obtained an excellent agreement with the results reported in literature. In particular, due to the low signal-to-noise ratio of the acquired data we developed a generalization of the $W(T)$ approach. In this way, we showed that ES-VRH permits to describe the resistance trend at low temperature, without

invoking transitions between different VRH regimes as commonly proposed in the literature.

We found that the *spaghetti-like* structure can be fruitfully used to describe the CT in all the fabricated GRM thin films, both in the case of RGO and EGO. We observed that the localization length ξ increases with the disorder in the stacking of the building blocks (i.e. the polycrystallinity) in the network, pointing out the effects of multiscale mechanisms. The increase in disorder relates to an increase of the possible building blocks orientations and therefore, to a greater number of structural configurations. This condition corresponds to the optimization of interfaces superposition at the nanometre scale and then, to a better chance that the charges will jump between the different building blocks.

Based on a systematic and quantitative analysis of experimental data, the developed model combines concepts, approaches and results of different fields, such as graphene and 2D related materials, polymers science, networks, percolation theory and critical phenomena. The role of interfaces and their nanostructure, as well as the universal behaviour observed from the nano- to the macro- scale and the analogies with charge transport in 1D and 3D systems give to these results a far-reaching importance. In principle, the developed approach could be used to describe the CT in Van der Waals thin films and many others disordered materials, such as composites and granular materials.

Appendix A

A.1 Complements of CT Theories

Computation of VRH formula

In the following, we detail the mathematical passages that allow to obtain eqn. 2-3 for VRH transport model.

As already mentioned, the p exponent and hence the type of VRH model strongly depends on DoS $g(E)$ in the small energy interval 2δ around E_F , where charge contributing to the transport are located. A simple way to proceed is to express the DoS as a power law [157]

$$g(E) = g_0(E - E_F)^s, \quad (\text{A-1})$$

with g_0 as positive pre-factor and s as exponential term. This assumption is reasonable at low temperature – *i.e.* $k_B T$ is sufficiently small compared to the energy scale (“bandwidth”) of levels distribution. For Mott-VRH, s is 0 and the DoS is constant around E_F ($g(E) \equiv g(E_F) \equiv g_0$). Hence, we can write for a system with dimensionality d

$$g_0 \cdot \delta \cdot c_d R_{hop}^d \approx 1 \quad \text{with } c_d = \begin{cases} 1, & d = 1 \\ \pi, & d = 2 \\ \frac{4\pi}{3}, & d = 3 \end{cases}, \quad (\text{A-2})$$

where R_{hop} is the typical hopping distance of a carrier from E_F to $E_{F+\delta}$. By inverting eqn. A-2,

$$R_{hop} \approx \left(\frac{1}{c_d \cdot g_0 \cdot \delta} \right)^{\frac{1}{d}}. \quad (\text{A-3})$$

For clarity, we recall here the transfer rate of eqn. 2-1 with $x_{ij} = 2 R_{hop}$ and $\delta = E_a = E_j - E_i$:

$$\Gamma \sim \exp \left\{ -\frac{2 R_{hop}}{\xi} - \frac{\delta}{k_B T} \right\}. \quad (\text{A-4})$$

We insert the estimation of R_{hop} in A-4 and the term in the exponential becomes

$$-\left[\frac{2}{\xi} \left(\frac{1}{c_d \cdot g_0 \cdot \delta} \right)^{\frac{1}{d}} + \frac{\delta}{k_B T} \right]. \quad (\text{A-5})$$

The optimum hopping energy range δ_0 is obtained by minimising eqn. A-5

$$\frac{d}{d\delta} [\dots]_{\delta=\delta_0} = 0 \Rightarrow \frac{2}{\xi} \left(\frac{1}{c_d \cdot g_0} \right)^{\frac{1}{d}} \left(-\frac{1}{d} \right) \delta_0^{-\frac{d}{d+1}} + \frac{1}{k_B T} = 0 . \quad (\text{A-6})$$

Then,

$$\delta_0 = \left(\frac{\xi \cdot d}{2k_B T} (c_d \cdot g_0)^{\frac{1}{d}} \right)^{-\frac{d}{d+1}} . \quad (\text{A-7})$$

By substituting δ_0 back in the exponential term of eqn. A-5 and by exploiting a bit of algebra we obtain the Mott VRH formula with $T_{0,M}$ (eqn. 2-4) and

$$c(d) = \frac{2^{d \cdot d}}{c_d} \cdot \left(1 + \frac{1}{d} \right)^{d+1} = \begin{cases} 8.0 , & d = 1 \\ 8.6 , & d = 2 \\ 18.1 , & d = 3 \end{cases} , \quad (\text{A-8})$$

An identical procedure is carried out by considering coulombic interactions among charge carriers. The energy scale for the charge hopping from E_i to E_j becomes

$$\delta_c = E_j - E_i - \frac{q^2}{4\pi \cdot \epsilon_0 \epsilon \cdot R_{hop}} = E_j - E_i - e_{ij} . \quad (\text{A-9})$$

Because a hopping event implies that δ_c is positive, an energy gap greater than e_{ij} must exist. This is the case of ES VRH model: $g(E)$ vanishes around E_F , while for energies $> \delta_c$, $g(E)$ has a linear decrease ($s=1$) in 2D systems and a parabolic decrease ($s=2$) in 3D systems.

Unfortunately, the procedure does not lead to the numerical coefficient ($=2.8$) used in 2-5. Further assumptions must be made and the passages are briefly discussed in Section 14.5 of reference [157].

Fluctuation-induced tunnelling (FIT)

For completeness, we present here the fluctuation-induced tunnelling (FIT) transport model that was developed for disordered systems, such as granular metals [166]. In FIT framework, transport is dominated by charge transfer between large conducting segments rather than hopping between localised states. Thermal vibrations allow then the transfer between these highly doped regions. ‘‘Tunnelling’’ is used improperly to indicate a classic charge transfer, instead of its quantum mechanical counterpart. An

extension of FIT to other mechanisms was proposed by authors of reference [167]. They showed how transport between two strongly doped polaronic clusters separated by less doped domains could occur according to fluctuations of dopant ions positions.

Resistivity in FIT scheme is given by

$$\rho_{FIT}(T) = \rho_{0,FIT} \cdot \exp\left\{\frac{T_{0,FIT}}{T + T_{1,FIT}}\right\}, \quad (\text{A-10})$$

where $T_{0,FIT}$ and $T_{1,FIT}$ are constant parameters which depends on the insulating regions characteristics, thought as energy barriers between conducting regions. Higher the barrier is and so, larger $T_{0,FIT}$ is, larger the contribution of charge transfers is in transport. Making the comparison with NNH model of eqn. 2-2, the denominator can be considered as an effective temperature ($T_{eff} = T + T_{1,FIT}$).

The reduced activation energy for FIT models is a little cumbersome and it results

$$W_{FIT} = \frac{T_{0,FIT} \cdot T}{(T_{1,FIT} + T)^2} = \frac{T_{0,FIT} \cdot T}{T_{eff}^2} \quad (\text{A-11})$$

and, in turns, the logarithm becomes

$$\ln W_{FIT} = \ln T_0 + \ln T - 2 \cdot \ln T_{eff} \quad (\text{A-12})$$

The limit $T \gg T_{1,FIT}$ gives the condition for which thermal activation over the barrier is dominant. Under such limit, we can approximate $\ln T_{eff} \approx \ln T + \frac{T_{1,FIT}}{T}$ by a series expansion at first order. Eq. A-12 is then approximated to

$$\ln W_{FIT} \approx \ln T_0 - \ln T - \frac{2 \cdot T_{1,FIT}}{\exp(\ln T)} \quad (\text{A-13})$$

The curve in eqn. A-13 is a concave function ($T_{1,FIT} > 0$) and it describes a line for $T_{1,FIT} = 0$. In this latter case, the model has the same activated form of NNH transport with $T_{0,FIT} = -E_a/k_B$. Because this curved functional dependence has not been observed in the $W(T)$ in our GRM films, we ruled out the FIT as plausible transport model.

A.2 Review of Literature about CT Studies in RGO Systems

Table A-1. Comparison of the literature about charge transport at low temperature T in RGO devices: both single sheet and thin films (separated in two pages for readability). The references are ordered following the publication year. More than one transport model is reported when the authors suggested multiple transport mechanisms were acting simultaneously at low T .

VRH: Variable-Range Hopping (ES: Efros-Shoklovskii type; 2D or 3D: Mott types); FIT: Fluctuation-Induced Tunnelling.

Ref.	Year	Reduction method	Deposition method	Transport model at low T	$W(T)$ analysis
single sheet					
Gomez-Navarro <i>et al.</i> [91]	2007	chemical (hydrazine)	drop-casting	2D-VRH	no
Kaiser <i>et al.</i> [56]	2009	chemical (H plasma)	drop-casting	2D-VRH	no
Lopez <i>et al.</i> [168]	2009	thermal + CVD defects healing	drop-casting	2D-VRH	no
Eda <i>et al.</i> [54]	2009	chemical (hydrazine)	drop-casting	2D-VRH	no
Joung <i>et al.</i> [55]	2012	chemical (hydrazine)	dielectro-phoresis	ES-VRH	yes
Baek <i>et al.</i> [169]	2014	thermal (in Ar)	drop-casting	3D-VRH + thermal activation	no
Park <i>et al.</i> [57]	2017	thermal (in Ar)	bubble method	ES-VRH	no

Ref.	Year	Reduction method	Deposition method	Transport model at low T	$W(T)$ analysis
thin film					
Wang <i>et al.</i> [62]	2011	chemical (hydrazine) + thermal	coating	thermal activation	yes (bad fit)
Muchharla <i>et al.</i> [61]	2014	chemical (vitamin C)	drop-spin casting	2D-VRH	yes
Rai <i>et al.</i> [60]	2015	thermal (in Ar)	drop-casting	2D-VRH	no
Kumar <i>et al.</i> [59]	2015	chemical (hydrazine)	mechanical pressing	3D-Mott	yes (no fit)
Kim <i>et al.</i> [63]	2015	chemical + thermal	drop-casting	3D-VRH + FIT + thermal activation	no
Vianelli <i>et al.</i> [65]	2016	thermal (in high-vacuum)	spin-coating	2D-VRH	no
Negishi <i>et al.</i> [64]	2016	thermal (in ethanol)	dip-coating	band transport	no
Faucett <i>et al.</i> [58]	2017	voltage-induced electroreduction	spin-coating	ES-VRH	yes
Shaina <i>et al.</i> [97]	2017	thermal (in Ar)	spin-coating	VRH	yes (no fit)
Haque <i>et al.</i> [94]	2018	thermal	pulsed-laser deposition	2D-VRH or ES-VRH	no
Silverstein <i>et al.</i> [95]	2019	voltage-induced electroreduction	drop-casting	ES-VRH	yes
Silipigni <i>et al.</i> [170]	2019	thermal (in vacuum)	vacuum-assisted filtration	thermal activation	no
Zeng <i>et al.</i> [171]	2019	thermal + joule heating	3D printing	3D-VRH + thermal activation + quantum tunnelling	no
Kurnosov <i>et al.</i> [96]	2020	thermal	vacuum-assisted filtration	ES-VRH	yes

A.3 Additional Data about GRM

We report here all the experimental data that have not found a proper space in the main discussion but are relevant to fully appreciate the work.

XPS data for GRMs

In Fig. A-1, the survey XPS spectra of GO, RGO (900°) and EGO are shown. XPS measurements were performed on filtered films, but they are representative of the material by itself. Elemental composition calculated from the analysis of all different spectra and oxygen functionalities calculated from the analysis of C 1S spectra are presented respectively in Table A-2 and Table A-3.

Table A-2. Elemental chemical composition of studied materials. Sulphur in EGO is due to residual solvent (DMF).

	C [%]	O [%]	N [%]	S (-O) [%]
GO	73.0 ± 0.9	26.4 ± 0.9	0.4 ± 0.1	\
RGO	96.5 ± 0.9	3.3 ± 0.4	0.2 ± 0.2	\
EGO	84.9 ± 0.9	13.8 ± 0.9	1.1 ± 0.4	0.2 ± 0.1

Table A-3. Chemical functionalities of studied materials, as they were determined by high-resolution XPS analysis of C1s spectra.

	C Sp² [%]	C Sp³ [%]	C-OH [%]	C-O-C [%]	C=O [%]	O-C=O [%]	O/C
GO	32.9 ± 0.9	11.9 ± 0.8	3.3 ± 0.3	42.5 ± 0.5	6.3 ± 0.4	3.1 ± 0.4	0.37 ± 0.02
RGO	93 ± 2	3.9 ± 1.6	2.0 ± 0.7	< 0.5	< 0.5	< 0.5	0.03 ± 0.01
EGO	71 ± 2	11 ± 2	1.2 ± 0.5	12 ± 2	2.2 ± 0.7	3.0 ± 0.6	0.15 ± 0.01

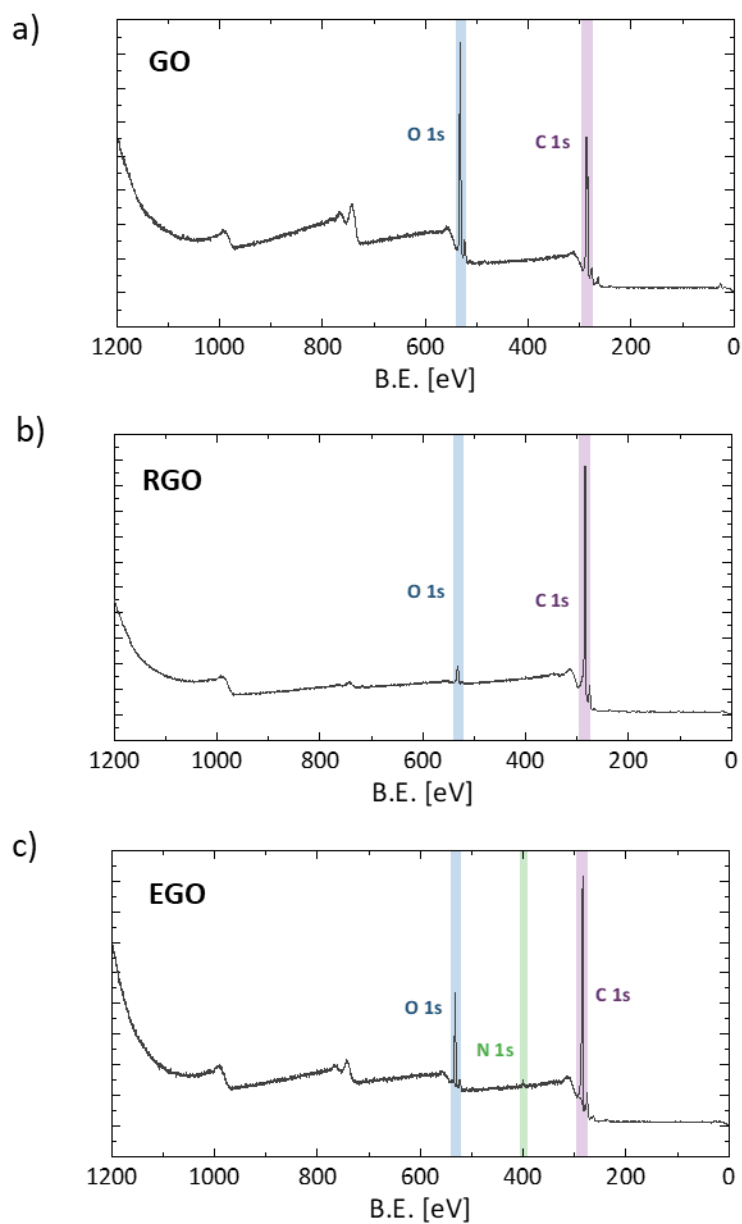


Figure A-1. Survey XPS spectra for (a) GO, (b) RGO and (c) EGO. B.E. in x-axis refers to binding energy E_B . Measurements were performed with a Mg anode in the x-rays source. No metallic impurities are observed in any spectra.

The XPS spectrum of C 1s signal for GO is shown in Figure A-2. The double peak highlights the presence of carbon-carbon bonds and carbon-oxygen functionalities, that are present in the material structure.

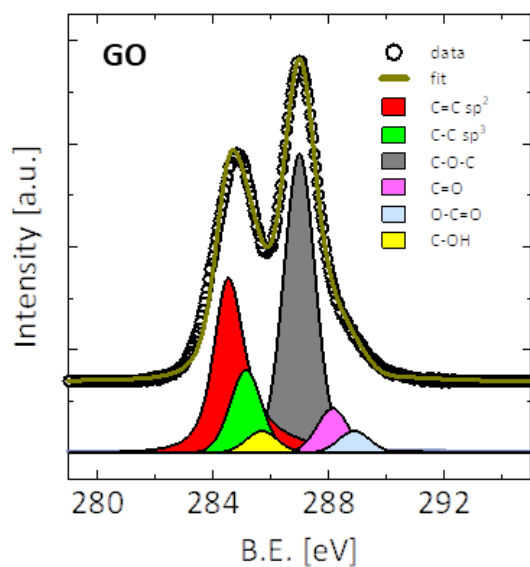


Figure A-2. High-resolved XPS spectra of C 1s for GO used in this work. B.E. in x-axis refers to binding energy E_B . The coloured peaks below the data represents the components used in the analysis. A rich variety of oxygen functional groups decorates the 2D GO sheet.

Additional AFM images of GRM films

We include representative AFM images of different RGO films and of a filtered EGO film in Figure A-3. The surface roughness and surface morphology of the films differ depending on the deposition technique and, in minor part, on the film building block.

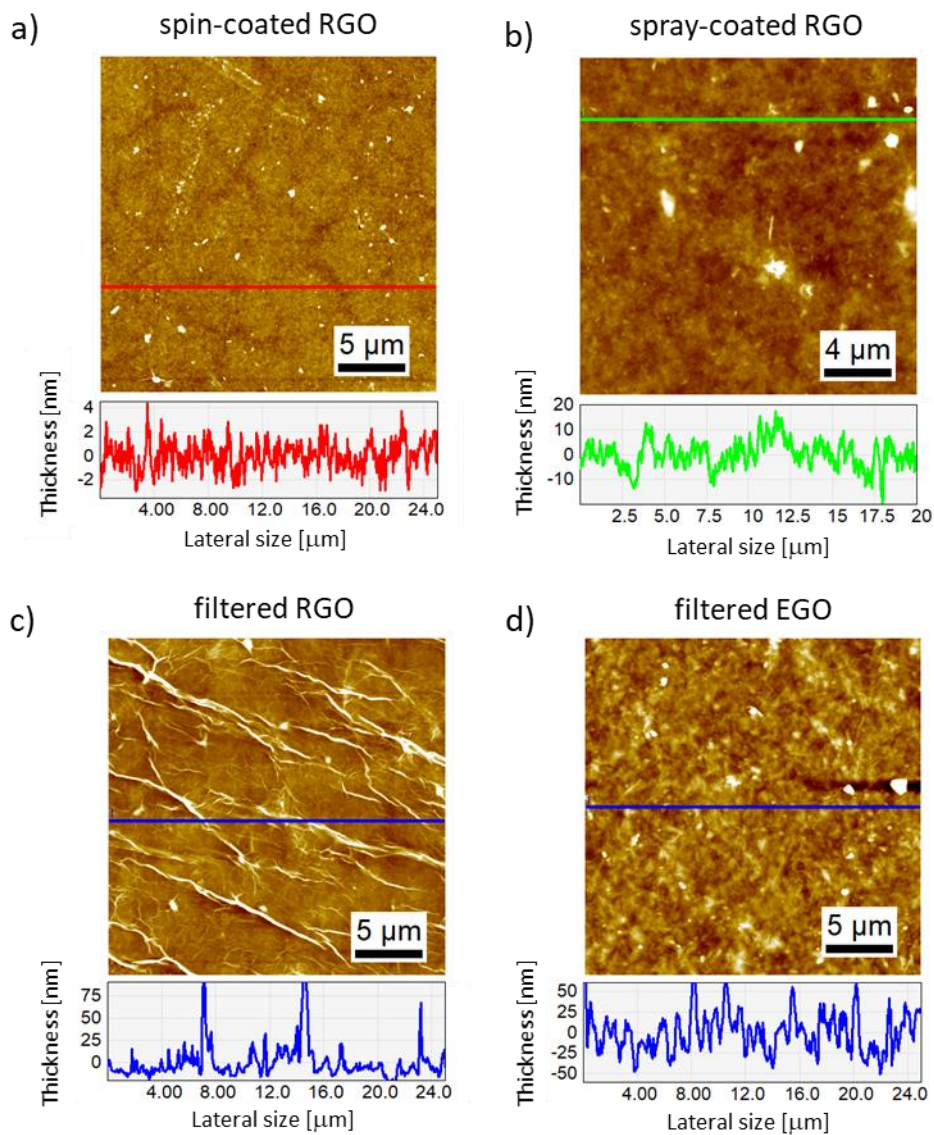


Figure A-3. AFM of the surfaces of (a,b,c) different RGO thin films and (d) a EGO thin film. The height profile along the coloured line is shown at the bottom of each image. It gives an idea of the surface roughness for each kind of network.

XRD measurement of GO

The XRD measurement in Fig. A-4 was performed on GO in powder form. The spectrum shows two peaks corresponding to out-of-plane [001] crystal direction and [100] crystal direction of oxidized graphite [172] and intercalated graphite [173]. z-periodicity and z-coherence length are respectively (8.0 ± 0.7) Å and (8.0 ± 0.1) nm, as computed from the analysis of [001] peak. From [100], the aromatic, graphene-like domains result around 8 nm wide. These values demonstrate the partial crystalline nature of GO and the difference compared to un-oxidised graphite.

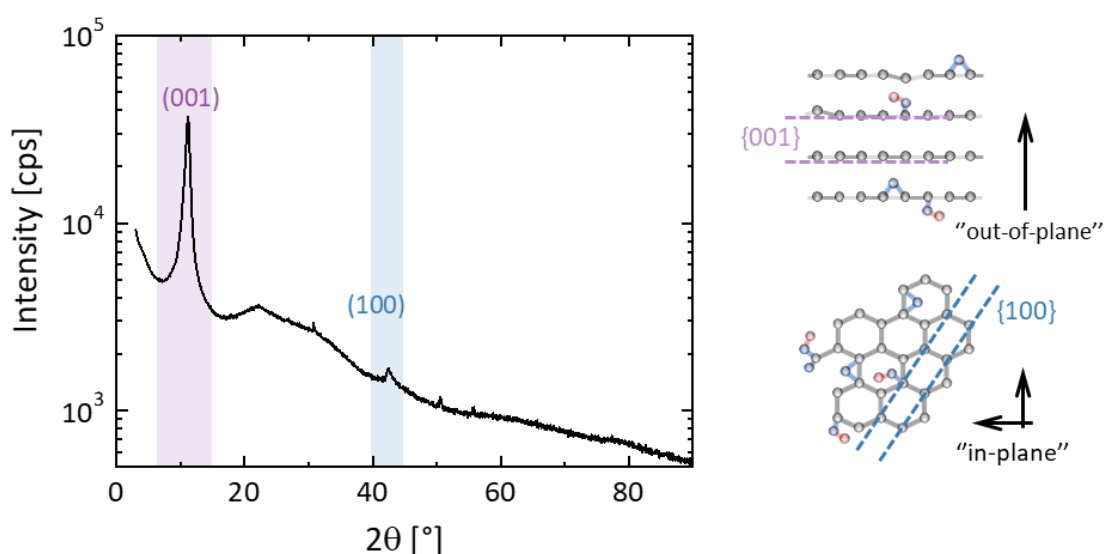


Figure A-4. Specular scan XRD ($\lambda = 1.54184$ Å) spectrum of GO. Both out-of-plane and in-plane characteristic x-ray reflections are observed. The two “ball and sticks” molecular models on the right depict the planes of symmetry of GO for the obtained peaks.

A.4 References

- [54] Eda, G., *et al.*, *Insulator to Semimetal Transition in Graphene Oxide*. The Journal of Physical Chemistry C **113**, 35, p. 15768-15771 (2009). www.doi.org/10.1021/jp9051402
- [55] Joung, D., *et al.*, *Efros-Shklovskii variable-range hopping in reduced graphene oxide sheets of varying carbon ρ^2 fraction*. Physical Review B **86**, 23, p. 235423 (2012). www.doi.org/10.1103/PhysRevB.86.235423
- [56] Kaiser, A.B., *et al.*, *Electrical Conduction Mechanism in Chemically Derived Graphene Monolayers*. Nano Letters **9**, 5, p. 1787-1792 (2009). www.doi.org/10.1021/nl803698b
- [57] Park, M., *et al.*, *Electrical and thermoelectric transport by variable range hopping in reduced graphene oxide*. Applied Physics Letters **111**, 17, p. 173103 (2017). www.doi.org/10.1063/1.4987021

- [58] Faucett, A.C., *et al.*, *Evolution, structure, and electrical performance of voltage-reduced graphene oxide*. *FlatChem* **1**, p. 42-51 (2017). www.doi.org/10.1016/j.flatc.2016.10.003
- [59] Kumar, R., *et al.* *Charge transport mechanism of hydrazine hydrate reduced graphene oxide*. *IET Circuits, Devices & Systems* **9**, 6, p. 392-396 (2015).
- [60] Rai, V., *et al.* *Correlating Chemical Structure and Charge Transport in Reduced Graphene Oxide for Transparent Conductor and Interconnect Applications*. in *2015 IEEE International Symposium on Nanoelectronic and Information Systems*. 2015.
- [61] Muchharla, B., *et al.*, *Temperature dependent electrical transport of disordered reduced graphene oxide*. *2D Materials* **1**, 1, p. 011008 (2014). www.doi.org/10.1088/2053-1583/1/1/011008
- [62] Wang, S.-W., *et al.*, *Transport behavior and negative magnetoresistance in chemically reduced graphene oxide nanofilms*. *Nanotechnology* **22**, 33, p. 335701 (2011). www.doi.org/10.1088/0957-4484/22/33/335701
- [63] Kim, H.-J., *et al.*, *Charge Transport in Thick Reduced Graphene Oxide Film*. *The Journal of Physical Chemistry C* **119**, 51, p. 28685-28690 (2015). www.doi.org/10.1021/acs.jpcc.5b10734
- [64] Negishi, R., *et al.*, *Band-like transport in highly crystalline graphene films from defective graphene oxides*. *Scientific Reports* **6**, 1, p. 28936 (2016). www.doi.org/10.1038/srep28936
- [65] Vianelli, A., *Charge transport in Reduced Graphene Oxide Thin Films*, PhD Thesis; Università di Modena e Reggio Emilia (2016). <https://morethesis.unimore.it/theses/available/etd-02162016-220621/>
- [91] Gómez-Navarro, C., *et al.*, *Electronic Transport Properties of Individual Chemically Reduced Graphene Oxide Sheets*. *Nano Letters* **7**, 11, p. 3499-3503 (2007). www.doi.org/10.1021/nl072090c
- [94] Haque, A., *et al.*, *Temperature Dependent Electrical Transport Properties of High Carrier Mobility Reduced Graphene Oxide Thin Film Devices*. *IEEE Transactions on Semiconductor Manufacturing* **31**, 4, p. 535-544 (2018). www.doi.org/10.1109/TSM.2018.2873202
- [95] Silverstein, K.W., *et al.*, *Voltage-reduced low-defect graphene oxide: a high conductivity, near-zero temperature coefficient of resistance material*. *Nanoscale* **11**, 7, p. 3112-3116 (2019). www.doi.org/10.1039/C8NR08285E
- [96] Kurnosov, N.V., *et al.*, *Comparison of temperature dependences of electrical conductivity of composite rGO-SWNT film with rGO and SWNT films*. *Low Temperature Physics* **46**, 3, p. 285-292 (2020). www.doi.org/10.1063/10.0000700
- [97] Shaina, P.R., *et al.*, *Anomalous charge transport in reduced graphene oxide films on a uniaxially strained elastic substrate*. *Journal of Physics: Condensed Matter* **29**, 23, p. 235301 (2017). www.doi.org/10.1088/1361-648x/aa6eba
- [157] Shklovskii, B.I., *et al.*, *Electronic properties of doped semiconductors*, Springer-Verlag (1984).
- [166] Sheng, P., *Fluctuation-induced tunneling conduction in disordered materials*. *Physical Review B* **21**, 6, p. 2180-2195 (1980). www.doi.org/10.1103/PhysRevB.21.2180
- [167] Zuppiroli, L., *et al.*, *Hopping in disordered conducting polymers*. *Physical Review B* **50**, 8, p. 5196-5203 (1994). www.doi.org/10.1103/PhysRevB.50.5196
- [168] López, V., *et al.*, *Chemical Vapor Deposition Repair of Graphene Oxide: A Route to Highly-Conductive Graphene Monolayers*. *Advanced Materials* **21**, 46, p. 4683-4686 (2009). www.doi.org/https://doi.org/10.1002/adma.200901582
- [169] Baek, S.J., *et al.*, *The effect of oxygen functional groups on the electrical transport behavior of a single piece multi-layered graphene oxide*. *Synthetic Metals* **191**, p. 1-5 (2014). www.doi.org/10.1016/j.synthmet.2014.02.008
- [170] Silipigni, L., *et al.*, *Band-like transport in high vacuum thermal reduced graphene oxide films*. *Vacuum* **165**, p. 254-261 (2019). www.doi.org/10.1016/j.vacuum.2019.04.025
- [171] Zeng, Y., *et al.*, *Thermally Conductive Reduced Graphene Oxide Thin Films for Extreme Temperature Sensors*. *Advanced Functional Materials* **29**, 27, p. 1901388 (2019). www.doi.org/10.1002/adfm.201901388
- [172] Muzyka, R., *et al.*, *Oxidation of graphite by different modified Hummers methods*. *New Carbon Materials* **32**, 1, p. 15-20 (2017). [www.doi.org/10.1016/S1872-5805\(17\)60102-1](http://www.doi.org/10.1016/S1872-5805(17)60102-1)
- [173] Leung, S.Y., *et al.*, *Structural studies of graphite intercalation compounds using ($\text{\$001\$\})$ x-ray diffraction*. *Physical Review B* **24**, 6, p. 3505-3518 (1981). www.doi.org/10.1103/PhysRevB.24.3505

List of Figures

Figure 1-1. (a) Chemical structure of graphene: carbon atoms are arranged in a honeycomb lattice. The scheme on the right depicts the three σ orbitals (i.e. sp^2) and the π orbital (i.e. p_z), that is perpendicular to the sheet. σ orbitals form in-plane σ bonds that strongly connect the carbon atoms and are responsible for the structural properties of the graphene sheet.
 (b) The bonding and antibonding electronic bands for σ orbitals and for π orbitals. Because σ bands are separated by a quite large gap, only π bands are usually considered for electronic properties of graphene. Images were inspired from ref. [7]. 4

Figure 1-2. Classification of graphene-related materials (GRMs) according to their chemical state (i.e oxygen to carbon ratio), their average lateral size and their average number of layers. The image is from ref. [11].5

Figure 1-3. List of some graphene and GRM production methods classified by the two basic approaches in nanofabrication: “top-down” or “bottom-up”. 6

Figure 1-4. (a) Scheme of Lerf and Klinowski structural model for GO. Image from [16]. (b) Digital coloured, transmission electron microscopy (TEM) images of GO and RGO. C Sp^2 regions are depicted in yellow, while functionalised regions in red. Blue areas represent holes in the materials. The increase of C Sp^2 is evident in RGO compared to GO. Images from [17]. 7

Figure 1-5. (a) High resolution TEM image of a EGO sheet. The sheet edge cross section is highlighted, showing a bilayer structure of the sheet. (b) On the left, a AFM image of a EGO sheet over a SiO_2 substrate; on the right, corresponding AFM histogram analysis with heights (see inset) measured at different regions, as marked in the image. The height peak for each layer is fitted with a main sharp component (L_1) plus a broader component (L_2) due to debris. The scheme at the bottom represents the suggested EGO morphology. Figures adapted from [33]. 9

Figure 1-6. Different examples of the use of GRM in realistic devices. Together with a digital photograph or a scheme, a cross-section SEM micrograph is shown of: (a) “Graphene” paper (adapted from [47]); (b) a printed transistor (adapted from [2]); and (c) a cellulose/GRM composite (adapted from [48]). 11

Figure 2-1. Diagrams of energy E versus spatial coordinate r for different transport mechanisms. From left to right, by increasing localisation: (a) band-like transport, (b) critical regime transport or nuclear tunnelling transport, and (c) hopping transport. The dashed line at EC corresponds to energy edge at which transport occurs, e.g. the bottom of the conduction band. The light blue areas represent de-localised regions, while blue short lines are localised energy levels. Black dots are the charge carriers. The diagrams are shown for negative charge carriers. A similar picture (with reversed energy band) could be drawn for positive carriers, i.e. holes. 18

Figure 2-2. Schematic illustration of two hopping transport models: (a) the Nearest Neighbour Hopping (NNH) transport, or Arrhenius-like transport, and (b) the variable range hopping (VRH) transport. The energy E is along the y-axis. Energy levels are depicted as short light blue dashes. If they are occupied by a carrier, a dark dot is present; otherwise, the states are unoccupied. In the VRH, charges around the Fermi energy EF can move to further unoccupied levels in the spatial landscape, without the need to overcome the thermal energy kBT 19

Figure 2-3. Scheme representing different materials ordered by their electrical resistivity. Simplified ρT and $W(T)$ plots are also presented for different charge transport regimes. While ρT does not always allow an unambiguous distinction of CT regimes, the fit of $\ln W - \ln T$ does. A system with localised charges has a negative $\ln W - \ln T$ slope, while metallic transport is identified by a positive $\ln W - \ln T$ slope. In a critical regime, W is independent on T 24

Figure 2-4. Log-log scale plot of resistivity ρT (top) and of corresponding reduced activation energy $W(T)$ (bottom) for (a) a single RGO sheet and (b) a representative RGO network. Conversely to ρ analysis, the use

of $W(T)$ allows to unambiguously discriminate different transport regimes. Two transport regimes are obtained in RGO: VRH (red line) and PL (black line). 29

Figure 2-5. Plot of relevant transport parameters as a function of room temperature resistivity ρ_{RT} for all devices studied in ref. [66]. (a) Plot of transition temperature T^* vs ρ_{RT} , with a red dashed line as eye guide. (b) Plot of exponent p values in the VRH regime vs ρ_{RT} . All the obtained values are consistent with $p=1/2$, corresponding to the ES type of the VRH. (c) Plot of power exponent m values in PL regime vs ρ_{RT} . The corresponding reorganization energy λ is also reported on the secondary y-axis. 30

Figure 2-6. (a) Correlation plot of PL regime: $\ln B$ vs m , obtained from eqn. 2-13, for all 28 RGO devices. The good linear fit (red curve) suggests a single transport mechanism common of all RGO networks. (b) Correlation plot between the PL and VRH regimes obtained by requesting the continuity of $W(T)$ at T^* . In all graphs, symbols correspond to different type of devices: (■) thin films, (○) few sheets partially overlapped and (△) single high-reduced RGO sheet. 32

Figure 2-7. Dependence of localization length ξ on: (a) room temperature resistivity ρ_{RT} ; (b) C sp^2 content in the RGO sheets; (c) average sheets size S_{RGO} of RGO used to fabricate the films; and (d) film thickness, quantified by the number of stacked layers N_{layer} . In (a) and (b), symbols correspond to different type of devices: (■) thin films, (○) few sheets partially overlapped and (□) single high-reduced RGO sheet. 34

Figure 2-8. Schemes depicting the charge transport in single RGO sheet and in RGO networks. (a) Comparison between the two cases: purely 2D CT in single RGO sheet (left) and 3D transport in stacked RGO sheets (right). In this latter case, the out-of-plane motion due to π - π stacking allows charges to overcome defects.

(b,c) Description of CT in RGO networks as they were composite materials with conductive fillers. Cartoons for this geometrical model from (b) top view and (c) lateral view. In (b), the aromatic sp^2 domains are represented by coloured disks. Conduction occurs via overlapped disks belonging to different planes. The same scheme is shown in (c) from lateral view, with disks that becomes short black lines. The red curved lines represent, instead, all the possible geometrical paths of average size ξ a charge can follow. By reducing the film thickness, also the number of paths is decreased. 37

Figure 3-1. Scheme of GO synthesis following a modified Hummer's method. 42

Figure 3-2. Scheme of EGO synthesis protocol. Image was taken from ref. [36]. 43

Figure 3-3. Scheme of a spin-coating deposition. Each phase of the method is illustrated separately. The deposited GRM suspension is depicted in dark grey on the top of a substrate (e.g. SiO_2), in lavender. 45

Figure 3-4. (a) Photograph of the vacuum-assisted filtration equipment. The inset shows a GO film on a nylon filter membrane. (b) Scheme of the GRM film fabrication by vacuum-assisted filtration. 48

Figure 3-5. Scheme of GRM film fabrication by the spray-coating process. 50

Figure 3-6. Scheme of the tube furnace used in this work for GRM thermal treatment at high vacuum. 52

Figure 3-7. (a) Optical image of a RGO film (in dark grey) with evaporated Ti/Au electrodes (in yellow). Samples with this 2 parallel line electrode configuration were used to estimate the contact resistance RC at the RGO/electrode interface. (b) Scheme of the film/contact geometry with RC and the transfer length dt highlighted. (c) Plot of 2-probe resistance R as a function of the electrodes distance D for three different devices (blue squares), following the transfer length method. The linear fit (red curves) permits to estimate RC , as well as the film resistance R_{film} and dt 53

Figure 4-1. (a) Basic principle of photoelectron spectroscopy: incident light of energy $h\nu$ impinges the sample surface and it causes the emission of an electron e^- , that is detected and its kinetic energy analysed. (b) Energy diagram representing the same electron photoemission process of (a). The sample comprises atoms with deep energy core levels and a continuum band of valence energy levels. 57

Figure 4-2. Approximated three-step model for the electron photoemission. Energy of electronic states is along the vertical axis, while the spatial coordinates are along the horizontal axis. $z=0$ indicates the interface between the sample ($z<0$) and the vacuum ($z>0$). In the first step of the process, (1) the electron is optically

excited from initial state $E(i)$ to $E(ii)$. Then, (2) it travels to the surface, and finally (3) is transmitted through the surface and emitted into the vacuum.....	58
Figure 4-3. (a) A scheme of a typical AFM set-up. The imaging mechanism relies on the interaction occurring between a sharp tip and the sample structure. On the right corner, an electronic micrograph (SEM) of the tip used for topographic imaging. (b) A sketch of “tapping” imaging mode: the change in sample-tip interaction due to a topography variation is met by a change in the applied potential to the cantilever to keep the amplitude constant.	65
Figure 4-4. Summary of the flattening procedure for AFM images. Three AFM images with corresponding height histogram below are presented by increasing data processing, from left to right. The left image is the raw data, while the right image represents the real, flat substrate after polynomials subtraction. Image adapted from ref. [133].	69
Figure 4-5. Scheme of XRD measurement configuration for (a) specular scan and for (b) rocking curve. In the bottom, the obtainable parameters from each kind of measurement are defined.	73
Figure 4-6. (a) Photograph of the Hall station probe assembly. A sample is placed below the 4 tip probes. Sample-probes electrical contact is achieved by lowering the reddish metal clip. (b) The electrical measurements performed in 4-probe Van der Pauw scheme.....	76
Figure 4-7. (a) Digital photograph of the PPMS dark grey Dewar flask. (b) Simplified scheme of the PPMS flask with the layered structure coloured for clarity.	77
Figure 4-8. Photograph of the sample holder, named puck, used for electrical measurements with the PPMS. It is a version particularly designed for resistivity measurements (“resistivity option” of Quantum Design PPMS). The 12 gold-plated pads, divided in groups of 4, are visible on the green insulating cover. A GRM self-standing membrane (grey square) on SiO ₂ (violet region) is wire bonded to some of the pads.	78
Figure 4-9. Scheme of the $\rho(T)$ characterization using the Physical Property Measurement System (PPMS) and a “home-coded” acquisition software.	79
Figure 5-1. AFM image of isolated RGO sheets deposited on SiO ₂ by spin-coating. The z-colour scale indicates the height of measured objects in a false colour system: RGO sheets are shown in yellow, while the substrate is in a dark red nuance. RGO owns a uniform thickness of (0.6 ± 0.1) nm including the substrate contribution, as shown in the height distribution on the right (from dashed, blue line area in the image).	84
Figure 5-2. (a) Thickness distribution and (b) Size distribution of RGO sheets, as determined from AFM images. A total of 774 objects were analysed. The red line in both graphs indicates the mean value. We recall that Size is equal to the square root of RGO sheet area.	84
Figure 5-3. High-resolved XPS spectra of C 1s for filtered RGO. B.E. in x-axis refers to binding energy EB . The colored peaks below the data represents the components used in the analysis. RGO is composed mainly by sp ² hybridised carbon (>90%) with a small amount of C sp ³ and residual oxygen functional groups.....	85
Figure 5-4. (a) Optical image of large RGO sheets. The sheets are superimposed and were reduced at 900°C in high vacuum after deposition. Coloured numbers indicate the micrometric regions where Raman spectroscopy was performed. (b) Raman spectra of RGO in (a). We thank V. Mussi of CNR-IMM (Italy) for performing the measurements.....	86
Figure 5-6. XRD spectra for the three type of RGO films. Intensity- 2θ spectra (a) and Intensity- $\Delta\omega$ spectra (b) obtained by specular scan measurements and by rocking curves measurements, respectively. x-axis of (b) is reported with respect to $2\theta_{002}$ positions.....	88
Figure 5-7. (a) AFM image of representative EGO sheets deposited on SiO ₂ by spin-coating. The height is represented by a set of false colours, from dark brown (i.e. the substrate) to deep yellow. The sheets have different thicknesses and are composed by multiple (bi-)layers. Holes and wrinkles, visible on the top surface of two sheets, are caused both by the fastness of the electrochemical oxidation-exfoliation process and by the amount of released energy. (b) A scheme of a representative EGO flake.	90

Figure 5-8. (a) Thickness versus Size plot of studied EGO flakes. It is immediately evident that EGO is not simply mono-atomic in thickness, but it comprises thicker structure. The corresponding (b) thickness and (c) size distributions are also reported. The red line in (b) and (c) indicates the mean value. 91

Figure 5-9. High-resolved XPS spectra of C 1s for EGO. B.E. in x-axis refers to binding energy EB . The colored peaks below the data represent the components used in the analysis..... 92

Figure 5-10. Multi-scale morphological images of EGO thin films fabricated with filtration deposition technique. Images obtained by (OM) Optical, (SEM) Scanning Electron and (AFM) Atomic Force Microscopies. AFM images show the film borders obtained by scratch. Profile heights correspond to the traced horizontal lines. AFM z-ranges: 200 nm. 93

Figure 5-11. XRD measurements on EGO thin films: (a) specular scan and (b) rocking curve. 93

Figure 5-12. Structural analysis of RGO an EGO thin films. (a) Scheme of the building blocks and (b) their arrangement plotted as z-coherence length L vs mosaicity M (averaged value over independent samples). A sketch of the proposed structural model for each sample is depicted next to each square marker. 94

Figure 6-1. Experimental $\ln W(\ln T)$ curves of two RGO thin films. In (a), a large variation of reduced activation energy ΔW occurs at low T and the transition between another regime is clearly defined. In (b), the variation ΔW at low T is instead small. Hence, it exists a corresponding region ΔT^* where the transition is poorly defined. A sketch of the two situations is depicted below: (c) ρ_0 is constant because $n \approx 0$ at low T ; and (d) $\rho_0 = \rho_0 T$ because $n \sim W_0$ 98

Figure 6-2. $\ln W(\ln T)$ curves for two RGO thin films with fits according to the analysis protocol explained in the text. (a) RGO sample having a large variation of ΔW at low temperatures and $\rho_0 = \text{const}$; (b) RGO sample in the opposite case with $\rho_0 = \rho_0 T$. In the latter, the developed protocol is needed and the VRH fit with $n=0$ (violet dotted line) cannot follow the measured data..... 101

Figure 6-3. m , T_0 and T^* parameters computed considering $n \neq 0$ (from eqn. 6.9 and eqn. 6.10) for devices of ref. [66] and ref. [95]. The parameters are plotted as a function of (a,b,c) ρRT and of (d,e,f) the same quantities computed with $n=0$ 103

Figure 6-4. Generalised correlation plot between VRH and PL regimes of Kovtun et al data [66] (square) and Silverstain et al data [95] (triangle). The red line shows the linear fit, having slope $-p_{\text{mean}} = -0.54 \pm 0.02$ 104

Figure 6-5. n values vs. ξ , as obtained for the data of ref. [66] (square) and ref. [95] (triangle). The red line shows the weighted mean value of 0.07 ± 0.02 . All RGO devices have a value of n compatible with the mean value, within the uncertainty limits. 105

Figure 7-1. Operational scheme of present CT investigation in GRM thin films: (a) varying the network order and (b) varying the network building block. 106

Figure 7-2. Room temperature resistivity ρRT vs. (a) z-coherence length L and (b) mosaicity M for the three types of RGO film: spin-coated (red square), filtered (blue triangle) and spray-coated (green pentagon). The faded brown arrow in both plots helps to visualize the direction of increasing structural disorder. Inserted ρRT values are the averaged values of all measured samples (for the same structure). 107

Figure 7-3. $\rho(T)$ curves of (a) a spin-coated RGO film, (b) a filtered RGO film and (c) a spray-coated RGO film. For clarity, the curves are normalised by the resistivity value $\rho RT \equiv \rho T = 297K$ 108

Figure 7-4. Room temperature resistivity ρRT vs. ρr ($= \rho(10K)/\rho(297K)$) ratio of RGO thin films. 109

Figure 7-5. $W(T)$ in log-log space computed from the curves of Figure 6-1: (a) spin-coated RGO film, (b) filtered RGO film and (c) spray-coated RGO film. The T regions showing different CT regimes are highlighted with different colours. VRH (red) and PL (light blue) fitting lines are also reported. 110

Figure 7-6. Localization length ξ vs. room temperature resistivity ρRT of the different RGO thin films. Black squares correspond to data of ref. [66]. For samples measured in this work, the reported ξ and ρRT are the averaged values. 111

Figure 7-7. Generalised correlation plot between VRH and PL regimes (see eqn. 6-11). Current RGO film data are inserted together with Kovtun et al data [66] (square) and Silverstain et al data [95] (open triangle). The red line shows the linear fit, having slope $-p = -0.52 \pm 0.02$ 112

Figure 7-8. Localization length ξ as a function of the geometrical parameters – (a) z-size domain L and (b) mosaicity M - for the three RGO thin films: spin-coated (red square), filtered (blue triangle) and spray-coated (green pentagon). We plotted the average values for each deposition technique. The arrow points towards increasing structural disorder.
(c) Scheme of CT in the network structure. For all kind of studied RGO films, ξ spans over different building blocks: charge carriers are delocalized along a wire of length ξ , that it is depicted with a wine line. 113

Figure 7-9. Pre-factor exponent n vs. localisation length ξ for the measured RGO thin films: spin-coated (red square), filtered (blue triangle) and spray-coated (green pentagon). The shaded purple region represents the constant value ($=0.07 \pm 0.01$) obtained for RGO devices of ref. [66] in Chapter 6. 114

Figure 7-10. $\rho(T)$ curves of filtered GRM thin films made with different building blocks: (a) RGO and (b) EGO. For clarity, the curves are normalised by the resistivity value $\rho_{RT} \equiv \rho T = 297K$ 117

Figure 7-11. $W(T)$ in log-log space: (a) filtered RGO film and (b) EGO film. Data are computed from the $\rho(T)$ curves of Figure 7-10..... 118

Figure 7-12. Spectral power density SV versus frequency f for (a) EGO film and (b) RGO film. The different coloured lines represent spectra acquired at different temperature and inject current values. All the $SV(f)$ signals show a common shape: a $1/f$ dependence at low frequencies and a f independence (S_{white}) at high frequencies..... 120

Figure 7-13. Experimental values and fits of noise components. (a) and (b) depict the flicker noise amplitude K and the white noise term S_{white} vs. the injected current I . The different marks represent signals acquired at different temperatures, from 16K to 290K. $K(I)$ is fitted with a second order polynomial (red line).
In (c) and (d), the quadratic coefficient a_2 and the linear coefficient a_1 of $K(I)$ are plotted as a function of temperature.
The plots in (a) and (c) are for the EGO film, the ones in (b) and (d) for the RGO film..... 121

Figure A-1. Survey XPS spectra for (a) GO, (b) RGO and (c) EGO. B.E. in x-axis refers to binding energy EB . Measurements were performed with a Mg anode in the x-rays source. No metallic impurities are observed in any spectra. 132

Figure A-2. High-resolved XPS spectra of C 1s for GO used in this work. B.E. in x-axis refers to binding energy EB . The coloured peaks below the data represents the components used in the analysis. A rich variety of oxygen functional groups decorates the 2D GO sheet. 133

Figure A-3. AFM of the surfaces of (a,b,c) different RGO thin films and (d) a EGO thin film. The height profile along the coloured line is shown at the bottom of each image. It gives an idea of the surface roughness for each kind of network. 134

Figure A-4. Specular scan XRD ($\lambda = 1.54184 \text{ \AA}$) spectrum of GO. Both out-of-plane and in-plane characteristic x-ray reflections are observed. The two “ball and sticks” molecular models on the right depict the planes of symmetry of GO for the obtained peaks. 135

List of Acronyms

1D	one-dimensional
2D	bi-dimensional
3D	tri-dimensional
AFM	Atomic Force Microscopy
AR	Aspect Ratio
CT	Charge (Carrier) Transport
CVD	Chemical Vapour Deposition
DMF	N,N-Dimethylformamide
DSM	Dynamic Structural Model (of graphene oxide)
ES-VRH	Efros-Shklovskii Variable-Range Hopping
EGO	Electrochemical-exfoliated Graphene Oxide
FIT	Fluctuation-Induced Tunnelling
FWHM	Full Width Half Maximum
GO	Graphene Oxide
GRM	Graphene-Related Material
IPA	2-propanol
MIT	Metal-to-Insulator Transition
NMP	N-methyl-2-pyrrolidone
NT	(assisted) Nuclear Tunnelling
OM	Optical Microscopy
PL	Power Law

RGO	Reduced Graphene Oxide
<i>rhs / lhs</i>	right side / left side of equation
RSF	Relative Sensitivity Factor
SEM	Scanning Electron Microscopy
VRH	Variable-Range Hopping
TEM	Transmission Electron Microscopy
XPS	X-ray Photoemission Spectroscopy
XRD	X-Ray Diffraction

List of Activities during the PhD

Published Work

1. *“Benchmarking of graphene-based materials: real commercial products versus ideal graphene”*; A. Kovtun, E. Treossi, N. Mirotta, A. Scidà, A. Liscio, M. Christian, F. Valorosi, A. Boschi, R. J. Young, C. Galiotis, I. A. Kinloch, V. Morandi, and V. Palermo; *2D Mater.* **6**, 025006 (2019), www.doi.org/10.1088/2053-1583/aafc6e

I performed XPS measurements and data analysis of different commercial GRM powders, determining their elemental composition and their amount of aromaticity (% of C sp²).

2. *“Ultrafast charge carrier dynamics in Vanadium-modified TiO₂ thin films and its relation to their photoelectrocatalytic efficiency for water splitting”*; A. Piccioni, D. Catone, A. Paladini, P. O’Keeffe, A. Boschi, A. Kovtun, M. Katsikini, F. Boscherini, and L. Pasquini; *J. Phys. Chem. C* **124**, 49, 26572 (2020), www.doi.org/10.1021/acs.jpcc.0c06790

I contributed with the XPS characterisation of V-modified TiO₂ thin films. I estimated the chemical state of V in TiO₂ surface and I showed an increase of V content upon thermal annealing of the TiO₂ film. Such observation well correlates with the enhanced photoelectrocatalytic properties of the device.

3. *“Multiscale Charge Transport in van der Waals Thin Films: Reduced Graphene Oxide as a Case Study”*; A. Kovtun, A. Candini, A. Vianelli, A. Boschi, S. dell’Elce, M. Gobbi, K. H. Kim, S. Lara-Avila, P. Samorì, M. Affronte, A. Liscio, V. Palermo; *ACS Nano* **15**, 2, 2654 (2021), www.doi.org/10.1021/acsnano.0c07771

I performed minor electrical characterisation of the final devices. I also discussed and commented the results of the analysis.

Oral Contributions

1. Title presentation: *“Benchmarking of Graphene-based materials: new standards for industry”* (15 min)

Conference: "Graphene Week 2019"

From 23 to 27 September 2019, at Marina Congress Centre, Helsinki (Finland).

2. Title presentation: *“Low temperature resistivity behaviour in GRM films: role of the vertical stacking order”* (15 min)

Conference: "FisMat 2019"

From 1 to 4 October 2019, at Università di Catania, Catania (Italy).

Poster Contributions

Title poster: *“Preparation of graphene-based films with tuned structural and electrical properties”*

Conference: "Materials.it 2018"

From 22 to 26 October 2018, at CNR, Bologna (Italy).

Schools

1. Name: *"Graphene Study Winter 2018"*

From 5 to 10 February 2018, at Innsbruck Univ. Centre, Obergurgl (Austria).

Topics: Structural characterisation of graphene-based materials.

30h of seminars

2. Name: *"NANO-BIS"*

From 18 to 22 June 2018, at Università di Bologna, Bologna (Italy)

Topics: Physical growth and deposition of nano-objects; review of nanoscale characterization techniques; basics of nano-structures modelling and presentation of common applications.

22h of seminars

3. Name: *"Aldo Armigliato SEM School in Material Science"*

From 9 to 13 November 2020, on-line*

Topics: Scanning Electron Microscopy

13h of theoretical lectures + 9h of practical sessions

Acknowledgments

I would prefer making my acknowledgments in Italian. I deeply apologize to who will not be able to read them, as well as to who will find them too informal.

Il mio primo ringraziamento va alle nostre dolci e verdeggianti colline: ci sono sempre state quanto ho avuto bisogno di libertà “riprendere fiato”. E misuro le parole se scrivo che senza di loro non sarei vivo.

Ringrazio Bologna. Io, figlio minore di questa dinamica, stupida, colorata città, ho perso il conto quante notti mi ha accolto e protetto tra i suoi portici.

Ringrazio il vino, che se non esistesse sarei sicuramente una persona migliore ma più vuota. Ringrazio la musica, quella di 40 anni fa e quella troppo attuale, che mi ha fatto diventare un cuoco migliore, o almeno ha contribuito a diminuire i volti disgustati davanti alle mie pietanze.

Ringrazio i miei genitori, Franca ed Ermes, che mi hanno sostenuto, sempre ed incondizionatamente, anche quando il nostro sguardo ammirava orizzonti differenti.

Ringrazio mio fratello, Manuel, che se continuerà ad essere testardo un decimo di quanto lo sono io, avrà sempre il vento alle spalle e poche preoccupazioni.

Ringrazio mia nonna, Silvana, per guardarmi sempre con profondo orgoglio e stima, nonostante io spesso l'abbia trascurata.

Ringrazio il mio gruppo a ISOF e ringrazio Enzo, che ne è stato faro anche dalla lontana Svezia. Ringrazio Andrea L., per avermi dato la possibilità d'intraprendere questo percorso ed avermi riempito di ideuzze la mente. I suoi aneddoti sono stati spesso un motivo per rallegrarsi. Ringrazio Alessandro K., per i tanti insegnamenti e per le molte parole d'incoraggiamento. Ringrazio Derek, per la sua compostezza e per avermi guidato nei grovigli della lingua britannica. E poi ringrazio Vanesa, Maria, Emanuele, Andrea C., Alessandra e Jeff.

E ringrazio gli altri miei “pari” dentro queste mura bianche con finestre gialle, i quali hanno saputo essere compagni prima che semplici colleghi. Marco, dalla parola pronta, ma non sempre al posto giusto. Claudio, da modenese, per la sua sopportazione dei piccoli

scherni quotidiani. Filippo, per il suo frullato di serietà e simpatia. Cecilia, per la sua ospitalità e per le sue risate. Giada, per la sua gentilezza e per le mille rocambolesche storie di cui è stata protagonista. Sara K., per aver mostrato qualche volta il suo cuore con ripieno morbido. Vitaliy, per la sua eleganza lusitana nei modi. “Il Porci” per la sua schiettezza e per le “baffe” (che non son più nella mia dieta). Vasia, per la sua capacità di trovare sempre un sorriso o, all'occorrenza, un dolcetto. Li ringrazio per tutte le serate passate e per tutte quelle che sono ancora lì ad aspettarci.

Ringrazio i chimici “modenesi”, Chiara, Fabrizio e Fabio (berrò una birra in tuo onore di tanto in tanto, si sa, la vita è così...).

Ringrazio i fisici “modenesi”: il prof. Affronte, Alberto, Claudio e Samuele, che mi hanno accolto permettendomi di utilizzare la loro strumentazione senza troppa diffidenza. Una menzione speciale è poi per Rita T., senza il suo forno, questa tesi non esisterebbe.

Ringrazio Luca e Paolo, fisici marchigiani, con cui ho condiviso tanti discorsi e di cui sto solo anticipando gioie e sofferenze.

Ringrazio tutti quei miei amici che guardando questo mio percorso “da lontano” non mi hanno mai abbandonato. Con loro ho vissuto momenti ed emozioni intense durante questi ultimi anni. Ringrazio Stanza, Giulio, Leo Sacc, Monta, Ale C., Barbara, Manfe, Miglio, Borto, Friso e Iaia, Mino e Giulia, Rinno e Chiara, Matte Bozzoli e Margherita, Frenci, Checco ed Eva, Martina e Paolo, Manu Rucci, Filippo Boia, Ale B. ed Ivan.

E a chi ho dimenticato di ringraziare offrirò sicuramente una bottiglia di vino.

Ringrazio Milena e Massimo per avermi voluto bene come un figlio. Il tempo mi permette di ringraziare anche Sara. Ora lei è nel cuore dell'Europa ad inseguire nuove primavere ed io le auguro di raggiungerle.

Ringrazio Moni, che è stata al mio fianco nelle ultime settimane di questo lavoro, ma è scappata subito dopo aver “organizzato la festa”. A lei auguro di “sognare forte, sognare sempre”, nonostante le ferite fresche che ancora provo.

Per finire, ringrazio chi si è arrabbiato con me quando ho commesso un errore, o quando semplicemente avevo sbagliato strada. Ringrazio chi ha aperto le braccia per abbracciarmi (anche virtualmente, in tempi pandemici) nonostante conoscesse i miei mille difetti. Ringrazio tutti quelli che mi han strappato un sorriso le volte che piangevo dentro. E ringrazio quelli che me ne han strappati due quando le lacrime erano vere.